Imperial College London
Department of Mechanical Engineering

Attenuation of the unsteady loading on a high-rise building using active control

Xiao Hu

Submitted in part fulfilment of the requirements for the degree of
Doctor of Philosophy in Mechanical Engineering of the Imperial College London
January 2023

Declaration

I hereby declare that the work presented in this thesis is the result of my original research, except where acknowledged in the text. The findings reported throughout this thesis have been presented at several conferences and published or submitted for publication in scientific journals.

Abstract

The present work numerically investigates the 3D flow structures around a canonical high-rise building immersed in an atmospheric boundary layer at different oncoming wind angles, using wall-resolved large eddy simulations. The switching between two vortex shedding modes is explored, and the influence of the atmospheric boundary layer on suppressing symmetric vortex shedding is identified. It is shown that the antisymmetric vortex shedding mode is prevalent in the near wake behind the building, with strong coherence between the periodic fluctuations of the building side force and the antisymmetric vortex shedding mode demonstrated. Exploiting this idea, active flow control strategies are designed to alleviate the aerodynamic side-force fluctuations.

Two feedback control strategies are then developed to attenuate the building's unsteady loading when the oncoming flow is normal to the wider side of the building, using pressure sensing on just a single building wall. The sensor response to synthetic jet actuation along the two 'leading edges' of the building is characterised using system identification. Both the designed linear controller and the least mean square adaptive controller attenuate successfully the side-force fluctuations when implemented in simulations. The linear controller exhibits better performance, and its effect on the flow field is to delay the formation of dominant vortices and increase the extent of the recirculation region.

Motivated by the effect of the downwash flow on the near wake of the building, an open-loop active control in the form of a synthetic jet located on the top surface is then considered. The aim is again to suppress side force fluctuations, this time exploring whether the simpler control setup can be effective across a wide range of oncoming wind angles. The behaviour of the synthetic jet and its effect on the building's unsteady side force, time-averaged flow fields and unsteady flow structures are investigated numerically. The synthetic jet actuation is found to reduce the side-force fluctuation of the building, enhance the downwash flow and successfully attenuate the antisymmetric vortex shedding.

Finally, the possibility of using a robust feedback control strategy mitigating the unsteady loading of a high-rise building exposed to differing oncoming wind directions is explored. A reference linear open-loop transfer function is identified, and the differences between the reference open-loop system and open-loop transfer functions for different oncoming wind angles are assessed by ν-gap. An H_∞ loop-shaping feedback controller is then designed and achieves the attenuation of the building's side-force fluctuations for differing oncoming wind angles.

This work can provide a theoretical basis for the practical application of novel active control approaches to attenuating the side-force fluctuation of the high-rise building exposed to differing oncoming wind directions.

Acknowledgements

First and foremost, I would like to express my sincere gratitude to my supervisor Professor Aimee Morgans, for her academic support and great instructions before and during my time at Imperial College London. She is always kind, humble and empathetic towards young researchers. Many thanks first for helping me obtain a scholarship for this project and for organising this fantastic research project in link with my interests.

This PhD would not be possible without the support of the Imperial College President's PhD Scholarship committee, who provided financial assistance throughout my doctoral study. I have been blessed with a perfect group of fellow researchers, and I sincerely thank them for their help. I would like to thank my colleagues and dear friends, Dr. Jialin Su, Dr. Juan-Guzman Inigo and Ms. Dania Ahmed, for their timely discussions and generous help. They were always available to discuss my questions and helped me find the solutions. I also thank all my colleagues who were so kind, friendly and humble. Particularly the days I spent with Dr. Dong Yang, Dr. Saikumar Reddy Yeddula, Dr. Yazhou Shen and Dr. Lionel Hirschberg will remain memorable.

Many thanks to my friends Yuxin Hao, Qiang Xu, Bowen Zhan and Haoyu Zuo - we began our PhD programs together and you were just like my families during the past several wonderful years.

I am grateful to my Master's Supervisor, Professor Shuxing Yang, who has a continuous impact on my academic work. He encouraged me to study abroad and be a part of Imperial College London.

Last but not the least, I would like to acknowledge all the unconditional spiritual supports, concerns and encouragement I always had from my parents and Xin Yang. My cute Bengal cat also deserves my wholehearted thanks as well. To them, I sincerely dedicate this thesis.

Contents

List of Tables

List of Figures

Chapter 1

Introduction

1.1 Background

With the increasing scarcity of urban land resources and the rapid expansion of the population, the number of high-rise buildings has experienced astronomical growth in recent years. As shown in figure 1.1, by the end of 2020, there were 1733 high-rise buildings worldwide with heights in excess of 200 m, marking a significant 600% increase from 262 in 2000. Similarly, the total number of super high-rise buildings (higher than 300 m) in the world is at present 191, and this number is expected to further increase to 300 in the next 5 years (Skyscrapercenter, 2021).

The vertical expansion of cities is also driven by both rapid development in materials and construction techniques. New-generation high-rise buildings are typically slender and lightweight structures that protrude significantly into the turbulent atmospheric boundary layer. It is critical to assess the dynamic response of such structures to external environmental loads. In particular, unsteady wind loading generated by aerodynamic features like vortex-shedding has the potential to strongly deteriorate the structural

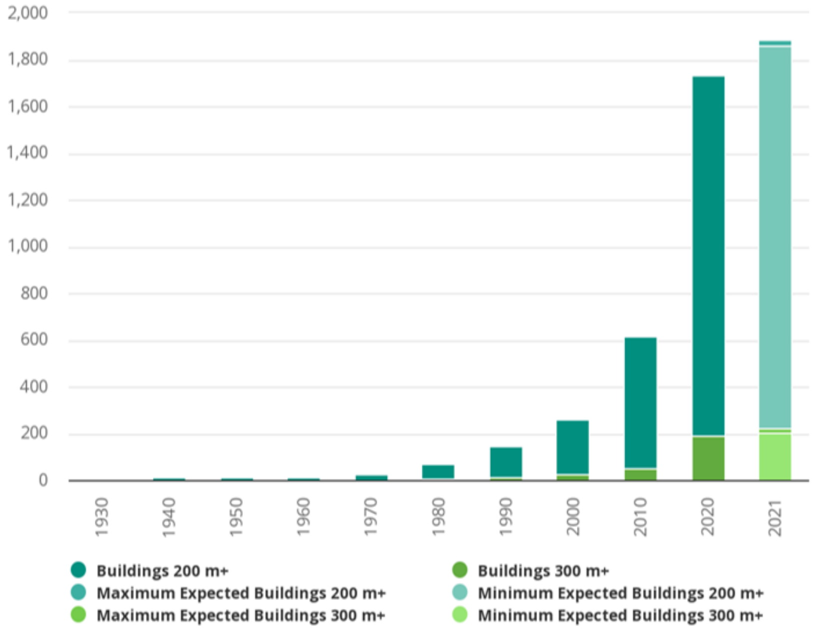

Figure 1.1: Number of buildings with heights in excess of 200m in the world at the end of each decade (Skyscrapercenter, 2021).

stability and occupant comfort of high-rise buildings (Irwin, 2009). Moreover, the exposure of these buildings to extreme weather events is a considerable and increasing risk (Pörtner *et al.*, 2022). With the severity and frequency of extreme weather events increasing, methods for mitigating unsteady wind loading for high-rise buildings could become an important technology.

The unsteadiness in the wake flow behind a high-rise building is the primary source of its unsteady wind loading. Therefore, a reduction of the building's unsteady wind loading can be achieved by controlling the flow field around it. Flow control techniques for reducing the wind loading of high-rise buildings can be decomposed into two categories: passive and active (Gad-el Hak, 2000). Passive control techniques are most often implemented using geometrical modifications and do not need any energy input. Active control uses powered actuation to manipulate the unforced flow towards a desired outcome.

Passive techniques focusing on local modifications in the building shape, such as corner rounding and chamfering (Tse *et al.*, 2009; Elshaer *et al.*, 2016), have been extensively studied in an attempt to mitigate the unsteady wind loading over the past decades. However, these strategies always come with a loss of usable floor area and an increase in construction cost, and they cannot adaptively respond to the differing oncoming wind flow. In this work, we investigate numerically the active flow control techniques aiming to attenuate the unsteady wind loading of a canonical high-rise building immersed in the atmospheric boundary layer. Synthetic jets, also named zero-net-mass-flux (ZNMF) jets, are employed as the actuation. The synthetic-jet technique is promising, because not only it does not require the modification of the building shape, but it would also be activated only a few times a year when the building is experiencing extreme weather conditions. This work is a concept study which can provide a theoretical basis for the practical application of active control approaches to high-rise buildings.

1.2 High-rise building flow

An in-depth understanding of the flow structures around high-rise buildings is of fundamental importance to identify the sources of unsteady loading and inform mitigation strategies. High-rise buildings have similar bluff-body geometries to finite-length wall-mounted square cylinders (FWMCs) with high aspect ratios, whose three-dimensional (3D) flow structures have been studied extensively in recent years. In this section, we summarize the present knowledge on the wake structures around a square FWMC first and then proceed to review investigations on high-rise buildings immersed in the atmospheric boundary layer.

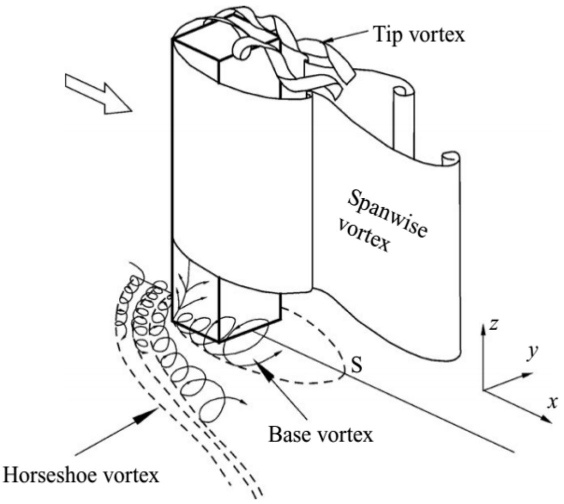

Figure 1.2: Wake vortex around the finite-length square cylinder (Wang *et al.*, 2006).

1.2.1 Flow around a square FWMC

The flow structures around a square FWMC are distinct from those of an infinite-length square cylinder. The free end and wall-cylinder junction introduce additional flow complexity to the wake. The free-end downwash flow and the upwash flow from the cylinder base interact strongly with the spanwise von Kármán vortex structures, forming a highly three-dimensional near wake around the cylinder (Sumner *et al.*, 2004; Wang & Zhou, 2009; Sumner, 2013).

The time-averaged wake structures behind the cylinder generally include dipole and quadrupole types characterized by one and two pairs of counter-rotating streamwise vortices respectively (Yauwenas *et al.*, 2019). The quadrupole wake structure behind a square FWMC is shown in the schematic in figure 1.2. The vortex pair occurring near the free end of the square FWMC, referred to as tip vortices, is ascribed to the free-end downwash flow (Kawamura *et al.*, 1984; Park & Lee, 2000). The base vortices close to the wall (floor) junction shown in figure 1.2 are associated with the upwash flow from the ground surface and are enhanced as the relative thickness of the boundary

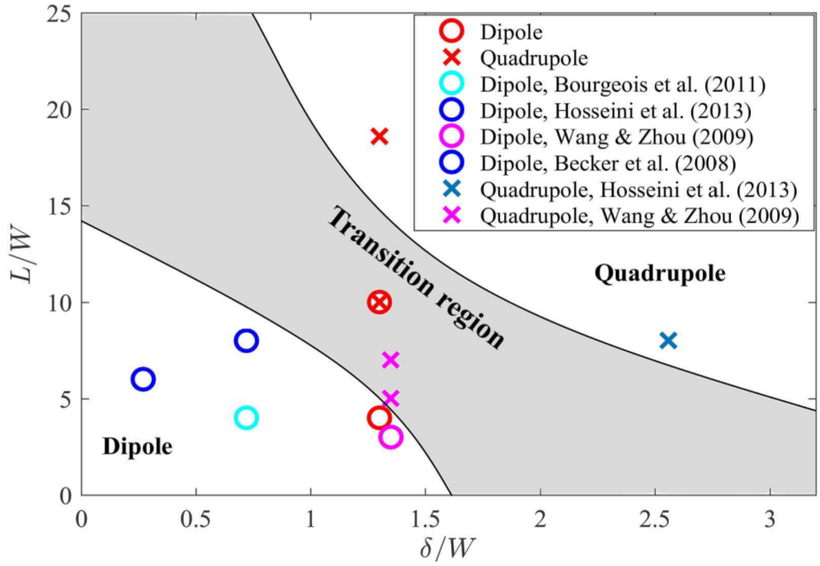

Figure 1.3: A parametric diagram of the time-averaged wake structure (Yauwenas *et al.*, 2019).

layer increases (Wang *et al.*, 2006). A thick boundary layer relative to the cylinder height allows the formation of base vortices and results in a quadrupole structure, while only tip vortices (the dipole structure) can be observed with a thinner one (Hosseini *et al.*, 2013). Moreover, Yauwenas *et al.* (2019) experimentally investigated how the aspect ratio (height L to width W) of the FWMC affects the time-averaged wake and summarized a parametric diagram to predict the mean wake structure based on the aspect ratio and the boundary-layer thickness (figure 1.3).

In terms of the instantaneous wake structures, Wang & Zhou (2009) observed that two spanwise vortex shedding modes, comprising antisymmetric and symmetric vortex shedding, occur intermittently in the near wake of a square FWMC. This intermittent vortex shedding was confirmed by Bourgeois *et al.* (2013), Yauwenas *et al.* (2019) and Behera & Saha (2019) using measurement of the pressure fluctuation on the side faces. Several experimental studies were conducted to understand this intermittent nature of vortex shedding in the FWMC wake. Wang & Zhou (2009) and Wang *et al.* (2017) observed the symmetric vortex shedding mode is more prevalent near the free end, and they suggested that free-end downwash flow tends to convert the spanwise vortex shedding from antisymmetric to symmetric. A numerical study performed by Behera & Saha (2019) also reported the impact of the downwash flow on suppressing antisymmetric spanwise vortex shedding.

1.2.2 Wind loading of a high-rise building

These investigations on finite-length square cylinders were conducted mostly with the cylinders exposed to a freestream inflow. High-rise buildings, rather than being in a freestream flow, typically penetrate substantially into an atmospheric boundary layer. Furthermore, the cross-sectional geometry of high-rise buildings is not perfectly square. These differences increase the complexity of the flow features.

Studies on the wind loading of high-rise buildings extensively use rigid building models in preference to high-expense aeroelastic ones. Conventional approaches to investigating unsteady wind around buildings mainly focus on wind tunnel testing. The Commonwealth Advisory Aeronautical Council (CAARC) standard tall building model (with dimensions 30m×45m×180m), has been adopted as a benchmark test case in the high-rise building aerodynamics modelling since its inception by Melbourne (1980). Obasaju (1992) simulated the atmospheric boundary layer over terrain with a certain roughness length and investigated the flow past a reduced-scale CAARC building model in this simulated boundary layer by experiments. He found that the simulated turbulent inflow results in a contraction of the near wake recirculating flow region and larger fluctuations in the aerodynamic forces.

Given the drastic enhancement of available computing power during the last decade, the technique of Computational Fluid Dynamics (CFD) has increasingly been used as an alternative approach to investigating the flow around a high-rise building. Numerical studies using Reynolds-averaged Navier-Stokes (RANS) turbulence models have been extensively conducted to obtain the steady pressure coefficient and time-average flow of high-rise buildings in the past (Tominaga *et al.*, 2008; Tominaga, 2015; Hertwig *et al.*, 2012). However, these RANS models are always challenged by the flow unsteadiness that is particularly relevant in detached regions of the flow such as the building wake. Large Eddy Simulation (LES), a scale-resolved turbulence modelling method that fully resolves instantaneous large flow structures, is gaining interest in terms of simulating the unsteady loading on high-rise buildings with better accuracy. Thordal *et al.* (2019) reviewed various turbulence models used in numerical studies for wind effects on high-rise buildings and advised LES as the optimal approach due to its lower computational requirement than Direct Numerical Simulation (DNS) and higher accuracy than RANS. Several numerical studies using LES have also been performed, demonstrating that LES generally achieves satisfactory agreement with experimental results, especially in terms of pressure fluctuations, and reveals more detailed flow features (Huang *et al.*, 2010; Yan & Li, 2015; Ricci *et al.*, 2018; Zhang & Habashi, 2015).

Both the above experimental and numerical investigations into the flow around high-rise buildings have so far focused predominantly on aerodynamic forces. However, at the start of this PhD research, to our knowledge, no existing studies clearly elucidate the wake structures around a high-rise building immersed in an atmospheric boundary layer.

1.3 Flow control

Flow control techniques for bluff bodies have received considerable research effort aiming to satisfy many engineering requirements (Choi *et al.*, 2008; Brunton & Noack, 2015), such as lowering drag for road vehicles, reducing vibration of submarine pipelines, and

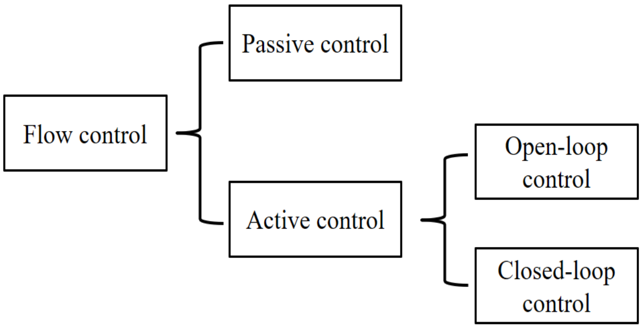

Figure 1.4: Flow control techniques classification.

in this project, attenuating the unsteady loading of high-rise buildings. To effectively review the research on flow control for high-rise buildings, a classification for control strategies is given (figure 1.4). Depending on whether the energy input is required, flow control techniques for high-rise buildings can be decomposed into two categories: passive and active (Gad-el Hak, 2000).

1.3.1 Passive control

Passive control techniques for bluff bodies are often implemented through shape modifications or aerodynamic element installation. They are usually designed to delay flow separation or to modify the wake flow structures. In terms of high-rise buildings, passive control methods always directly act on the spanwise vortex shedding to attenuate the unsteady loading (Kareem *et al.*, 1999).

High-rise buildings typically have a rectangular cross-section characterized with local sharp corners. Several previous studies considered methods that modify the shape of the corners to optimize the aerodynamic performance of high-rise buildings (figure 1.5). For instance, Tse *et al.* (2009) performed experiments to investigate the influence of chamfered and recessed corners on a high-rise building's aerodynamic responses and re-

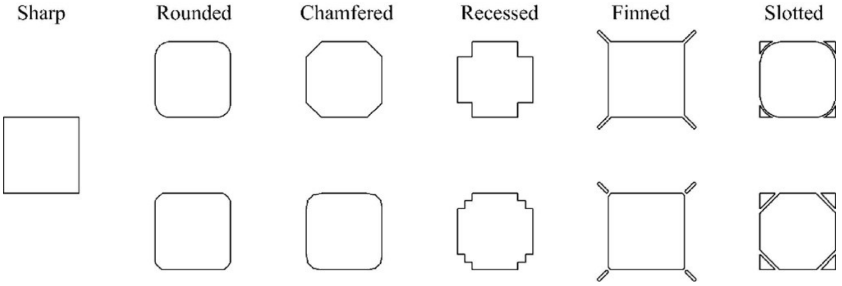

Figure 1.5: Common examples of tall building corner modification (Elshaer *et al.*, 2017).

ported the effectiveness of both chamfered and recessed corners in reducing along-wind and crosswind responses. Wind tunnel tests conducted by Kawai (1998) and Carassale *et al.* (2014) found that rounded corners promote the reattachment of the flow on the lateral faces and suppress wind-induced loading. Elshaer *et al.* (2017) coupled 2D numerical simulations and an artificial neural network to develop a building corner aerodynamic optimization procedure to reduce the wind loading and then verified the optimal shapes using a high-fidelity 3D LES.

Another solution to reduce the wind loading of a high-rise building is varying cross-section shapes along the height through tapering, twisting or the addition of openings. Variations of sectional shape with height could affect the overall vortex structure behind a high-rise building, further improving its aerodynamic performance (Tamura *et al.*, 2010). Kim & Kanda (2010) experimentally investigated the effect of tapering on the wind loading of a high-rise building. They found that tapering disturbs the uniform spanwise vortex shedding through all heights, and the vortices are shed irregularly and incoherently, which causes the reduction of the fluctuating side force. Elshaer *et al.* (2016) employed twisting to achieve varying shapes along the height, and they found the optimal twisting angle which can obtain the lowest along-wind moment coefficient and RMS values of the cross-wind moment coefficient.

High-rise buildings share a similar geometry to finite-length wall-mounted square cylinders with a high aspect ratio. A different passive drag reduction method for a square FWMC is to add physical extensions. Ogunremi & Sumner (2015) investigated the flow around a square FWMC with a splitter plate experimentally and reported that the splitter plate disrupts the interactions of the shear layers originating from the side faces and further weakens the spanwise vortex shedding. Wang *et al.* (2022) successfully utilized a flexible plate clamped at the free-end leading edge to strengthen the downwash flow and further modulate the aerodynamic forces on a square FWMC.

1.3.2 Active control

Compared to passive control approaches, active control techniques require an additional energy input for operation. There are various types of actuators used in active flow control, and common active control actuators include moving surfaces, plasma actuators and fluidic devices such as synthetic jets (Cattafesta III & Sheplak, 2011). Active control techniques usually do not require geometrical modifications of the building, which avoids an increase in construction costs due to the complex structural and architectural design. Moreover, they would be activated only a few times a year when the building is experiencing extreme weather conditions. Depending on whether input commands are associated with sensor signals, active control techniques can be further classified into open-loop and closed-loop types (figure 1.4).

Open-loop control techniques have been applied in the flow past a high-rise building to achieve unsteady loading reduction. Menicovich *et al.* (2014) experimentally employed active open-loop control in a form of several steady jets near the spanwise leading edges of the building to mitigate the mean and dynamic aerodynamic forces. Zheng & Zhang (2012) numerically investigated the effect of steady suction near the spanwise leading edge of the side faces on the aerodynamic performance of a simplified high-rise building model and reported that the steady suction can effectively suppress the spanwise flow separations. Moreover, motivated by the effect of the downwash flow on the near wake behind the FWMC (Wang & Zhou, 2009; Behera & Saha, 2019; da Silva *et al.*, 2020), active open-loop control methods with actuation located at the free end have also been investigated. Wang *et al.* (2018) experimentally studied the effect of steady slot suction near the free-end leading edge of a square FWMC on its aerodynamic forces. Investigations into active control strategies for suppressing the aerodynamic forces of high-rise buildings have so far focused predominantly on the case with the oncoming wind normal to the wider side. To our knowledge, no existing studies investigate the application of a single open-loop controller for the attenuation of the building's unsteady loading across differing oncoming wind angles.

In contrast to open-loop control, active feedback control generates its actuation signals based on the measurement of sensor signals (figure 1.6). This offers the potential for higher actuation efficiency and can also provide enhanced robustness to uncertainty and disturbances, and the possibility of optimizing the choice of controller signal (Choi *et al.*, 2008; Brunton & Noack, 2015). While studies on feedback control applied to high-rise buildings are limited, feedback control has been applied successfully to bluff-body flows in other contexts. We therefore cover a broader range of bluff bodies in the present review.

Feedback control techniques can be divided into two main categories based on the choice of the control strategy. The first control strategy is to use model-independent controllers. These controllers always adopt gradient methods to seek the maximum or minimum of some aerodynamic parameters like drag without any underpinning dynamic model, making it desirable for highly complex flows. For instance, Henning & King (2005) used an extremum-seeking controller experimentally to reduce the drag of a D-body in a turbulent flow and found that the controller synchronized vortex shedding, resulting in a

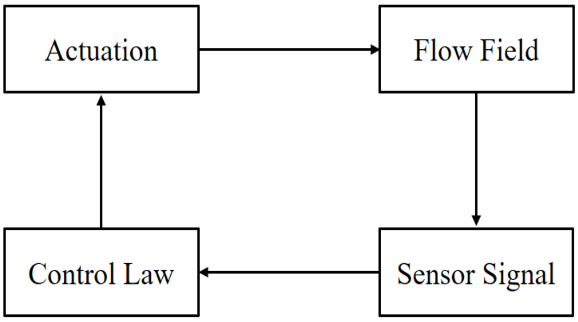

Figure 1.6: Schematic of closed-loop control system.

base pressure increase. Pastoor *et al.* (2008) designed slope-seeking feedback control strategies for the same bluff body, achieving a 15 % drag reduction. A physics-based opposition control strategy that combines closed-loop gradient feedback with an open-loop periodic forcing was explored by Li *et al.* (2016) to symmetrise the bimodal dynamics of a turbulent wake behind the Ahmed body, also achieving a slight base pressure recovery.

Another approach is to use model-based controllers requiring a mathematical model of the flow system. The employed models can be obtained by white-box, grey-box or black-box modelling approaches (Brunton & Noack, 2015). These approaches can capture different levels of flow physics. High-dimensional white-box models always established based on the linearization of the Navier-Stokes equations have been used in active feedback control for some low-Reynolds number flows such as cavity flows (Rowley *et al.*, 2006) Moreover, reduced-order models resolving most of the relevant flow features in a lower dimensional state are also applied in the design of feedback controllers. These models can be obtained through various approaches such as Proper Orthogonal Decomposition (POD) or dynamic mode decomposition (DMD). For example, Weller *et al.* (2009) employed a reduced-order model obtained through POD analysis of the laminar flow around a square cylinder to design a feedback controller. The designed controller was then implemented in numerical simulations and the result showed it can yield a long-term reduction in drag.

In terms of black-box models, they are state-space models or transfer functions identified from the input–output response of the flow system to the actuation. With the advantage of rapid identification and easy implementation, black-box models have been extensively applied in feedback control for bluff body flows. Stalnov *et al.* (2011) designed experimentally a phase-locked loop with fluidic actuators for the D-shaped cylinder flow, reducing the wake unsteadiness significantly. Flinois & Morgans (2016)) designed feedback controllers for the flow past a D-body based on a linear state-space model obtained through Eigensystem Realization Algorithm (ERA). Another approach for system identification is to perform the open-loop forcing with various frequencies and obtain a transfer function based on the frequency response. Dahan *et al.* (2012), Dalla Longa *et al.* (2017) and Evstafyeva *et al.* (2017) developed sensitivity-based feedback controllers based on this approach for a range of two- and three-dimensional bluff bodies via numerical simulations, achieving a reduction in base pressure force unsteadiness and aerodynamic drag. This thesis also uses this approach for system identification and more details about this method are described in Chapter 3. At present, we believe that there is no existing literature that investigates the application of feedback control for the attenuation of unsteady loading on a high-rise building immersed in an atmospheric boundary layer.

1.4 Conclusions and thesis plan

This chapter focuses on introducing the main challenges and previous studies that are relevant to the work presented in this thesis. Gaining an in-depth understanding of the flow around high-rise buildings and exploring the active flow control strategies for it are of interest to academic and industrial communities. This project aims to numerically investigate the flow structures around a canonical high-rise building immersed in an atmospheric boundary layer, and then to develop active control strategies to alleviate the building's unsteady wind loading. The feedback control strategies used in this thesis mimic the controller that has been applied successfully in other bluff-body flows (Evstafyeva *et al.*, 2017; Dalla Longa *et al.*, 2017; Flinois & Morgans, 2016; Dahan *et al.*, 2012), while the open-loop ones are motivated by the effect of the downwash flow on the near wake. The structure of this thesis is presented as follows.

Chapter 2 introduces the numerical method used to simulate the flow around a high-rise building immersed in the atmospheric boundary layer as well as modal decomposition tools for the flow field analysis.

Chapter 3 provides insights into the 3D flow structures around a high-rise building when the oncoming wind is normal to the wider side. Feedback control strategies are then designed to alleviate the unsteady loading.

Chapter 4 presents the use of an open-loop active control strategy employing a synthetic jet on the top surface to mitigate the aerodynamic side-force fluctuations of a high-rise building across differing oncoming wind angles.

Chapter 5 presents the design of an H_∞ loop-shaping feedback controller which aims to attenuate the unsteady loading of a high-rise building exposed to differing oncoming wind directions.

1.5 Related publications

1. Journal publications during the course of the work:

    (a) Hu, X. & Morgans, A. S. 2022 Attenuation of the unsteady loading on a high-rise building using feedback control. *Journal of Fluid Mechanics.* 944, A10.

   (b) Hu, X. & Morgans, A. S. 2022 Attenuation of the unsteady loading on a high-rise building using top-surface open-loop control. *Journal of Fluid Mechanics.* (Second Revision).

2. The work was presented during the following conferences and events:
   (a) 14th European Fluid Mechanics Conference, Athens, Greece, 2022.
   (b) 73th American Physical Society's Annual Meeting of the Division of Fluid Dynamics, Virtual, USA, 2020.
   (c) 74th American Physical Society's Annual Meeting of the Division of Fluid Dynamics, Phoenix, USA, 2021.
   (d) 75th American Physical Society's Annual Meeting of the Division of Fluid Dynamics, Indiana, USA, 2022.
   (e) UK Fluids Conference. Southampton, UK, 2021.

Chapter 2

Research Methodology

In this chapter, the numerical method used to model the flow around a high-rise building is introduced, and details on the flow solver are also described. This is followed by a brief overview of two modal decomposition tools which are used to gain further insight into the flow dynamics in this work: proper orthogonal decomposition (POD) and spectral proper orthogonal decomposition (SPOD).

2.1 Numerical Method

With the increase in computing capacity, the technique of Computational Fluid Dynamics (CFD) has increasingly been used to investigate the aerodynamic performance of a high-rise building (Tominaga *et al.*, 2008; Tominaga, 2015; Ricci *et al.*, 2018; Yan & Li, 2015; Huang *et al.*, 2010; Giangaspero *et al.*, 2022). Compared to wind tunnel experiments, CFD techniques are capable of capturing more abundant information on flow features which might be difficult to measure in wind tunnel studies, and their ability to test various geometries without building several physical models reduces the design cost.

Extensive numerical studies in wind engineering use Reynolds-averaged Navier-Stokes (RANS) equations (Tominaga *et al.*, 2008; Tominaga, 2015; Hertwig *et al.*, 2012). This approach splits the flow variables into a mean and a fluctuating component. The time-averaged flow is then resolved while the effect of turbulent fluctuations on the mean flow, i.e. Reynolds stresses, is captured using a turbulence model. Although RANS turbulence modelling, as a computationally economical method, can be tuned to obtain a good prediction of mean flow properties, it is always challenged by the unsteadiness in the bluff body flows such as massive flow separation and recirculation (Blocken, 2014; Thordal *et al.*, 2019).

Another approach, Direct Numerical Simulation (DNS), can resolve all turbulent fluctuations down to the Kolmogorov length scale. This approach solves the Navier-Stokes equations directly without any turbulence model and has the highest accuracy. However, the expensive computational cost makes it impossible for industrial applications with a relatively high Reynolds number.

Large Eddy Simulation (LES), the turbulence modelling approach used in this project, models small-scale turbulence with a length scale smaller than the filter size using a sub-grid scale model while directly resolving the large-scale turbulence. The filter size is intrinsically dependent on the computational grid. By modelling small-scale turbulence, LES significantly reduces the computation cost in comparison to DNS. Moreover, insight into instantaneous flow behaviour is important for studying the unsteady wind loading of a high-rise building, and LES allows access to instantaneous flow structures and captures more accurate turbulent fluctuations than RANS. These attributes make LES a desirable choice for numerical studies on the flow around a building (Ricci *et al.*, 2018; Thordal *et al.*, 2019; Krajnović, 2009), and the details of the LES solver used are described below.

2.1.1 Large Eddy Simulations

All simulations in this project are conducted on an open-source CFD software OpenFOAM that is written in C++ and uses the finite volume method to solve the fluid dynamic problems. The PimpleFOAM solver, a transient solver for incompressible turbulent flow that uses the pressure implicit with splitting operators PISO – SIMPLE algorithm for evaluating the pressure fields, is employed to calculate the flow around a high-rise building. It has been successfully used to compute bluff body flows, such as the flow around an Ahmed body (Hesse & Morgans, 2021), a road vehicle (Hesse & Morgans, 2023) and an axisymmetric bluff body (Zhu & Morrison, 2021).

The computational domain is decomposed into small control volumes based on the unstructured meshes generated by Star-CCM+, and the governing equations are applied over each control volume. The governing equations for the flow around a building are described by the incompressible Navier-Stokes equations based on the conservation of mass and momentum, which are written using tensor notation as follows (Wilcox, 1998):

$$\frac{\partial u_i}{\partial x_i} = 0 \tag{2.1}$$

$$\frac{\partial u_i}{\partial t} + \frac{\partial u_i u_j}{\partial x_j} = -\frac{1}{\rho}\frac{\partial p}{\partial x_i} + \nu \frac{\partial}{\partial x_j}\left(\frac{\partial u_i}{\partial x_j}\right) \tag{2.2}$$

where u_i is the component of the velocity in the i^{th} spatial direction, ρ is the density of the fluid, p is the pressure and ν is the kinematic viscosity. Through spatial and temporal discretization, the above partial differential equations can be converted into a linear algebraic equation system which can be solved to obtain the transported quantities for the control volume. In this project, following the suggestion given by Ferziger *et al.* (2002), the second-order central difference scheme is chosen to discretize the convective and diffusion terms due to its low dissipation, while the Crank–Nicolson scheme is used to discretize the temporal derivatives.

Large Eddy Simulation (LES) is used as the turbulence model for all simulations in this project. The idea of this turbulence model is resolving large-scale structures and modelling the smaller ones by a subgrid-scale (SGS) model. A filtering process is required to obtain small-scale vortices which need to be modelled by SGS models. Based on the filtering process, the flow function can be written as

$$\Phi(x,t) = \bar{\Phi}(x,t) + \Phi'(x,t) \tag{2.3}$$

where $\bar{\Phi}$ represents the large-scale part which will be resolved, and Φ' stands for the filtered small scale modelled by the SGS model. The resolved term is determined by the spatial filtering operator and can be obtained as follows

$$\bar{\Phi}(\mathrm{x},t) = \int_{-\infty}^{+\infty} \Phi(\mathrm{r},t) G(\mathrm{x}-\mathrm{r},t) d\mathrm{r} \tag{2.4}$$

where $G(x)$ is the filtering function. Filtering functions for LES have been extensively reported in the existing literature, and a typical filtering function used in the finite volume method is the box filter:

$$G\left(x\right) = \begin{cases} \frac{1}{\Delta} & |x| \leq \frac{\Delta}{2} \\ 0 & |x| > \frac{\Delta}{2} \end{cases} \tag{2.5}$$

with Δ being the filtering width, also the magnitude of the grid size. If the filtering width tends to be infinitely small, the simulated results obtained from LES will become comparable to DNS which resolves all the turbulence length scales. Applying filtering operations to the unsteady incompressible Navier-Stokes equations, the filtered continuity and momentum equations are obtained as

$$\frac{\partial \bar{u}_i}{\partial x_i} = 0 \tag{2.6}$$

$$\frac{\partial \bar{u}_i}{\partial t} + \frac{\partial \bar{u}_i \bar{u}_j}{\partial x_j} = -\frac{1}{\rho}\frac{\partial \bar{p}}{\partial x_i} + \nu \frac{\partial}{\partial x_j}(\frac{\partial \bar{u}_i}{\partial x_j}) - \frac{\partial \tau_{ij}}{\partial x_j} \tag{2.7}$$

where variables with an overbar stand for the filtered flow variables which will be resolved. τ_{ij} is the subgrid-scale stress, and the last tensor term in the momentum equation, which is generated after the spatial filtering operations, can be regarded as a divergence of τ_{ij}.

The subgrid-scale stress is given by the SGS model for the closure of the filtered equation. Here the Wall-Adapted Local Eddy-viscosity (WALE) model, an eddy viscosity model developed by Nicoud & Ducros (1999), is employed. This model represents the effects of unresolved turbulent structures that account for the energy dissipation in the flow. The traceless part of τ_{ij} can be expressed as

$$\tau_{ij} = \frac{1}{3}\delta_{ij}\tau_{kk} - 2\upsilon_T \overline{S_{ij}} \tag{2.8}$$

where δ_{ij} is the Kronecker symbol, υ_T is the eddy viscosity, and $\overline{S_{ij}} = \frac{1}{2}\left(\frac{\partial \overline{u_i}}{\partial \overline{x_j}} + \frac{\partial \overline{u_j}}{\partial \overline{x_i}}\right)$ stands for strain rate tensor after filtering. Different from the Smgorinsky model, the WALE model can achieve the vanishing behavior of eddy viscosity near the solid boundaries and also capture accurately the strain and rotation rate at the smallest resolved length scales (Nicoud & Ducros, 1999). The eddy-viscosity defined by the WALE model is written as

$$\upsilon_T {=} \left(C_w \bar{\Delta}\right)^2 \frac{\left({S_{ij}}^d {S_{ij}}^d\right)^{3/2}}{\left(\bar{S}_{ij}\bar{S}_{ij}\right)^{5/2} + \left({S_{ij}}^d {S_{ij}}^d\right)^{5/4}} \tag{2.9}$$

where ${S_{ij}}^d$ is the traceless part of a strain rate tensor, and C_w is a constant parameter. This SGS model has been applied to various bluff body flow problems and shown good performance in modelling the turbulence at sub-grid scales (Dalla Longa *et al.*, 2019; Posa *et al.*, 2019; Zheng *et al.*, 2021). We therefore choose the WALE model in the present numerical studies to investigate the unsteady flow around the high-rise building.

2.2 Modal decomposition

The flow around the building immersed in the atmospheric boundary layer is complex, highly turbulent, and comprises both large-scale structures and fine-scale turbulent fluctuations. Considering these features of the flow, modal decomposition is applied to deconstruct the targeted unsteady flow field into physically important features, or dominant modes. In this work, two modal decomposition approaches, Proper Orthogonal Decomposition (POD) and Spectral Proper Orthogonal Decomposition (SPOD), are employed to reveal the characteristics of coherent structures in the wake.

Proper Orthogonal Decomposition, also called Principal component analysis in data science, can extract energetic coherent structures from an unsteady flow. This method, which decomposes the experimental or numerical flow field data into a minimal number of basis functions or modes to capture as much energy as possible, has been widely used in flows with pronounced coherent structures (Lumley, 1967; Rigas *et al.*, 2014; Evstafyeva *et al.*, 2017; Dalla Longa *et al.*, 2019).

For POD analysis, the input is generated by arranging the snapshots of scalar or vector fields with the temporal mean value removed in a chronological order (Taira *et al.*, 2017). This input matrix including the m time series flow field snapshots is obtained:

$$X = [\boldsymbol{q}_1 - \bar{\boldsymbol{q}}, \boldsymbol{q}_1 - \bar{\boldsymbol{q}}, \cdots, \boldsymbol{q}_m - \bar{\boldsymbol{q}}] = [\boldsymbol{x}_1, \boldsymbol{x}_2, \cdots, \boldsymbol{x}_m] \in \mathbb{R}^{n \times m} \tag{2.10}$$

where the vector $\boldsymbol{q}_k \in \mathbb{R}^n$ represents the snapshot at k time point and $\bar{\boldsymbol{q}}$ is the time-average value of the considered variable.

This fluctuation can be decomposed into a linear combination of the spatial basis modes and their corresponding temporal coefficients. POD analysis aims to obtain the basis modes that optimally represent the given flowfield data. The classical method to get the matrix of spatial POD modes Φ can be calculated through the eigenvalue decomposition (Taira *et al.*, 2017)

$$R\Phi = \Phi\Lambda, \tag{2.11}$$

where $R = XX^T \in \mathbb{R}^{n\times n}$ is the covariance matric of X, and $\Lambda \in \mathbb{R}^{n\times n}$ is the matrix including the corresponding eigenvalues along its diagonal. These eigenvalues representing the energy level of the corresponding mode are arranged in descending order within the Λ matrix.

However, this classical POD method is practically unavailable for the high-dimensional spatial dataset whose covariance matrix size is significantly large. In this project, the method of snapshots proposed by (Sirovich, 1987) is used to obtain POD modes for the flow around a high-rise building. The method of snapshots focuses on finding the eigenvectors and the eigenvalues for a matrix of size $m \times m$:

$$X^T X\Psi = \Psi\tilde{\Lambda}, \quad m \ll n, \tag{2.12}$$

where $\Psi \in \mathbb{R}^{m\times m}$ is the eigenvector of the above smaller eigenvalue problem and $\tilde{\Lambda} = diag\left(\lambda_1, \lambda_2, \cdots, \lambda_m\right) \in \mathbb{R}^{n\times n}$ contains the energy content. Based on the relationship between the eigenvectors of XX^T and $X^T X$, the POD modes can be further determined by

$$\Phi = X\Psi\tilde{\Lambda}^{-1/2}, \tag{2.13}$$

where $\Phi \in \mathbb{R}^{n\times m}$. The calculated basis spatial modes and the related coefficients are then used to investigate the coherent structures in the flow field. Compared to the classical POD method, the matrix $X^T X$ in the eigenvalue problem solved by the method of snapshots has a much smaller size, which significantly reduces the computational cost.

POD modes are ranked in terms of the modal energy to identify the most energetic coherent structures, but their corresponding temporal coefficients generally contain a mix of frequencies. Another model decomposition technique, Spectral Proper Orthogonal Decomposition(SPOD) proposed by Towne *et al.* (2018), addresses this issue. SPOD is an empirical method to identify frequency-resolved coherent structures oscillating at a certain frequency (Towne *et al.*, 2018; Schmidt *et al.*, 2018). The mutually orthogonal SPOD modes are ranked in terms of energy at each frequency. The method has been successfully applied to extract the spatial-temporal modes of a turbulent jet (Towne *et al.*, 2018), wind turbine flows (Schmidt & Colonius, 2020), and the wake behind a square FWMC (Yauwenas *et al.*, 2019). The procedure of SPOD analysis is detailed as follows.

The time-resolved flow matrix X is divided into n_b blocks and each block overlapped with the neighboring blocks consists of m_f snapshots. Regarding each block as a statistically independent realization based on the ergodicity hypothesis, the frequency-domain matrix of the i_{th} block can be obtained by performing discrete Fourier transform (DFT)

$$\hat{X}^{(i)} = \left[\hat{\boldsymbol{x}}_{\omega_1}^{(i)}, \hat{\boldsymbol{x}}_{\omega_2}^{(i)}, \cdots, \hat{\boldsymbol{x}}_{\omega_{m_f}}^{(i)}\right] \in \mathbb{R}^{n\times m_f}. \tag{2.14}$$

The frequency-domain data matrices of all blocks can be rearranged based on the resolved frequencies. A new data matrix at the k_{th} frequency can be written as

$$\hat{X}_{\omega_k} = \left[\hat{\boldsymbol{x}}_{\omega_k}^{(1)}, \hat{\boldsymbol{x}}_{\omega_k}^{(2)}, \cdots, \hat{\boldsymbol{x}}_{\omega_k}^{(n_b)}\right] \in \mathbb{R}^{n\times n_b}. \tag{2.15}$$

For this frequency, the cross-spectral density (CSD) matrix $\hat{X}_{\omega_k}\hat{X}_{\omega_k}^T$ is further formed, and the eigenvalue decomposition is performed on this matrix to calculate the SPOD modes at this frequency

$$\hat{X}_{\omega_k}\hat{X}_{\omega_k}^T\Phi_{\omega_k} = \Phi_{\omega_k}\Lambda_{\omega_k}, \tag{2.16}$$

where eigenvalues Λ_{ω_k} represent the corresponding energy levels.

In order to reduce the required computation and memory resources, the idea similar to the method of snapshots can also be used to get the SPOD modes at each frequency for high-dimensional spatial data (Towne *et al.*, 2018). An eigenvalue decomposition problem of size $n_b \times n_b$ is solved and then the SPOD modes can be obtained:

$$\hat{X}_{\omega_k}^T\hat{X}_{\omega_k}\Psi_{\omega_k} = \Psi_{\omega_k}\tilde{\Lambda}_{\omega_k}, \tag{2.17}$$

$$\Phi_{\omega_k} = X_{\omega_k}\Psi_{\omega_k}\tilde{\Lambda}^{-1/2}, \tag{2.18}$$

where $\Phi_{\omega_k} \in \mathbb{R}^{n\times n_b}$. The calculated SPOD modes are ranked following their corresponding eigenvalues $\tilde{\Lambda}_{\omega_k}$, and the dominant modes at the characteristic frequency can be further identified. This modal decomposition method is later employed in the thesis to gain insight into the coherent structures generated by the top-surface active controller and the impact of the controller on the wake.

Chapter 3

Attenuation of unsteady loading using feedback control

3.1 Introduction

Investigations into the flow around high-rise buildings have so far focused predominantly on aerodynamic forces (Obasaju, 1992; Tominaga *et al.*, 2008; Huang *et al.*, 2010; Yan & Li, 2015; Tominaga, 2015; Ricci *et al.*, 2018; Thordal *et al.*, 2019). However, to our knowledge, no existing studies clearly elucidate the wake structures around a CAARC high-rise building immersed in an atmospheric boundary layer. Additionally, although feedback control techniques have been successfully applied to bluff body flows in other contexts, we believe that there is no existing literature that investigates the application of feedback control for the attenuation of unsteady loading on a high-rise building immersed in an atmospheric boundary layer.

In the present chapter, we investigate numerically the use of feedback control strategies to attenuate the unsteady loading of a canonical high-rise building immersed in an atmospheric boundary layer with an oncoming wind normal to the wider side, which can provide a theoretical support for the practical application of this novel control. High-fidelity, wall-resolved Large Eddy Simulations (WRLES) are performed to investigate the unforced flow, offering fresh insights into the wake topology around the building as well as the effect of the atmospheric boundary layer. Two single-input single-output (SISO) feedback control strategies aiming to attenuate the building's unsteady loading are then developed. The first mimics the linear feedback control that has been successfully applied in other bluff body flows (Dahan *et al.*, 2012; Evstafyeva *et al.*, 2017; Dalla Longa *et al.*, 2017). The second employs the LMS adaptive control. This has not, to our knowledge, previously been employed to bluff body flows, even though it has been shown to be effective in combustion instability suppression (Billoud *et al.*, 1992; Evesque & Dowling, 2001) and boundary layer transition delay (Kurz *et al.*, 2013; Fabbiane *et al.*, 2017). The present study performs what we believe is the first application of a LMS adaptive control strategy to the wake of a bluff body.

This chapter presents the simulation set-up in section 3.2 followed by the flow structures of the unforced flow and the effect of the atmospheric boundary layer in section 3.3. The designed feedback control strategies and their effect on the unsteady wind loading are studied in section 3.4. Feedback control with reduced sensing area is further explored in section 3.5, before finishing with concluding remarks.

3.2 Simulations set-up and validation

The rigid CAARC standard tall building model proposed by Melbourne (1980) has a rectangular horizontal cross-section, with full-scale dimensions 30.48m (D) × 45.72m (B) × 182.88m (H). In the present simulation, a reduced-scale CAARC building model with a geometric scaling ratio of 1:400 was considered, which can mitigate the challenges

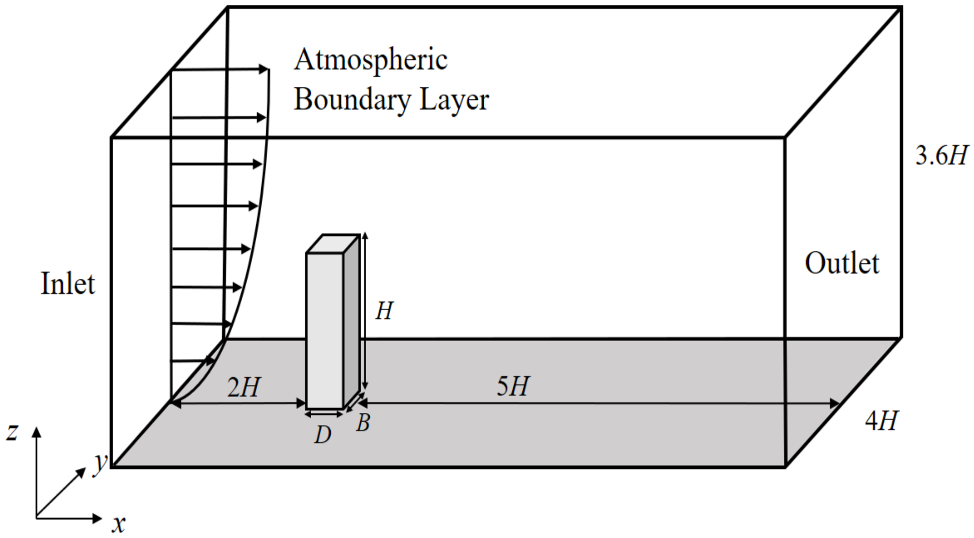

Figure 3.1: Flow set-up, showing the CAARC building model, ground, the atmospheric boundary layer and the computational domain

associated with high Reynolds numbers and is also consistent with the experimental investigation given by Ngooi (2018). The oncoming flow was taken to be normal to the wider side, B, of the building.

The computational domain used in this paper is shown in figure 3.1, with the domain cross-section being $4H$ (width) × $3.6H$ (height), slightly larger than that suggested by Architectural Institute of Japan (AIJ) (Tominaga *et al.*, 2008; Tominaga, 2015). The computational domain has its origin at the junction of the CAARC building model and the ground, centred on the building axis. The inlet boundary is $2H$ upstream of the front of the building and the outflow boundary $5H$ downstream of the rear of the building, the latter length ensuring that the wake behind the building can fully develop (Tominaga *et al.*, 2008). The resulting blockage ratio of the computational domain is 1.6%, less than the limitation of 3% suggested by Franke *et al.* (2011).

The flow simulations were performed using Large Eddy Simulations (LES). They used the open-source CFD software OpenFOAM, which solves the 3D Navier-Stokes equations using the finite volume method. The details of the solver have been described in Chapter 2. The Wall-Adapted Local Eddy viscosity (WALE) model (Nicoud & Ducros, 1999) was employed to model the subgrid-scale stresses.

No-slip boundary conditions were applied on the building surfaces and the ground. Free-slip conditions were enforced at the sides and top of the computational domain, and a convective condition was set at the domain outlet to avoid backflow. A turbulent velocity field which can realistically mimic the atmospheric boundary layer needed to be imposed as the inlet boundary condition. The required characteristics of this “target” boundary layer can be summarised through mean profile and turbulence requirements. In order to computationally generate the inflow velocity profile which closely matches the “target” mean flow and turbulent characteristics, the Synthetic Eddy Method (SEM), introduced by Jarrin *et al.* (2006) was used. Based on the classical view of turbulence as a superposition of coherent structures, this method decomposes a turbulent inflow plane into synthetic eddies. It performs well in reproducing the prescribed turbulence characteristics such as turbulent length and time scales.

Here, the “target” mean wind velocity profile was taken to be the power law (Melbourne, 1980; Huang *et al.*, 2005), written as

$$U = U_H \left(\frac{z}{H} \right)^{\alpha} \tag{3.1}$$

where H represents the height of the building, $U_H = 3m/s$ is the oncoming velocity at the height of the building and the exponent α was chosen to be 0.25. The Reynolds number based on the building width is $Re_B = 24000$. This is less than for full-scale building flows. However, it was suggested by Sohankar (2006) and Brun *et al.* (2008) that for cases with Re_B more than 20000, the transition from laminar boundary layer to turbulent shear layer occurs consistently at the flow separation point, i.e. the leading edge. The mean and the relatively large scale unsteady wake structures behind bluff body flows are known to change relatively little once the transition to turbulent shear layer is achieved close to the leading edge (Bai & Alam, 2018; Brun *et al.*, 2008; Sohankar, 2006), and so this suggests that a qualitatively representative wake can be achieved at a reasonable computational cost, and one which facilitates full resolution of the building boundary layers, rather than requiring less accurate wall models.

For the inlet turbulent fluctuations, the "target" features were characterised using the turbulence intensity profile, following AIJ standards (Tominaga *et al.*, 2008) and experimental data from Obasaju (1992), Ngooi (2018) and Huang *et al.* (2005). This profile is shown below, where $I(z)$ is the streamwise turbulence intensity at height z and I_H is the streamwise turbulence intensity at the height of the building.

$$I(z) = I_H \left(\frac{z}{H}\right)^{-\alpha - 0.05}. \tag{3.2}$$

I_H was set to 13% and the normalized turbulence integral length, L_H, at the height of the building was set to 0.95, similar to the wind tunnel tests conducted by Obasaju (1992), Ngooi (2018) and Huang *et al.* (2005).

The time-averaged velocity and turbulence intensity profiles for the turbulent inflow generated by the SEM are compared to the target profiles, given in equation 3.1 and equation 3.2 respectively, in figure 3.2. They both show good agreement with the target profiles, validating our use of the SEM to generate an inflow which closely approximates an atmospheric boundary layer.

The computational domain was discretized into an unstructured grid composed of trimmer cells and prism layer cells using StarCCM+, as shown in figure 3.3. The prism layers were used to refine the mesh close to the ground and the building, ensuring that the boundary layer can be properly resolved. A grid refinement study was conducted

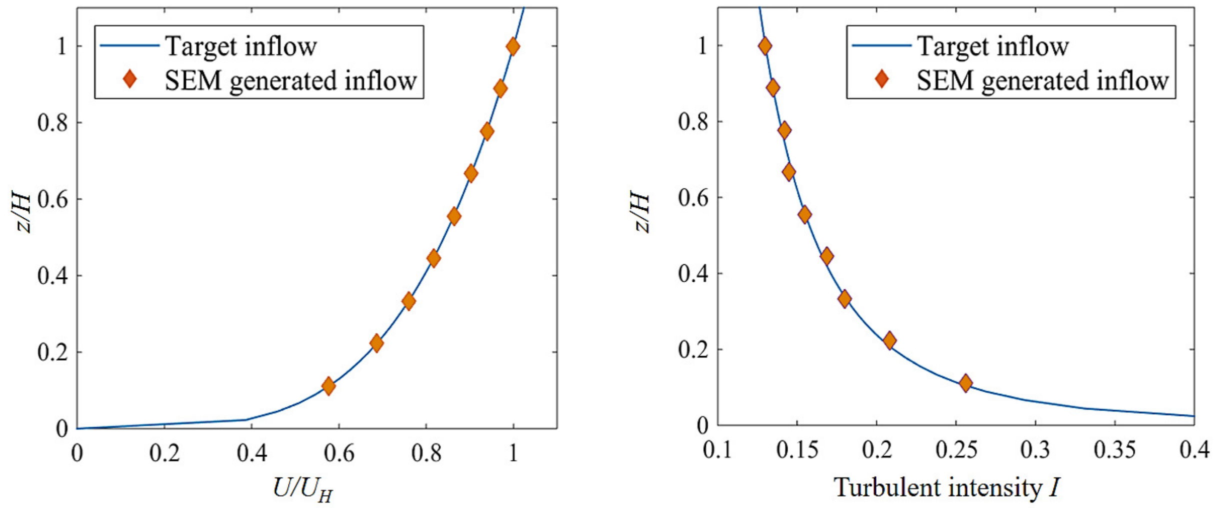

Figure 3.2: Profiles of normalized mean velocity and turbulence intensity generated by the SEM.

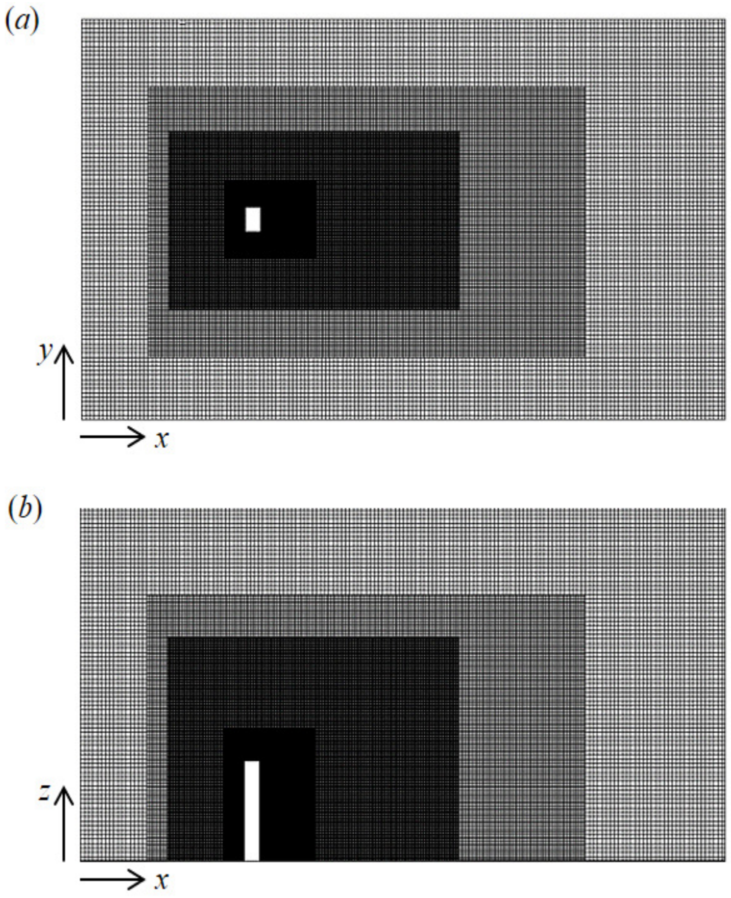

Figure 3.3: Baseline grids used in the simulation.(a) xy slice, top view. (b) xz slice, side view.

Case	Mesh size	$\overline{C_d}$	$C_{\sigma d}$	$\overline{C_l}$	$C_{\sigma l}$
Coarse	6.7 Million	1.29	0.19	0.0012	0.20
Baseline	18.4 Million	1.30	0.27	0.0003	0.29
Fine	24.3 Million	1.30	0.27	0.0003	0.28
Experimental	N/A	1.31	0.28	0	0.30

Table 3.1: Summary of the grid refinement study. The mean (overbar) and RMS (subscript σ) values of the aerodynamic force coefficients C_d and C_l are compared to experimental values from Obasaju (1992).

to identify the baseline mesh for this work. Two non-dimensional aerodynamic force coefficients are defined: the drag coefficient, C_d, and the lift coefficient, C_l:

$$C_d = \frac{F_x}{0.5\rho U_H^2 BH}, \qquad C_l = \frac{F_y}{0.5\rho U_H^2 BH}, \tag{3.3}$$

where F_x and F_y are respectively the alongwind (x-direction in figure 3.1) and cross-wind (y-direction in figure 3.1) aerodynamic forces on the building, and U_H is the mean wind velocity at the height of the top of the building. Numerical results from three different grid refinements were compared to the experimental data from Obasaju (1992) and are summarised in table 3.1. The three meshes adopt computational cells with identical sizes in the far field, with differences only in the cell size in their wake regions. It can be seen that the baseline mesh of 18.1 million cells is sufficiently fine to resolve the mean and fluctuating forces on the building accurately. It was therefore chosen for the main simulations in this study.

Figure 3.4 presents colour contours illustrating the spatial variation of y^+ around the building. The average value of y^+ for the baseline mesh remains below 1, consistent with the recommendation given by Saeedi & Wang (2016). The maximum CFL number in the simulation is dynamic and remains below 0.15, which ensures that the unsteady flow is temporally resolved. To further validate the accuracy of our simulations, figure 3.5 shows the comparisons of the mean and RMS of the pressure coefficient distributions

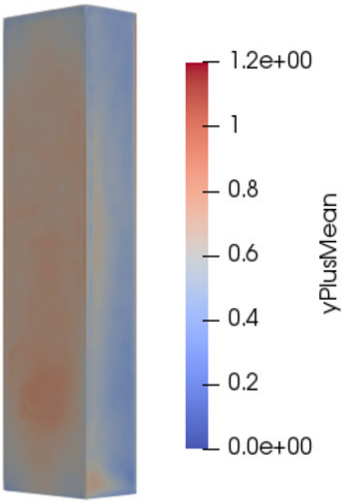

Figure 3.4: y^+ colormap on the surface of the building for the baseline mesh.

at $z = 2/3H$ to experimental studies. It can be observed that our numerical results match the experimental measurements very well for the mean and fairly well with some slight discrepancies for the RMS values. This further confirms the reliability of our simulations. All computations were performed using several hundred cores on either the Imperial College HPC facility or the UK computational facility, ARCHER.

3.3 Unforced flow features and effect of the atmospheric boundary layer

The flow field around the CAARC building immersed in the atmospheric boundary layer determines its unsteady loading. Understanding the structures of this flow is therefore important in order to choose appropriate actuation and sensing for feedback control. In this work, the statistics of 56 cycles of the spanwise antisymmetric vortex shedding are sampled for the unforced flow analysis, where the transient stage has been removed. The unforced time-averaged flow is first examined, after which the unsteady flow features are

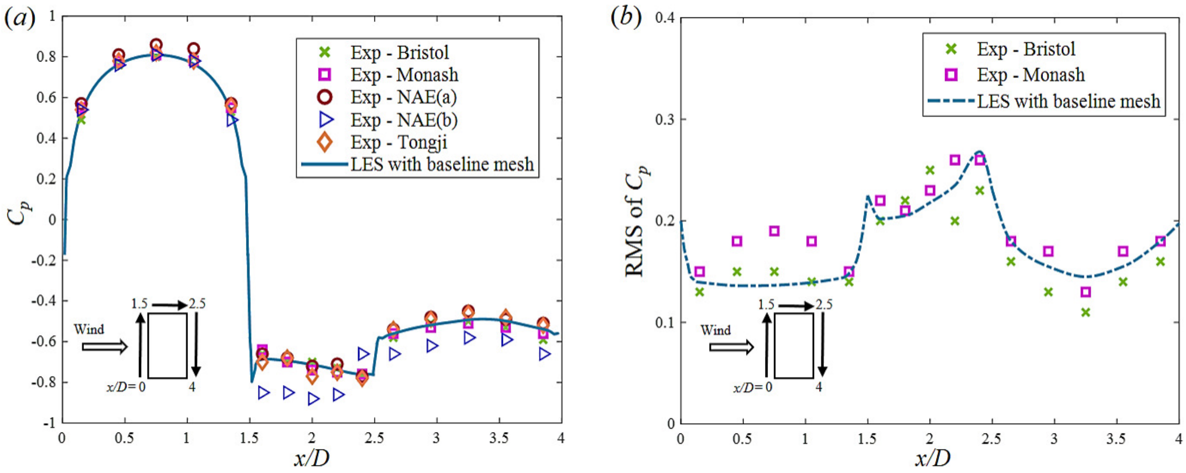

Figure 3.5: (a) Comparison of mean pressure coefficient distribution at $z = 2/3H$; (b) Comparison of RMS pressure coefficient distribution at $z = 2/3H$. The pressure coefficient $C_p = (p - p_\infty) / (0.5\rho U_H^2)$.

investigated. This is followed by analysis of the effect of the atmospheric boundary layer on the flow features via comparison to the case of the CAARC building immersed in a uniform inflow.

3.3.1 Time-averaged flow

The simulated time-averaged streamwise velocity field and streamlines around the high-rise building immersed in the atmospheric boundary layer are visualized in figure 3.6. The time-averaged wake is approximately symmetric in the horizontal slice shown. The flow separates at both leading edges of the building, forming a bubble on both side faces, with a large low-pressure recirculation region behind the building then established. Figure 3.6(b) shows the time-averaged velocity field on the xz plane at $y = 0$. The downwash flow from the free end of the building top meets with the upwash flow originating from the ground-building interface in the wake, and the interaction between these two flows and the spanwise vortex shedding results in a highly three-dimensional flow. For the flow around a high-rise building immersed in an atmospheric boundary layer, the saddle point is located above the mid-height of the building, much higher than for the FWMC flows with freestream inflow (Bourgeois *et al.*, 2011; Yauwenas *et al.*, 2019). This is because the atmospheric boundary layer engulfs almost the entire building, which weakens the downwash flow. From the streamlines in the yz plane at $x = 5B$ shown in figure 3.6(c), it can be observed that the tip vortices, generated by the interaction of the downwash flow and Von Karman vortex shedding, persist in the downstream region near the building top, leading to a dipole time-averaged wake structure (a pair of counter-rotating streamwise vortices) behind the CAARC building. This bears similarities to the flow over a FWMC with $L/W = 4$ (Bourgeois *et al.*, 2011; Yauwenas *et al.*, 2019), where the dipole vortex structure is also observed.

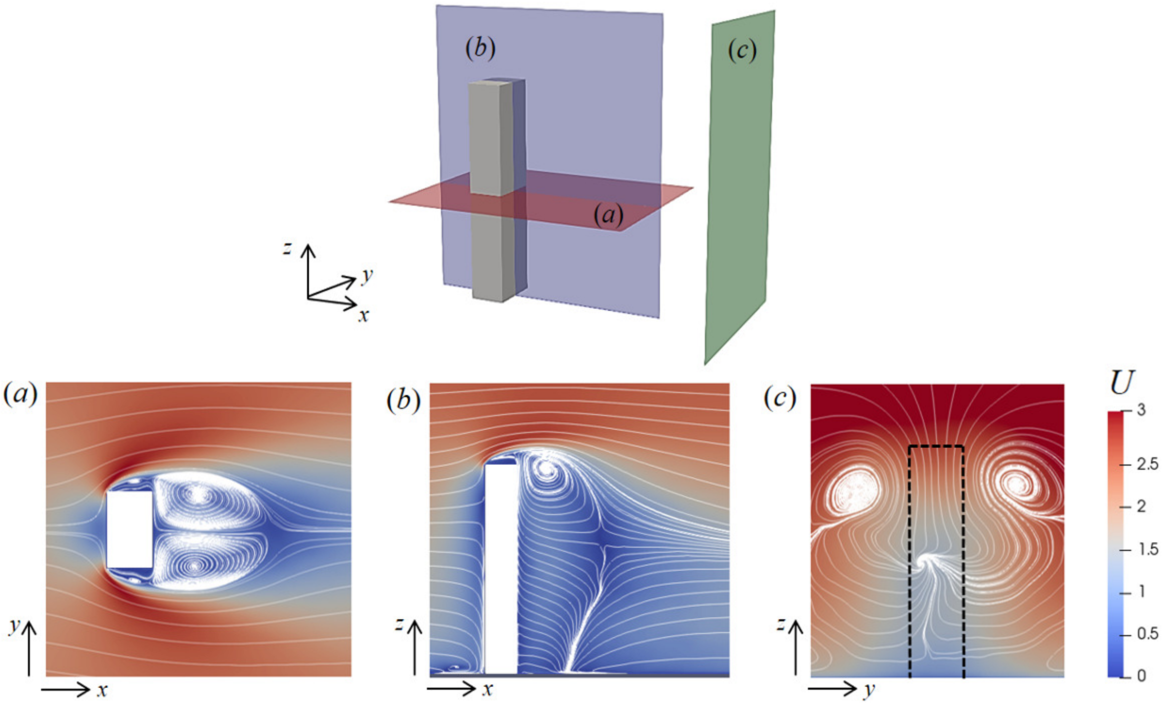

Figure 3.6: Time-averaged streamwise velocity field and projected streamlines. (a) Top view in the horizontal plane $z = 0.5H$, (b) side view in the symmetry plane $y = 0$, (c) downstream plane at $x = 5B$.

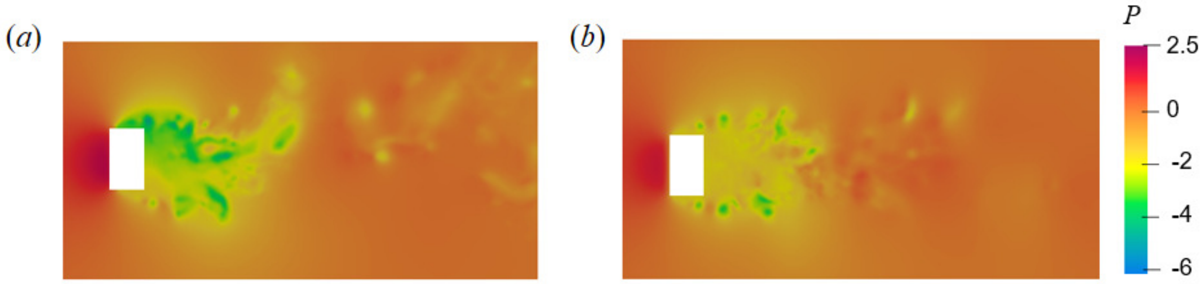

Figure 3.7: Instantaneous snapshots of pressure field at $z = 0.5H$. (a) Antisymmetric vortex shedding, (b) symmetric vortex shedding.

3.3.2 Time-varying Flow

The primary cause of the building's unsteady loading is the unsteadiness in the wake flow behind the building. This wake flow is complex and highly three-dimensional, exhibiting various coherent structures interacting with each other. As shown in figure 3.7, the simulations successfully capture the intermittent nature of the vortex shedding in the near wake. The instantaneous snapshots confirm two types of vortex shedding behaviour: (i) antisymmetric Von Karman-type periodic shedding as captured in figure 3.7(a) and (ii) symmetric arch-type vortex shedding as captured in figure 3.7(b), analogous to the intermittent vortex shedding for the finite-length cylinder wake reported by Wang & Zhou (2009); Sattari *et al.* (2012) and Yauwenas *et al.* (2019). The near wake exhibits these two vortex shedding behaviours alternately.

In the present unforced case, switching between antisymmetric and symmetric vortex shedding occurs randomly during the simulations. To further understand this switching phenomenon, the flow field during a switch was investigated in more detail. Figure 3.8 shows 3D snapshots of the pressure iso-contours at different time points, exhibiting the switching process from antisymmetric vortex shedding to symmetric. These time points correspond to the switching process highlighted by the circles in figure 3.9. The downwash flow near the free-end caused by flow separation interacts strongly with the

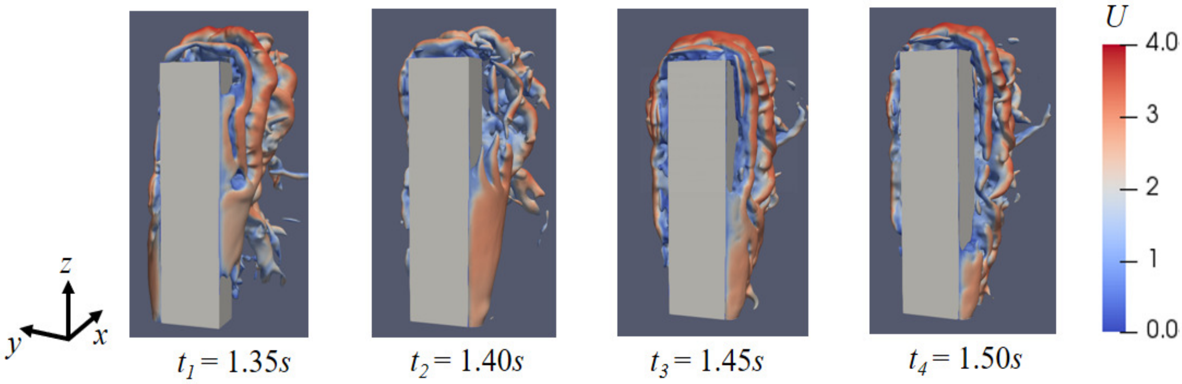

Figure 3.8: Instantaneous snapshots of iso-contours of pressure taken at $Cp = -0.2$ coloured by velocity. Flow in the $+x$ direction.

spanwise vortex structures near the top, and Wang & Zhou (2009) suggested that the free-end downwash flow could suppress the antisymmetric vortex shedding and promote the formation of symmetric vortices. Under the influence of the downwash flow, the switching from antisymmetric to symmetric vortex shedding occurs near the top of the building first. Figure 3.8 exhibits the flow structure at the initial stage of this switching. At t_1, shed vortices can be observed on both two sides of the building near the top, showing the feature of symmetric vortex shedding, while the flow lower down the building remains antisymmetric. As time progresses, the symmetric vortex shedding gradually extends down the building, with only the near ground flow remaining antisymmetric at t_4. Therefore, we observe that the switching from antisymmetric to symmetric vortex shedding does not occur in the entire coherent wake structure simultaneously, but appears first at the top of the building, and then gradually transmits towards the near ground.

Figure 3.9 shows the time history of the pressure coefficient on the left and right side faces of the building at different heights, where the transient stage has been removed. The symmetrical vortex shedding is seen to emerge near the top of the building first and then extend towards the near ground, lasting longer near the top of the building.

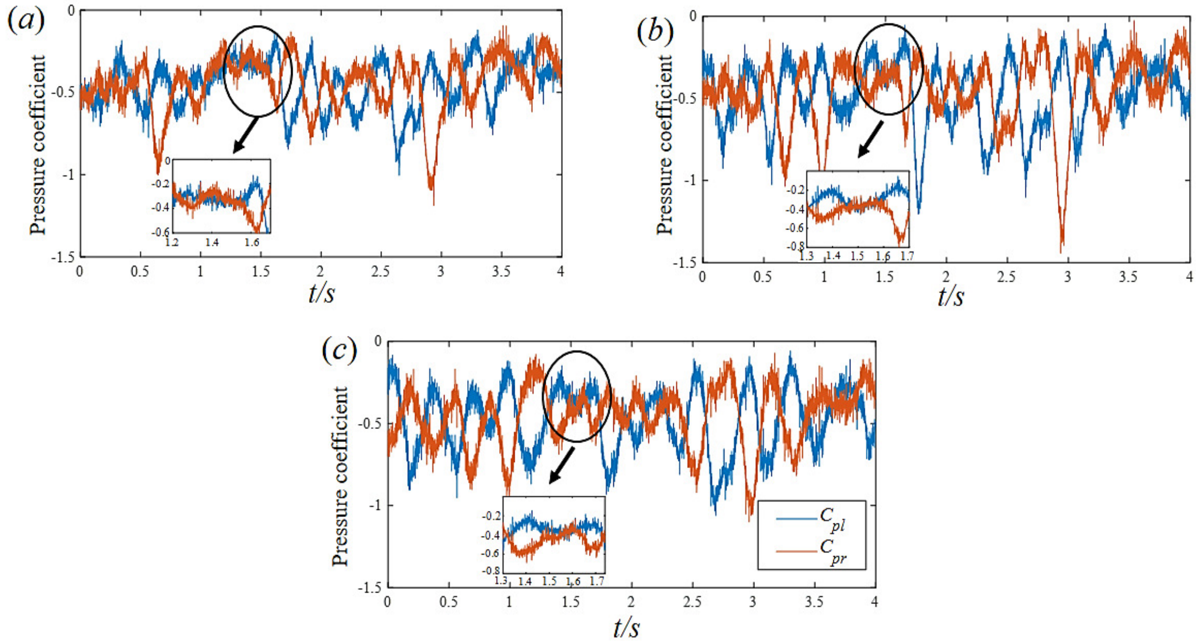

Figure 3.9: Variation of instantaneous pressure coefficient on side faces at (a) $z = 0.9H$; (b) $z = 0.5H$; (c) $z = 0.2H$, where C_{pl} and C_{pr} are the pressure coefficient averaged over a line on left and right side faces at every height. Black circles indicate the symmetric vortex shedding.

Moreover, figure 3.9 reveals that the appearance of the symmetric vortex shedding process is more like an interruption, with the antisymmetric vortex shedding dominating most of the time. Interestingly, immediately prior to and after intervals of symmetric vortex shedding, the antisymmetric vortex shedding ends and restarts with the same orientation. Streamlines for the initial symmetric and symmetric-back-to-antisymmetric shedding are shown in figure 3.10 corresponding to times t = 1.5 and 1.6s in figure 3.9(b). In both images of figure 3.10, the larger antisymmetric vortex immediately behind the building is closer to side A. Of the small counter-rotating vortices on sides A and B, the strength of the one on side A appears suppressed by the large shed vortex behind the building and is the slightly weaker of the two.

To further investigate the coherent structures present, modal decomposition was applied to snapshots of the 3D pressure field for the near wake behind the building. To account

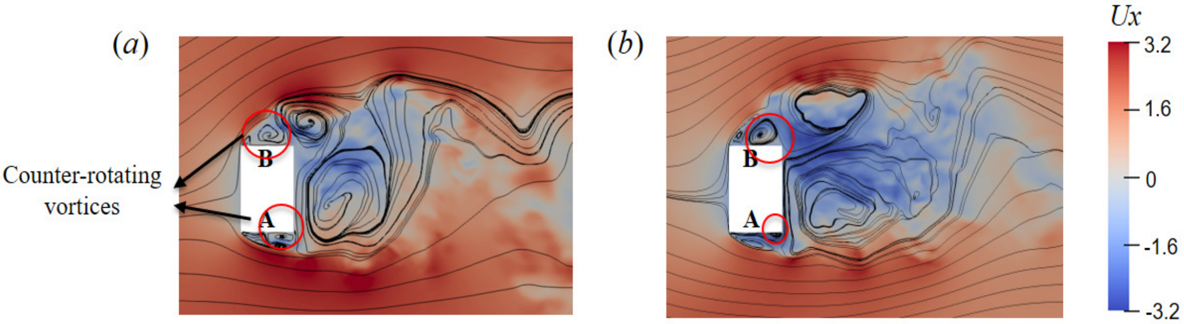

Figure 3.10: Instantaneous streamlines and streamwise velocity field in horizontal slices at $z = 0.5H$. (a) Initiation of symmetric vortex shedding at $t = 1.5s$; (b) Transition from symmetric back to antisymmetric vortex shedding at $t = 1.6s$. Red circles indicate the counter-rotating vortices.

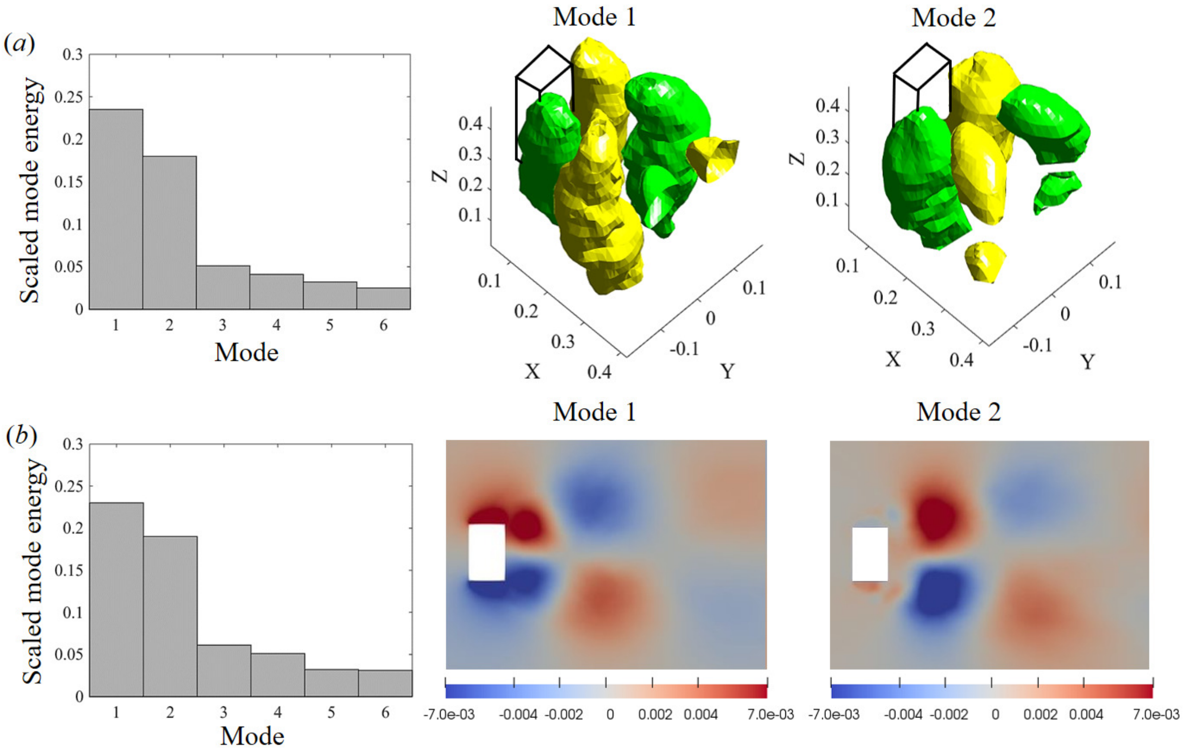

Figure 3.11: First two POD modes of the pressure fluctuation. (a) 3D POD modes and their corresponding spatial structures are plotted using the iso-contour of dominant amplitude. (b) POD modes plotted on the horizontal slice at $z = 0.5H$.

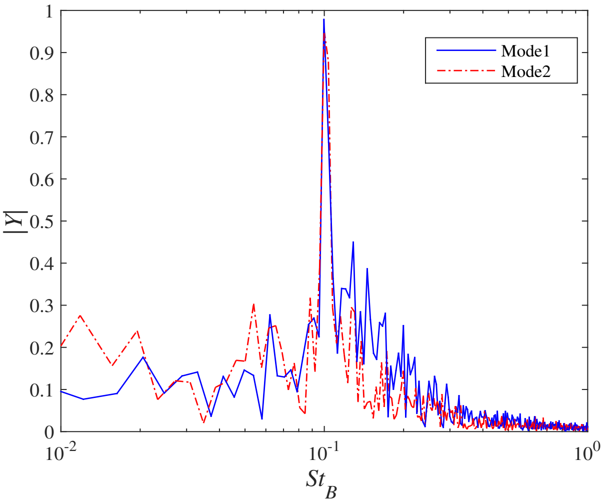

Figure 3.12: Normalized spectra of the first two 3D POD modes.

for the observation that the symmetric vortex shedding behaviour occurs intermittently in short bursts, exhibiting no obvious periodicity (Bisset *et al.*, 1990; Zhou & Antonia, 1993; Porteous *et al.*, 2017; Wang *et al.*, 2017), proper orthogonal decomposition (POD) was chosen to obtain the most energetic wake modes in preference to methods which yield structures at a given frequency, such as dynamic mode decomposition (DMD) or spectral POD (Taira *et al.*, 2017). Snapshots of the pressure field with its mean component subtracted from the sampled data were analysed. The results are summarized in figure 3.11, showing the energy content of first six pressure POD modes. The first two modes, which account for nearly 40% of the overall energy, are shown in figure 3.11(a). They exhibit coherent vortex structures that are anti-symmetric about the wake centerline over the entire building height, confirming that the large scale Von Karman antisymmetric vortex shedding mode is prevalent in the near wake. The spectra of the first two modes are shown in figure 3.12, exhibiting peaks at the antisymmetric vortex shedding frequency, $St_B = 0.1$. For a horizontal slice at $z = 0.5H$, the first two modes of the pressure field are shown in figure 3.11(b). The anti-symmetric spanwise vortex shedding with separation near both leading edges is again observed.

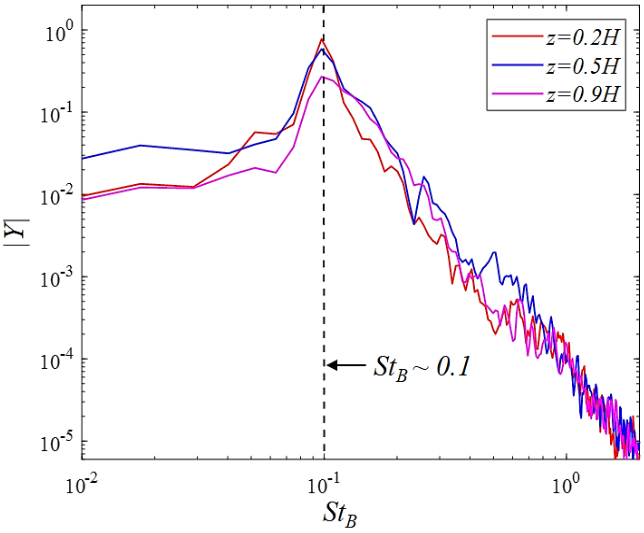

Figure 3.13: Power spectral density of C_l at different heights of the CAARC building, where C_l stands for the coefficient of the y-direction integrated pressure force at every height and $St_B = fB/U$ is the Strouhal number based on the building width, B. Filtering is applied using pwelch function for clarity.

In order to design a controller which attenuates the unsteady loading via attenuation of wake unsteadiness, it is necessary to know the frequency content of the unsteady fluctuations. The normalized PSD of the side-force (lift) coefficient, C_l, at different heights of the building is shown in figure 3.13. The main spectra peak in C_l occurs at the same frequency of $St_B = 0.1$ along the entire building height, in good agreement with the dominant frequency reported in the experimental study of Obasaju (1992). Interestingly, it can be found that the peak frequency determined by the spectrum of C_l is consistent with the antisymmetric vortex shedding one. This illustrates that even though the average velocity and turbulence intensity of the oncoming flow vary with height, the flow forms an overall vortex structure, with a consistent dominant vortex shedding frequency, as indicated by the 3D POD modes.

3.3.3 Effects of the atmospheric boundary layer

As many studies have considered a square FWMC in the presence of a uniform inflow, it is insightful to explicitly consider the effect of the atmospheric boundary layer on the flow features. This is now achieved by performing a simulation with a uniform oncoming flow incident on the CAARC building. The same baseline mesh as for the atmospheric boundary layer case was used, and a steady uniform velocity profile corresponding to $Re_B = 24000$ was set as the inlet boundary condition. The boundary layer was set to zero height at the inlet, and a very thin boundary layer relative to the atmospheric boundary layer developed between the inlet and the building, with thickness less than 10 % of the building height.

The r.m.s. value for C_l in the uniform inflow was found to be 0.038, significantly lower than the value for the atmospheric boundary layer flow of 0.29. The spectra of C_l is compared for the atmospheric boundary condition and uniform inflow in figure 3.14(a); the peak frequencies are very close, both corresponding to antisymmetric vortex shedding. The PSD spectra of C_d are compared in figure 3.14(b). It is observed that for the atmospheric boundary layer flow, the peak occurs at the low frequency of $St_B \sim 0.02$, in good agreement with the experimental data from Obasaju (1992). However, this spectral peak is not seen in the uniform inflow case, which is consistent with the suggestion by Obasaju (1992) and Kwok (1982) that this peak is associated with the inflow turbulence rather than the wake.

Figure 3.15 shows the pressure fluctuations on the side faces of the building in the atmospheric boundary layer case and the uniform inflow case. C'_{pl} and C'_{pr} denote the fluctuations of the pressure coefficient on the left and right side faces respectively; the scatter plots show the instantaneous results of 40,000 samples. These scatter plots reflect the symmetry of fluctuations for horizontal slices at different heights.

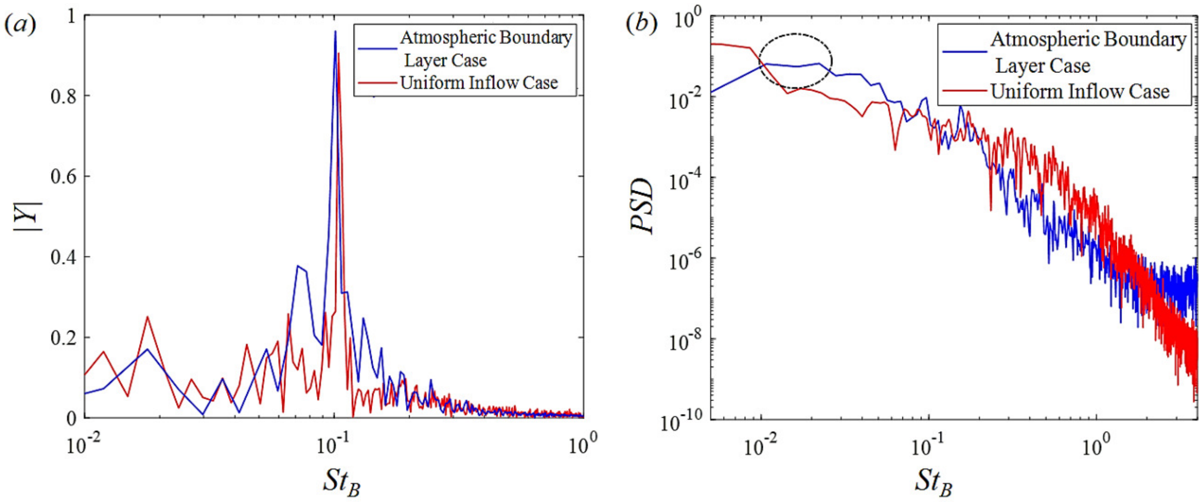

Figure 3.14: (a) Normalized spectra of the building's side force fluctuation, C_l. (b) Power spectral density of C_d of the building with two inflow conditions. Filtering is applied using pwelch function for clarity.

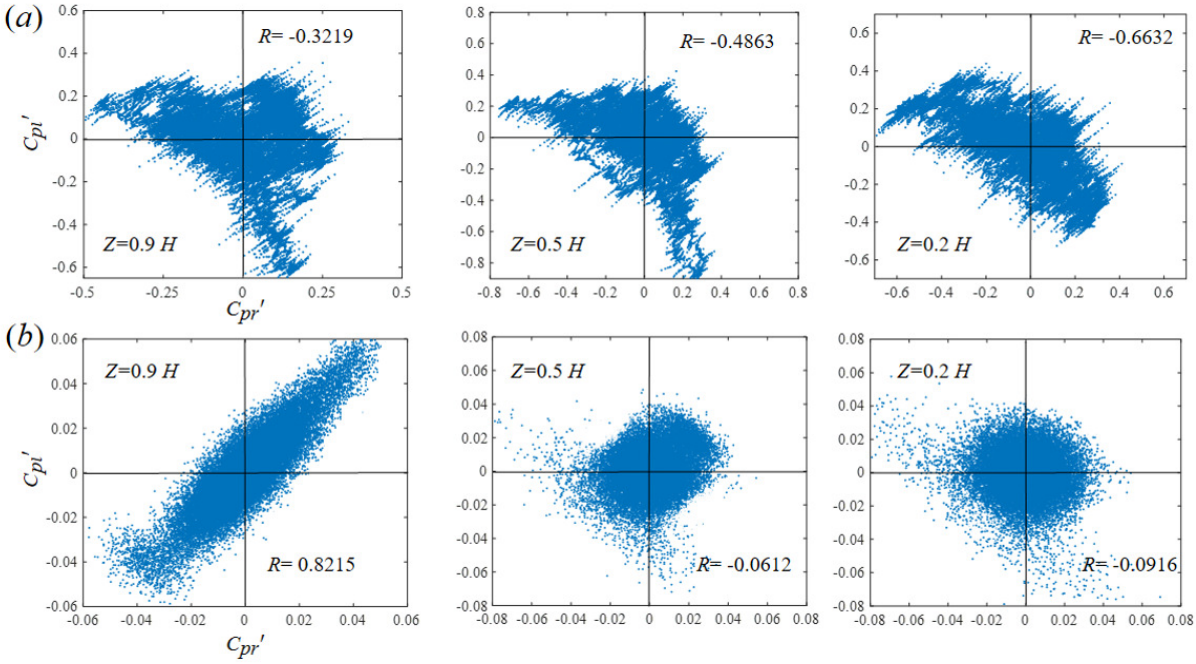

Figure 3.15: Scatter plot for the fluctuation of the pressure coefficient on the building side faces with (a) atmospheric boundary layer inflow and (b) uniform inflow at different heights.

For the uniform inflow, at $z = 0.9H$, i.e. near the top, most scatter points are located in the first and third quadrants, with the correlation coefficient R between C'_{pl} and C'_{pr} being 0.8215. Thus the pressure fluctuations on opposing side faces are in-phase most of the time, indicating that symmetric vortex shedding dominates. However, for the building immersed in the atmospheric boundary layer, the scatter plot slants the other way, with the pressure fluctuations on two opposing faces being negatively correlated at $z = 0.9H$, with correlation coefficient -0.3219. Similarly at $z = 0.5H$ the the correlation coefficients between C'_{pl} and C'_{pr} are -0.4863 for the atmospheric boundary layer inflow and -0.0612 for the uniform inflow, while at $z = 0.2H$ they are -0.6632 and -0.0916 respectively. All of this indicates that the presence of the atmospheric boundary layer enhances the antisymmetric vortex shedding behaviour and inhibits the symmetric vortex shedding behaviour compared to the uniform inflow. The tendency to the antisymmetric behaviour is stronger close to the ground for both flows.

3.4 Feedback Control

We now seek to develop and test active feedback control techniques to attenuate the unsteady loading of the CAARC high-rise building in an atmospheric boundary layer flow. The chosen actuator and sensor signals are first presented, after which two feedback control strategies are described. This is followed by the presentation of the system identification and the implementation of the feedback controllers in numerical simulations.

3.4.1 Choice of sensor signals

As the aim of feedback control is to attenuate the unsteady loading on the building, we seek a sensor signal that is capable of capturing this unsteady loading. The sensor should furthermore be located on the building surfaces, for future practical applicability, and should ideally require measurements on as few of the building surfaces as possible.

Kwok (1982), Liang *et al.* (2002) and Gu & Quan (2004) indicated that the wind-induced structural response of super-tall buildings in the crosswind direction is usually much larger than the alongwind one. Hence, the present study will focus on attenuating the crosswind loading (what is termed the fluctuating side-force coefficient). While the unsteady lift coefficient can be measured directly using pressure sensors on the two side surfaces of the building, it may also be possible to exploit the dominance of the antisymmetric vortex shedding mode in the wake to sense only on the building base (rear face). A possible choice of sensor signal is that of the vertically antisymmetric component of the base pressure force, which can be obtained by taking the integrated value of the pressure on the base and counting as negative the values on one horizontal half, as shown schematically in figure 3.16(a). This choice would be consistent with that for other bluff body flows dominated by anti-symmetric vortex shedding (Flinois & Morgans, 2016; Dalla Longa *et al.*, 2017), and involves pressure measurement on just one of the five exposed building surfaces.

Figure 3.16(b) compares the spectra of the building's variations in C_l and the anti-symmetric base pressure force. Both the sensor signal and C_l exhibit a narrow peak at $St_B = 0.1$, confirming that the proposed sensor signal captures the main vortex shedding features of the unsteady loading. As a further check, the cross power spectral density between C_l and the antisymmetric pressure force was found to exhibit a magnitude peak value of 0.8 at $St_B = 0.1$, confirming significant coherence between C_l and antisymmet-

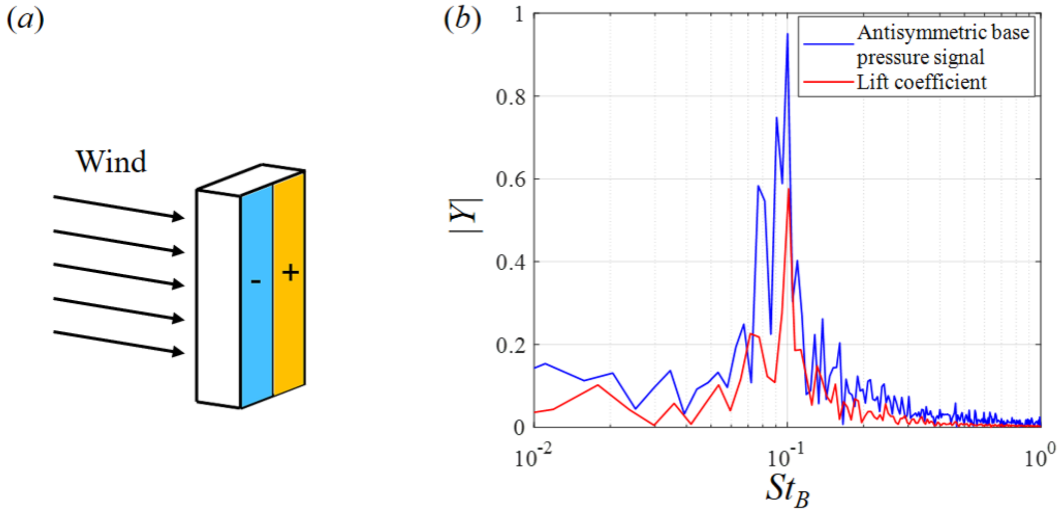

Figure 3.16: (a) Schematic of the antisymmetric base pressure force signal. (b) Normalized FFT spectra of the building's side force fluctuation, C_l, and the antisymmetric base pressure force signal, all in the absence of any actuation.

ric base pressure force. Thus the antisymmetric base pressure was chosen as the sensor signal for feedback control.

3.4.2 Choice of actuator

We seek an actuator strategy which has the spatial location, spatial form and control authority to attenuate the unsteady loading. The strategy should also be implementable in real experiments outside of the wind or water tunnel, even though the present study uses computational flow simulations as a test-bed.

The unforced flow shown in figure 3.11(b) reveals that the antisymmetric vortex shedding that is the main cause of unsteadiness involves large scale flow separation from the leading edges of the building. This suggests that actuation along these leading edges will have good control authority. By choosing the signals on either edge to be out of phase with one another, the antisymmetric nature of the vortex shedding can be accounted for.

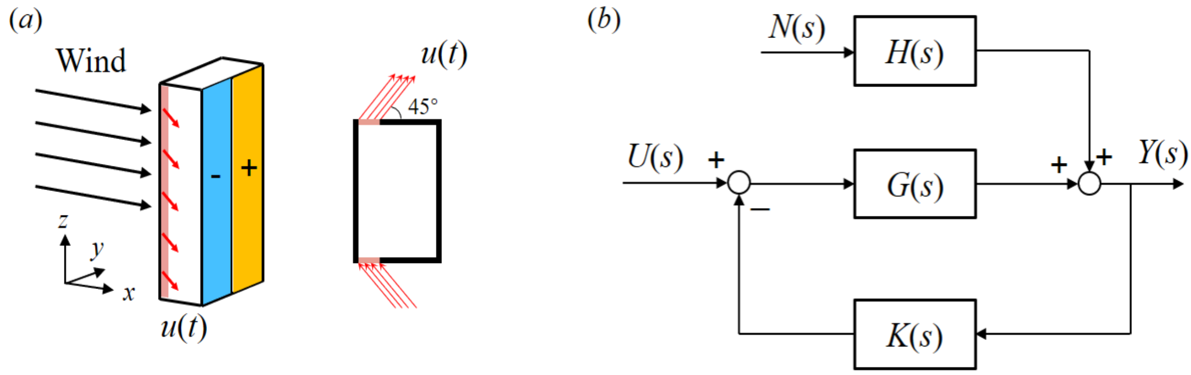

Figure 3.17: (a) Setup of the body-mounted sensing and actuation. (b) Frequency domain model underpinning the linear feedback control strategy, with s denoting the Laplace transform variable.

We therefore choose actuation in the form of synthetic slot jets, implemented near the leading edges of the building. The synthetic jets extend along the entire cylinder span (height) with a slot width of 0.04B and an injection angle of 45°, as shown in figure 3.17(a). The two synthetic slot jets located on different lateral edges are out of phase and operate simultaneously.

3.4.3 Linear control strategy

A linear SISO feedback controller is now designed, whose aim is to attenuate the sensor signal fluctuations and thus attenuate the unsteady loading on the building.

The feedback control approach is summarised in the schematic in figure 3.17(b). Fluctuations in the antisymmetric base pressure sensor signal, $Y(s)$, occur due to both natural disturbances in the unforced flow, $N(s)$, and due to the response to actuation, $U(s)$, where $s = i\omega$ is the Laplace transform variable. The transfer functions $H(s)$ and $G(s)$ are those describing how the sensor signals respond to the natural disturbances and actuation respectively - they are initially unknown but can be identified if needed. It then follows that the sensor signal in the presence and absence of control can be written as

$$Y(s)_{withoutcontrol} = U(s)G(s) + N(s)H(s) \tag{3.4}$$

$$Y(s)_{withcontrol} = \frac{U(s)G(s) + N(s)H(s)}{1 + G(s)K(s)}. \tag{3.5}$$

The ratio of sensor signal fluctuations with and without control is then given by

$$\left| \frac{Y(s)_{withcontrol}}{Y(s)_{withoutcontrol}} \right| = \frac{1}{|1 + G(s)K(s)|} = |S(s)| \tag{3.6}$$

where $S(s)$ is what is known as the sensitivity transfer function (Golnaraghi & Kuo, 2017). Thus, by designing the frequency response of $|S(i\omega)|$ to be less than unity at the frequencies most relevant to the sensor fluctuations, attenuation of the sensor signal fluctuations at these frequencies will be achieved. The steps involved in this process are (i) identifying the frequency response for the transfer function $G(s)$ and (ii) designing a feedback controller, $K(s)$, such that $|S(i\omega)| < 1$ over the most important frequencies, which are those for which the spectra in figure 3.16(b) exhibits high values.

This approach to feedback control for sensor signal attenuation has been successfully implemented in other flow control applications (Dahan *et al.*, 2012; Dalla Longa *et al.*, 2017; Evstafyeva *et al.*, 2017). It should be noted that some fundamental limits on the shape of $|S(i\omega)|$ exist, including that $|S(i\omega)| < 1$ cannot be achieved over all frequencies. A "waterbed" effect exists by which it being less than unity over some frequency range implies that it will exceed unity over other frequency ranges (Golnaraghi & Kuo, 2017).

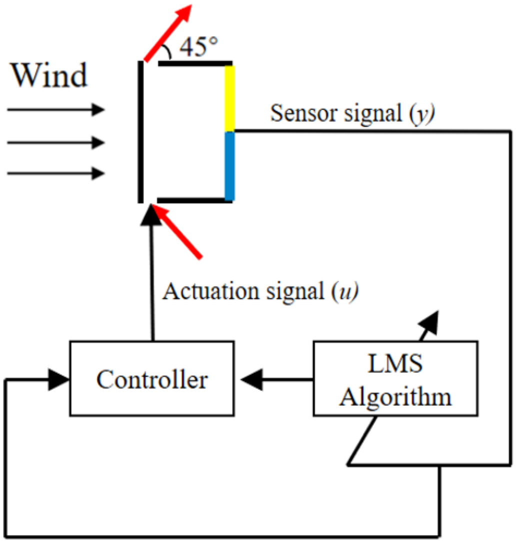

Figure 3.18: Schematic for the LMS feedback control strategy.

3.4.4 LMS control strategy

The LMS controller is an adaptive controller whose parameters are optimized by the LMS algorithm. This algorithm aims at minimizing the mean square of the error signal. It has been effective in both combustion instability control (Billoud *et al.*, 1992; Evesque & Dowling, 2001) and transition delay control (Kurz *et al.*, 2013; Fabbiane *et al.*, 2017). As the aim is to attenuate the high-rise building's side force fluctuations, the sensor signal y, given by antisymmetric base pressure fluctuations, is chosen as the error signal in this LMS algorithm.

The configuration of the LMS feedback control is shown in figure 3.18. The actuation signal to be generated by the LMS-controller is proscribed by an infinite-impulse-response (IIR) filter (Widrow *et al.*, 1977)

$$u(t) = \sum_{i=0}^{n-1} a_i(t) y(t - idT) + \sum_{j=1}^{m} b_j(t) u(t - jdT) \tag{3.7}$$

where $u(t)$ and $y(t)$ are the time-discrete actuation and sensor signals respectively, and

dT is the control sampling interval time. The computation for the coefficients a_i and b_j are the kernels of this adaptive controller. The LMS algorithm is employed to dynamically update these controller coefficients at each timestep in order to minimize the mean square of the sensor signal y, as follows

$$\begin{aligned} a_i(t+dT) &= a_i(t) - \mu y(t)\delta_i(t) \\ b_j(t+dT) &= b_j(t) - \mu y(t)\gamma_j(t) \end{aligned} \tag{3.8}$$

where μ is the convergence step-length and

$$\begin{aligned} \delta_i(t) &= Dy(t-idT) + \sum_{k=1}^{m} b_k(t)\delta_i(t-kdT) \\ \gamma_j(t) &= Du(t-idT) + \sum_{k=1}^{m} b_k(t)\gamma_j(t-kdT) \end{aligned} \tag{3.9}$$

D, named the auxiliary path in the LMS algorithm (Evesque & Dowling, 2001; Fabbiane *et al.*, 2017), is the transfer function describing the effect of actuation on the sensor signal. Note that this method is not completely model free as D needs to be determined. In the current work, the open-loop transfer function $G(s)$ obtained in the linear controller design is adopted as the auxiliary path D. The feedback coefficient b_j might be updated adaptively to some values that drive the IIR filter towards instability and cause divergence of the LMS algorithm. An efficient method, proposed by Evesque & Dowling (2001), that checks the stability of the IIR filter and resets the coefficients if unstable, is implemented to ensure the convergence of the LMS controller.

3.4.5 System identification

It is clear from the above descriptions that a low-order linear model for $G(s)$ must be identified in order to design both feedback controllers. Note that $H(s)$ in figure 3.17(b) does not need to be identified.

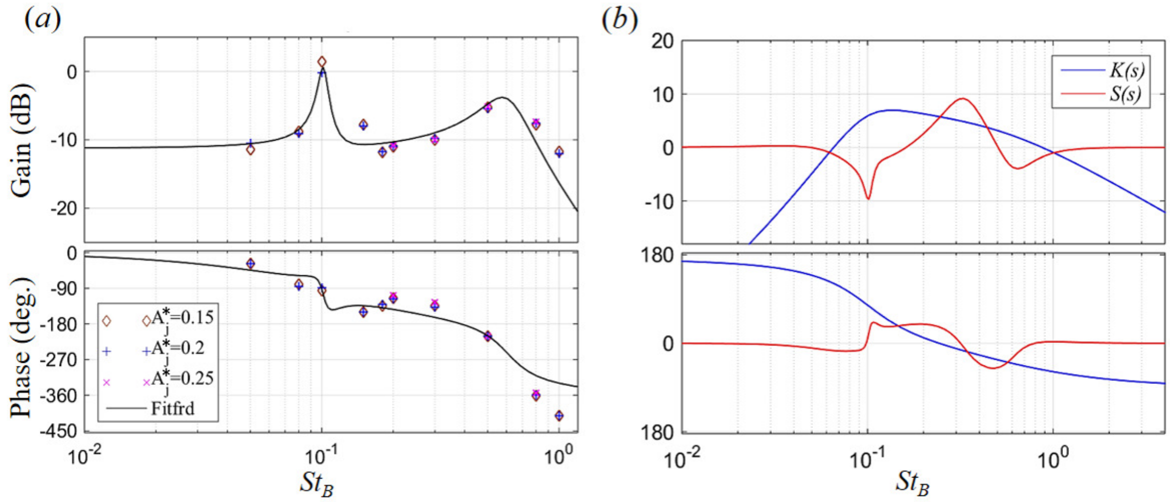

Figure 3.19: Frequency response: gain and phase shift for (a) system identification data resulting from open-loop harmonic forcing as well as fifth order fit from Matlab `fitfrd` command (b) the designed controller $K(s)$ and sensitivity function $S(s)$.

If we assume (we can later check) that the sensor response induced by open-loop forcing is approximately dynamically linear, $G(s)$ can be identified through linear system identification. Different actuation forcing signals can be applied in order to perform system identification, but the most intuitive, that of purely harmonic open-loop forcing, $U(t) = A_j^* U_H \sin(2\pi f_j t)$, over a relevant range of frequencies, f_j, allows us to obtain high-quality frequency response data while also facilitating a check on the assumption of dynamic linearity, through the ability to vary the amplitude. Based on the spectra of figure 3.16(b), the open-loop forcing frequency range was chosen to be $0.05 \leq St_B \leq 1$, with amplitudes ranging from 0.15 to 0.25 considered.

For the harmonic forcing simulations, the harmonic actuator signal was applied and the sensor signal measured. Once transients in the sensor signal had decayed to low levels, the sensor signal was recorded and the gain and phase shift of the open-loop response extracted using spectral analysis. The results, shown in figure 3.19(a), firstly confirm that the frequency response varies little with forcing amplitude, A_j, for all frequencies across the considered range. Hence the response of the sensor signal to the forcing can be considered dynamically linear. The average gains and phase shifts across the different forcing amplitudes are calculated, and the `fitfrd` MATLAB command used to fit the frequency-domain response data with a fifth order state-space model, as shown in figure 3.19(a).

3.4.6 Controller design and implementation

Linear controller design

To suppress the fluctuations in the sensor signal, the feedback controller, $K(s)$, is designed such that the magnitude of the sensitivity transfer function in equation 3.6 is less than unity over the frequency range where the wake exhibits significant dynamics. Based on the unforced spectra in figure 3.16(b), the main frequency to target for attenuation is $St_B = 0.1$.

Conventional loop-shaping is used to design the feedback controller, $K(s)$, to achieve this. The final feedback controller is a combination of a first-order high-pass filter and a second-order band-pass filter, written as

$$K(s) = \frac{167.7s^2}{s^3 + 100.5s^2 + 1684s + 23520} \tag{3.10}$$

The gain and phase shift of the controller, $K(s)$, along with the resulting sensitivity, $S(s)$, are shown in figure 3.19(b), where it can be seen that $S(s)$ <1 is achieved at and around $St_B = 0.1$.

LMS controller design

In terms of the LMS controller, a second-order IIR filter is used to generate the controller signal, i.e. $m = n = 2$. The convergence step-length μ has been chosen as a constant, with its value less than the upper bound, $1/(m+1)\sigma_y^2$, to avoid LMS algorithm divergence (Madisetti, 1997). The open loop transfer function $G(s)$, obtained through linear system identification is adopted as the auxiliary path D. In the initial stage of adaptive updating of controller coefficients, the LMS controller may produce large actuation amplitudes that could induce the divergence of the numerical iterations, thus a saturation limit of the actuation signal is applied.

Effect of feedback controllers

The controller was implemented in discrete-time format in the LES simulations in order to test its performance. When implementing the feedback flow control into the flow simulations, the actuators, whose signal at each timestep is generated following the variation of the sensor signal, require a time-varying boundary condition. Here, the plugin SWAK4FOAM (SWiss Army Knife for OpenFOAM) library allowing user-defined equations for boundaries was used.

The effect of the linear and LMS controllers on the sensor signal and the lift coefficient are shown in figure 3.20. Both controllers are effective in successfully attenuating the sensor signal fluctuations over the targeted frequency range, although high frequencies are amplified with the LMS controller. RMS fluctuations in C_l were correspondingly reduced by approximately 38% and 17% via the linear and LMS controller respectively, as shown in figure 3.20(b) and (d). In order to understand the mechanism of our controller, a POD analysis of the unforced and controlled flows based on the fluctuating kinetic energy was conducted to illustrate the difference in their unsteady flow structures. Figure 3.21

shows the streamwise velocity components of the first POD mode at $z = 0.5H$ for the feedback controlled flows compared to the unforced flow. It is observed that the center of the coherent structures, which is located at around $x/B = 1.2$ in the unforced flow, moves toward around $x/B = 1.6$ under the effect of the linear feedback controller. The linear feedback controller pushes the dominant coherent structures corresponding to antisymmetric vortex shedding further downstream, while the LMS controller only mildly affects the antisymmetric vortex shedding. Overall the linear feedback controller outperforms the LMS one with regard to the attenuation of the side-force fluctuation. The changes to the time-averaged flow field after implementing feedback control are shown in figure 3.22. The recirculation region has been extended in the streamwise direction, in a similar manner as for the D-body flow investigated by Dalla Longa *et al.* (2017). In a summary, the controller delays the formation of dominant vortices, which can further reduce the pressure fluctuations on the building caused by these vortices.

The aim of the LMS algorithm is to minimize the mean square of the error signal. In this work, the performance of the LMS controller is effective but not as good as for the linear controller. This may be attributed to the way in which the auxiliary path was prescribed. As described in section 3.4.4, our approach employed an offline system identification based on the assumption of dynamic linearity. It may be the case that this approach does not sufficiently account for nonlinearity nor changes in the auxiliary path as control is implemented. A more accurate online estimate of this auxiliary path may improve the performance of the LMS controller.

3.5 Feedback control with reduced sensing area

The above feedback control strategy uses a sensor signal which depends upon the pressure integrated over the entire rear face (base) of the building, as shown in figure 3.16(b).

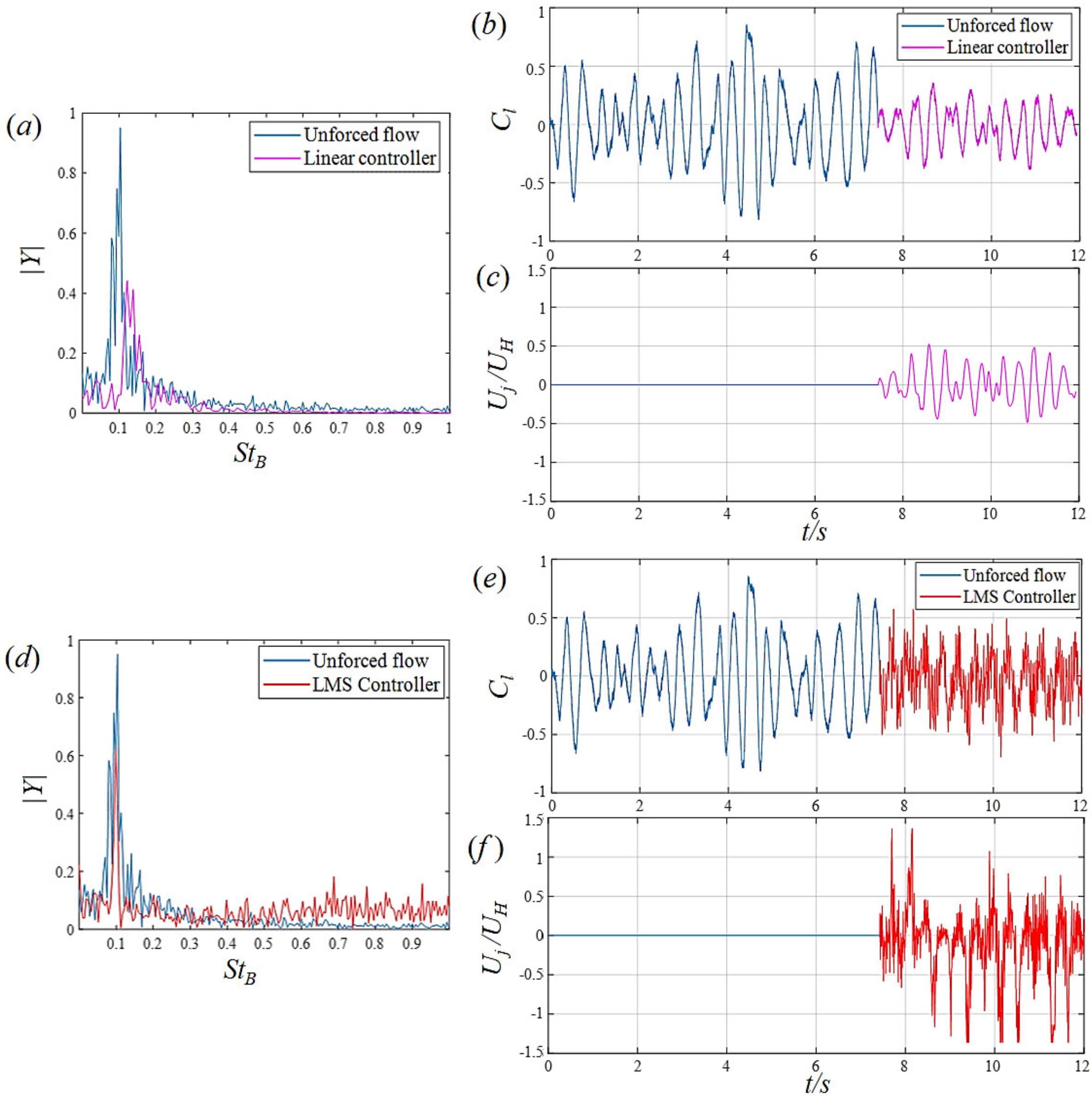

Figure 3.20: Effect of control: (a) spectra for antisymmetric base pressure force signal with linear feedback control; (b) time variation of building side-force (lift) coefficient with linear feedback control; (c) corresponding actuation signal with linear feedback control; (d) spectra for antisymmetric base pressure force signal with LMS feedback control; (e) time variation of building side-force (lift) coefficient with LMS feedback control; (f) corresponding actuation signal with LMS feedback control;.

In order to reduce the complexity of sensing and total number of individual sensors required, a controller is now investigated which is based upon sensing over a smaller building rear-face area.

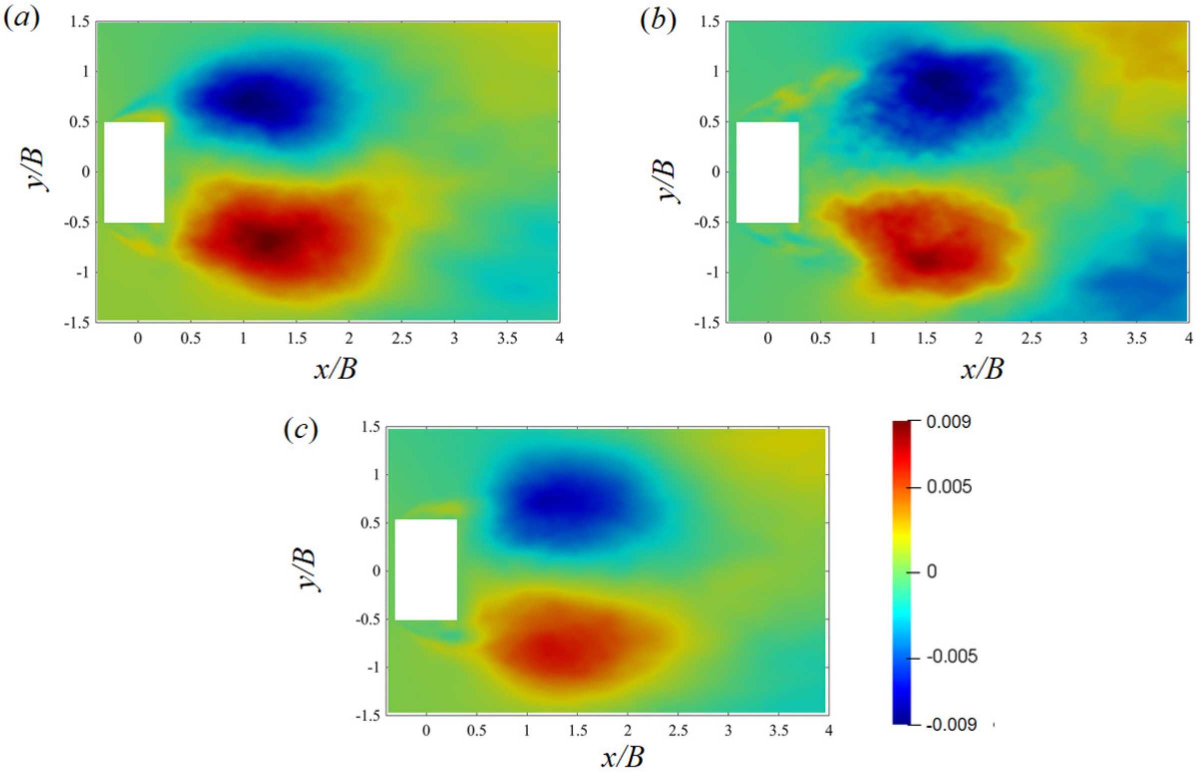

Figure 3.21: Streamwise velocity components of the first POD mode at $z = 0.5H$ for (a) unforced flow; (b) flow with the linear controller; (c) flow with the LMS controller.

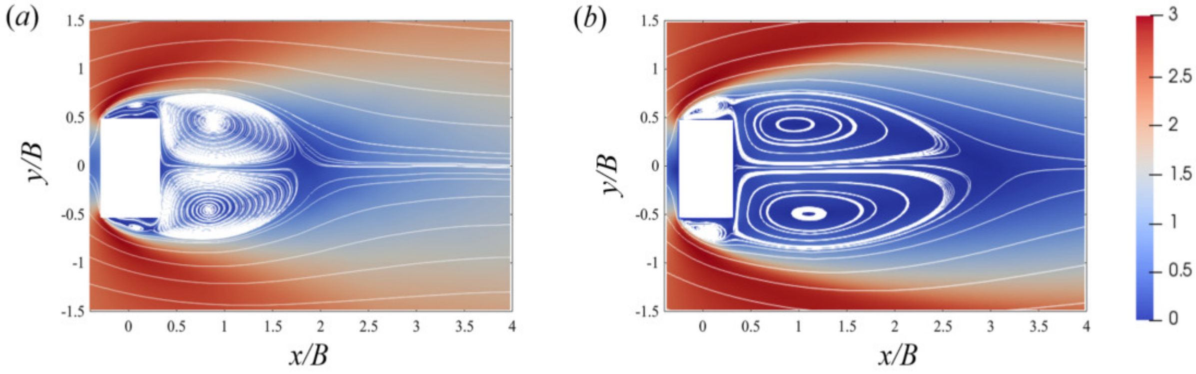

Figure 3.22: Colour contours of the time-averaged streamwise velocity and line contours of stream function. (a) Unforced flow; (b) Linear controlled flow.

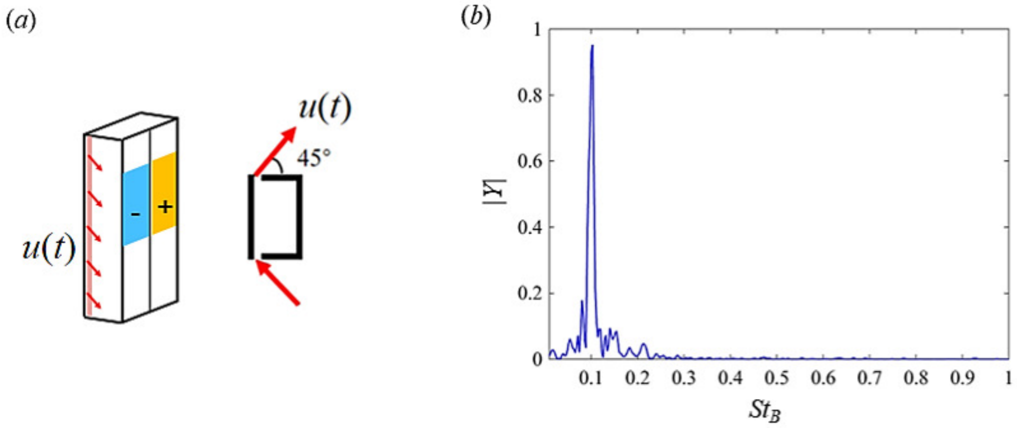

Figure 3.23: (a) Setup of the body-mounted sensors and actuation for the new feedback strategy. (b) Spectrum of the partial antisymmetric pressure signal for unforced flow

As the dynamic response of a high-rise building to unsteady loading can be approximated by that of a cantilever beam, pinned at its lower end to the ground, the effect of unsteady loading towards the top of the building will have more effect on motion amplitude and hence occupant comfort. At the same time, the antisymmetric vortex shedding mode that dominates the unsteady loading is predominant towards the middle of the building, as shown in figure 3.11, with downwash and upwash flows becoming more influential towards the top and the bottom respectively. For these reasons, a sensing area which extends over the upper part of the building base, but not as far as the top, i.e. from $0.4H$ to $0.8H$, is investigated, as shown in figure 3.23(a). The sensing again takes the asymmetric component of this pressure force over this reduced area. The unforced spectrum of this new sensor signal is shown in figure 3.23(b), exhibiting a similar frequency peak to that of full base sensing in figure 3.16(b).

Having a better performance than the LMS controller, the linear feedback control strategy described in Section 3.4.3 is chosen to check the feasibility of this reduced sensing area, and the actuation is implemented as shown in figure 3.17. The modified open loop frequency response, identified through harmonic forcing simulations, is shown in figure 3.23(a). It exhibits little dependence on the input forcing amplitude, implying dynamic linearity. The fifth order linear state-space model, $G_n(s)$, resulting from a fit through these points using Matlab's `fitfrd` function, is also shown in figure 3.24(a), exhibiting a similar form to that with full base area sensing. The feedback controller, $K_n(s)$, was designed by loop-shaping in the frequency domain to give low sensitivity close to frequencies of $St_B = 0.1$; its phase and gain along with the resulting sensitivity function are shown in figure 3.24(b), where it can be seen that $|S(s)| < 1$ is achieved close to $St_B = 0.1$.

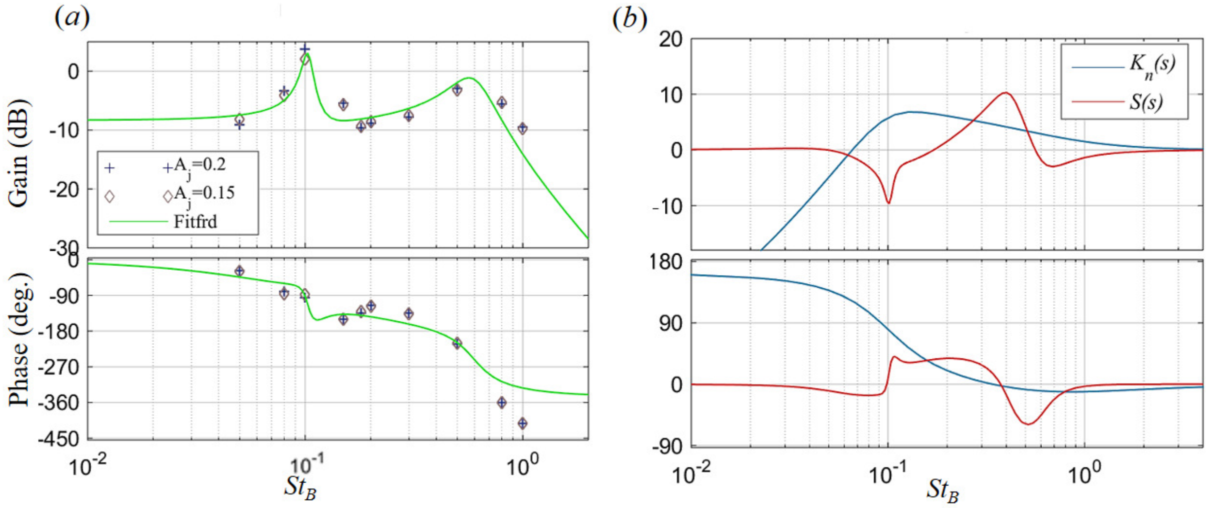

Figure 3.24: Frequency response: gains and phase shifts for (a) system identification data for open-loop forcing with less sensors (b) designed controller $K_n(s)$ and sensitivity function $S_n(s)$.

This feedback controller, based upon reduced sensing area, was implemented in simulations. The sensor (partial antisymmetric base pressure force) signals are compared both in the absence and presence of feedback control in figure 3.25, along with the building's side-force (lift) coefficients. Control is seen to achieve its primary objective of attenuating the sensor signal fluctuations, giving corresponding attenuation in the fluctuations of C_l, approximately 35%, demonstrating that feedback control with reduced sensing area is feasible.

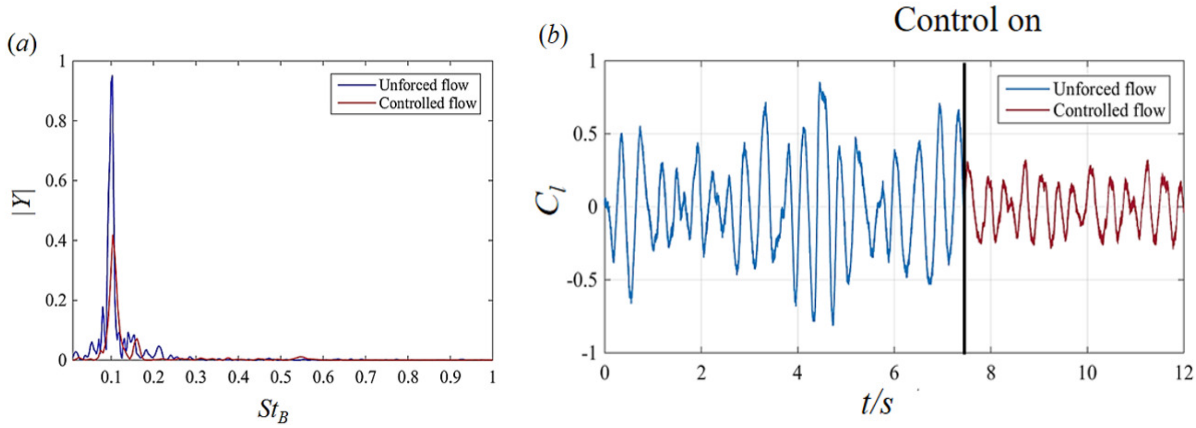

Figure 3.25: Effect of the controller with less sensors: comparison between cases with and without feedback control in (a) spectrum for antisymmetric base pressure signal; (b) time history for lift coefficient.

3.6 Summary

In this chapter, the flow structures around a high-rise building immersed in an atmospheric boundary layer were studied numerically using wall-resolved large eddy simulations. A canonical high-rise building, known as the CAARC model, was studied, which has a constant rectangular cross-section. An oncoming wind normal to the wider dimension was considered.

The flow features were found to be three-dimensional, with two types of spanwise vortex shedding evident, along with a downwash flow over the building top and an upwash flow near the building/ground interface. The flow intermittently changes between antisymmetric vortex shedding, which exhibits a dominant frequency, and symmetric vortex shedding, which is not associated with a dominant frequency. The switching from the antisymmetric to the symmetrical vortex shedding mode gradually transmits from the top of the building towards the near ground, and the region near the top maintains the symmetric vortex shedding longer. Proper orthogonal decomposition confirmed that the large-scale Von Karman antisymmetric vortex shedding mode is prevalent in the near wake, rather than the symmetric mode. This mode dominates the unsteady loading on the building. The influence of the atmospheric boundary layer was also analyzed via the comparison with the uniform inflow case, with it being found that the symmetric vortex shedding mode gets suppressed significantly when the building is fully immersed in the atmospheric boundary layer.

Two feedback control strategies were then developed, which aimed to attenuate the building's unsteady loading. The control strategies were implemented via body-mounted sensors and actuation, for practical applicability. Sensing was chosen to be the vertically antisymmetric component of the base pressure force on the building's rear face, this allowing the most important features of the unsteady loading to be captured through measurements on only one building face. Actuation was via zero-net mass flux (unsteady slot jet) actuation along the two leading edges of the building, constant along each edge and with actuation along each edge in anti-phase with the other.

System identification of the sensor signal unsteady response to actuation was performed, using harmonic forcing of the actuator signal across relevant frequencies and amplitudes. A linear feedback controller base on the frequency-domain loop-shaping method and a LMS adaptive controller were then designed to attenuate the sensor unsteadiness in the presence of feedback control. The designed controllers were implemented in large eddy simulations, and successfully attenuated the building's side force fluctuations by 38% and 17% respectively. A further study showed that reducing the sensing to 40% of the building's rear face area led to similar successful linear feedback control.

Chapter 4

Attenuation of unsteady loading using top-surface open-loop control

4.1 Introduction

In this chapter, we investigate numerically the use of active open-loop control strategies to attenuate the unsteady loading of a canonical high-rise building at different oncoming wind angles. Building on the knowledge discussed in Section 1.2.1 that, for a square FWMC, a perturbation near the free end can affect the aerodynamic forces, active control in the form of a synthetic jet positioned on the top surface is employed. The ability of a synthetic jet to control bluff-body flows has been extensively studied in other contexts (Qu *et al.*, 2017, 2019; Zhu & Morrison, 2021; Erfan *et al.*, 2021; Dahan *et al.*, 2012). The present study investigates whether this synthetic jet, set on the top surface of the building, can act on the downwash flow and attenuate the unsteady loading of a high-rise building. Exploiting the simplicity of this approach as compared to feedback control, we further investigate whether this can be achieved across a wide range of oncoming wind directions. We believe this represents the first attempt to employ a synthetic jet on the top surface with the aim of controlling the flow around a high-rise building across different oncoming wind angles. The study is performed numerically, using high-fidelity wall-resolved large eddy simulations (WRLES). The unforced and controlled flows are analysed across the different wind angles, offering insights into the control mechanisms of the actuation.

This chapter presents the simulation set-up in section 4.2 followed by the implementation of the active control and an investigation of flow structures for the unforced and controlled cases in section 4.3. It finishes with concluding remarks.

4.2 Simulations set-up and validation

The same wall-resolved large eddy simulation approach and CAARC building model as in Chapters 2 and 3 are employed. The same Reynolds number is considered, but in the present chapter, the oncoming wind angle is not only assumed to be normal to the wide side of the building. A range of oncoming wind angles is investigated, as shown in figure 4.1.

Obasaju experimentally measured the unsteady loading of the CAARC across the different oncoming wind angles with the turbulent inflow and it can be observed that most of the unsteady loading variation is captured in the 0° to 45° range (Obasaju, 1992). Thus four different oncoming wind angles with respect to the shorter cross-sectional side of the building (see figure 4.1(a)), $\alpha = 0^\circ$, 10°, 20° and 45°, were investigated numerically. When at $\alpha = 0^\circ$, the flow set-up of simulation matched the unforced case in Chapter 3.

Figure 4.1(b) shows the sketch of the computational domain used. The origin of the solution domain is defined on the junction of the CAARC building model and the ground,

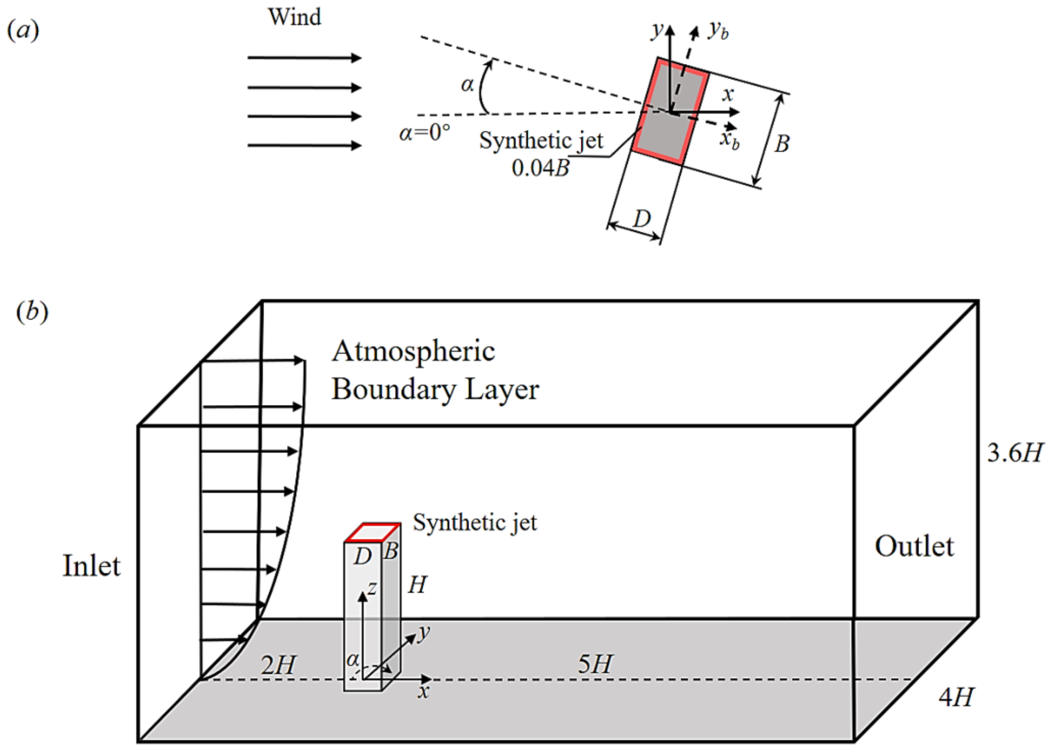

Figure 4.1: (a) Top surface of the high-rise building ; (b) Flow set-up, showing the CAARC building model, ground, the atmospheric boundary layer and the computational domain. The red rectangle denotes the location of the synthetic jet open-loop forcing, which is in the upward (z) direction.

centred on the building axis. The free stream flows in the $+x$ direction; the horizontal direction normal to the flow and the vertical (building spanwise) direction are designated by the y-axis and z-axis, respectively. The setup of the computational domain and the generation of inlet boundary condition that can realistically mimic the atmospheric boundary layer follow as for Chapter 3. The generated inflow shows a good performance in reproducing the prescribed turbulence characteristics and was well tested and validated in Chapter 3.

Flow forcing is provided by a zero-net-mass-flux (ZNMF) synthetic jet. The modelling of the actuation is kept simplistic and the jet cavity is not resolved. The slot on the top surface of the building model is designed as the synthetic jet exit, and it is positioned around the perimeter of the top surface with a width of $0.04B$, as shown in figure 4.1. Unlike in Chapter 3, where the actuation synthetic jet signal was prescribed according to the feedback control algorithm, the present chapter employs open-loop control. A harmonic actuation signal is chosen, and the boundary condition of the actuation is described by a periodic velocity profile. The components of the instantaneous velocity vector at the actuation slot exit are

$$u_{jet} = v_{jet} = 0, \tag{4.1}$$

$$w_{jet} = U_f \sin(2\pi f_f t), \tag{4.2}$$

where u,v and w are respectively the velocity components along the x, y and z directions, and U_f is the maximum jet velocity. The forcing amplitude ratio A^*, defined as U_f/U_H, is chosen as 1 following the optimal suction ratio suggested by Wang *et al.* (2018). The only variable parameter of the actuation was the forcing frequency. As shown in Chapter 3, the spanwise vortex shedding frequency for the unforced case at $\alpha = 0°$ is $St_0 = 0.1$, where $St = fB/U$ is the Strouhal number based on the building width, B. The forcing frequency, St_f is typically non-dimensionalized by the vortex shedding frequency of the unforced flow, St_0. Motivated by the successful application of high-frequency open-loop forcing to bluff-body flows in other contexts (Zhu & Morrison, 2021; Oxlade *et al.*, 2015), where effective open-loop control occurred at forcing frequencies approximately an order of magnitude larger than the vortex shedding frequency, dimensionless forcing frequencies spanning three different values of $St_f/St_0 = 5$, 10, and 15 were considered.

The spatial discretization of the computational domains is performed with an unstructured grid composed of trimmer cells and prism layer cells using StarCCM+. The unstructured grid created and validated in Chapter 3 was employed for the case at $\alpha = 0°$. For other wind directions, new grids had to be generated, and the case at α=20° is shown

Case	Mesh size	$\overline{C_{Fxb}}$	$C_{\sigma_{Fxb}}$	$\overline{C_{Fyb}}$	$C_{\sigma_{Fyb}}$
Coarse	8.4 Million	1.19	0.17	-0.041	0.13
Baseline	18.2 Million	1.16	0.23	-0.037	0.198
Fine	23.8 Million	1.16	0.22	-0.037	0.205
Experimental	N/A	1.17	0.24	-0.038	0.2

Table 4.1: Summary of the grid refinement study for the $\alpha = 20°$ wind angle case. The mean (overbar) and r.m.s. (subscript σ) values of the aerodynamic force coefficients C_{Fxb} and C_{Fyb} are compared to experimental values from Obasaju (1992).

as an illustrative example for an inclined building model. Figure 4.2 shows the grid in the symmetry plane at $y = 0$ and the xy plane at $z = 0.5H$. The mesh close to the ground and the building is refined to fully resolve the boundary layer using prism layers. The baseline mesh for the case at α=20° was identified via a grid refinement study. Following experimental measurements (Obasaju, 1992; Melbourne, 1980), the aerodynamic forces along axes fixed on the building body across different wind angles were considered for the study. Defining F_{xb} and F_{yb} as the aerodynamic pressure forces normal to the rear face and side face of the building model (x_b-direction and y_b-direction in figure 4.1(a)) respectively, the corresponding non-dimensional aerodynamic force coefficients follow as

$$C_{Fxb} = \frac{F_{xb}}{0.5\rho U_H^2 BH}, \qquad C_{Fyb} = \frac{F_{yb}}{0.5\rho U_H^2 BH}, \tag{4.3}$$

where U_H is the mean flow velocity at the top of the building. Results from three different grid refinements were compared to the experimental measurement from Obasaju (1992), and are summarized in table 4.1. As compared to the fine mesh, the baseline grid adopts an identical size for the first cell from the building walls, with the wake region relatively less refined. While the coarse mesh under-predicts the fluctuating parts of aerodynamic forces, the differences in values between the baseline and fine mesh suggest that the baseline mesh of 18.2 million cells is sufficiently fine to accurately simulate the flow.

For the baseline mesh for the 20° wind angle, the spatial distribution of y^+ around the

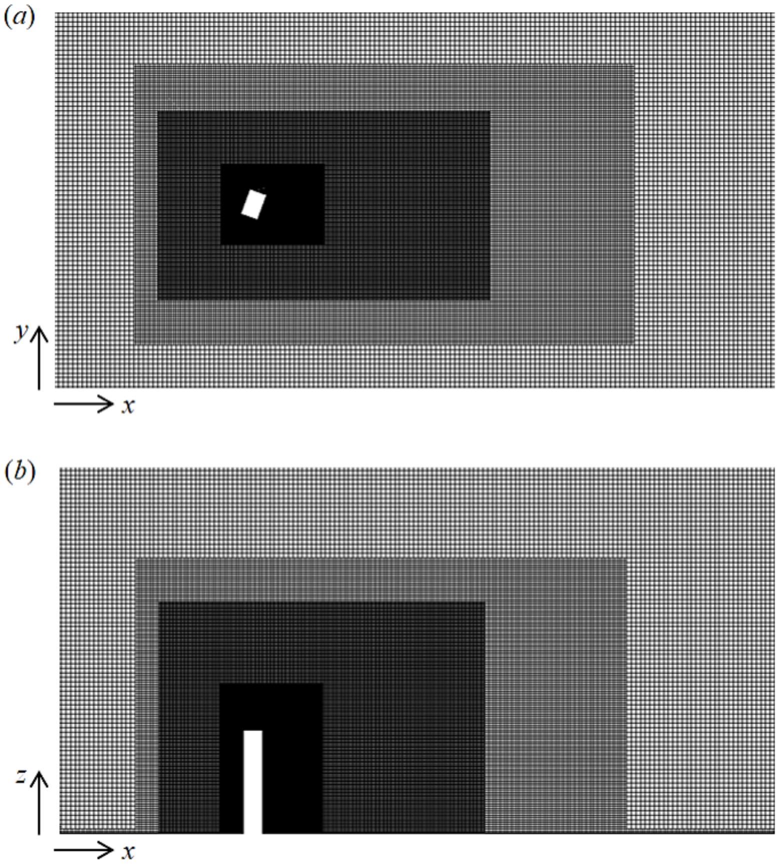

Figure 4.2: Baseline grid used for an oncoming wind angle of $\alpha = 20°$.(a) xy slice, top view. (b) xz slice, side view.

building is shown in figure 4.3, where it can be observed $y^+ \simeq 1$. The Courant–Friedrichs–Lewy number in the simulation is dynamic and remains below 0.2. Unsteady simulations were performed on the Imperial College cluster and the ARCHER2 UK computational facility using several hundred cores.

4.3 Implementation of open-loop control

The open-loop active control strategy in the form of a synthetic jet located on the top surface is implemented in the simulations across different oncoming wind angles. After

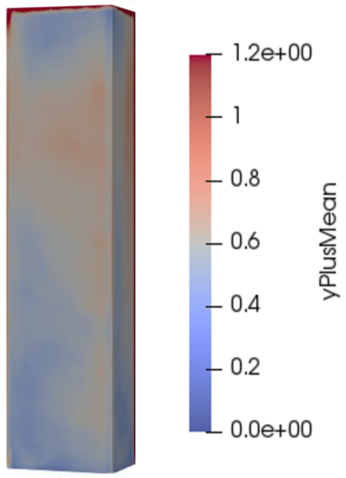

Figure 4.3: y^+ colormap on the surface of the building for the baseline mesh at $\alpha = 20°$.

removing the transient stage, the statistics of 32 cycles of the spanwise antisymmetric vortex shedding are sampled for the analysis of the unforced and controlled flows. The aerodynamic characteristics are examined first, after which the time-averaged flow features are investigated. This is followed by the analysis of the effect of the synthetic jet on the unsteady flow features.

4.3.1 Aerodynamic characteristics

Figure 4.4 presents the fluctuating aerodynamic force coefficients of a CAARC building, the r.m.s. values of C_{Fyb} and C_{Fxb}, under the influence of open-loop control at different oncoming wind angles, where the unforced case serves as a benchmark for comparison.

For the unforced case, the fluctuation of the side force, C_{Fyb}, exhibits a maximum value of 0.29 at $\alpha = 0°$, this value reducing as the oncoming wind angle increases from 0° to 45°. The r.m.s. values of C_{Fyb} are respectively 0.26, 0.20 and 0.11 at $\alpha = 10°$, 20° and 45°, matching the experimental measurements from Obasaju (1992) well, and further confirming the reliability of the simulations.

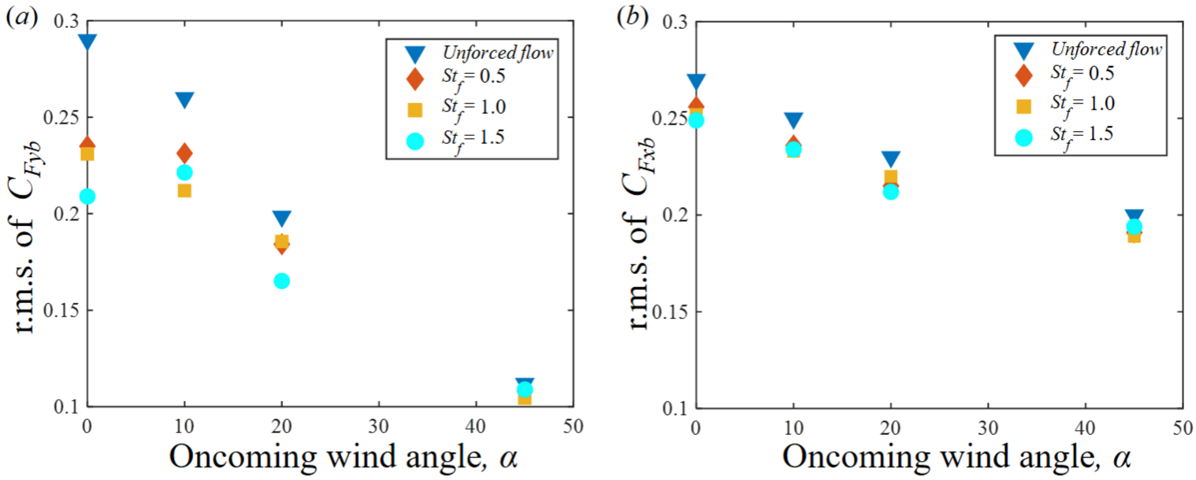

Figure 4.4: Effect of open-loop control on the fluctuating aerodynamic force coefficients for different oncoming wind angles: (a) the r.m.s. value of C_{Fyb}; (b) the r.m.s. value of C_{Fxb};

In the presence of the top-surface active control, figure 4.4(a) shows that its effect is to significantly attenuate the fluctuation of C_{Fyb} for oncoming wind angles of $\alpha = 0°$, $10°$ and $20°$. The attenuation remains present but smaller for $\alpha = 45°$, although the fluctuations are so much smaller in absence of control at this wind angle. For the wind angles of α=0° and 20°, the most effective forcing frequency is St_f=1.5, for which the r.m.s. values of C_{Fyb} are reduced respectively by approximately 25% and 15% compared with the unforced cases. Effective attenuation is also achieved for forcing frequencies of $St_f = 0.5$ and 1. At $\alpha = 10°$, while the minimum value of the side-force fluctuation occurs for $St_f = 1$, control remains almost as effective at the higher forcing frequency of $St_f = 1.5$, which decreases the r.m.s. value of C_{Fyb} by 15%.

The fluctuations of C_{Fxb} across different forcing frequencies are shown in figure 4.4(b). For the unforced flow, the r.m.s. value of C_{Fxb} falls off with increasing wind angle, although this is less pronounced than the falloff of C_{Fyb}. The effect of open-loop forcing is to reduce these fluctuations for all three forcing frequencies and across all wind angles, although the effect is less pronounced than for C_{Fyb}. This is consistent with the fluctuating C_{Fxb} depending more on the inflow turbulence rather than the near wake dynamics (Obasaju, 1992; Hu & Morgans, 2022). The time-averaged values of C_{Fyb} and C_{Fxb} have also been checked and found to be mildly reduced by the impact of the synthetic jet.

4.3.2 Time-averaged flow characteristics

The effect of open-loop control on the time-averaged near wake structures is now investigated. Open-loop forcing at a frequency of $St_f = 1.5$ overall gave the most significant building unsteady loading reductions, with these being most relevant for the smaller wind angles of $\alpha = 0°$, $10°$ and $20°$. The effect of the synthetic jet at $St_f = 1.5$ and across these smaller wind angles is now considered in more detail.

Figures 4.5(a) and (c) show the time-averaged streamlines and streamwise velocity field in the horizontal slice at $z = 0.5H$ at $\alpha = 0°$ for the unforced and controlled cases respectively. For the unforced case, the oncoming flow separates at the leading edges of the building, forming bubbles on the side faces of the building. A large low-pressure recirculation region, which is approximately symmetrical about the wake centerline of $y = 0$, is established behind the building. For open-loop forcing at $St_f = 1.5$, the size of the recirculation region is extended in the streamwise direction. This is consistent with the attenuation of the spanwise vortex shedding achieved by the synthetic jet, which will be shown later in Sec 4.3.3.

The time-averaged streamwise velocity field on the xz plane at $y = 0$ for the unforced case is shown in figure 4.5(b). The main flow separates at the leading edge of the top surface, and the downwash free-end shear layer meets with the upwash flow originating from the ground, forming a saddle point at $z = 2.7B$. For forcing at $St_f = 1.5$, it can be observed that the separated shear layer is closer to the top surface, and the streamlines in the vicinity of the trailing edge slot are slightly affected by the motion of the synthetic

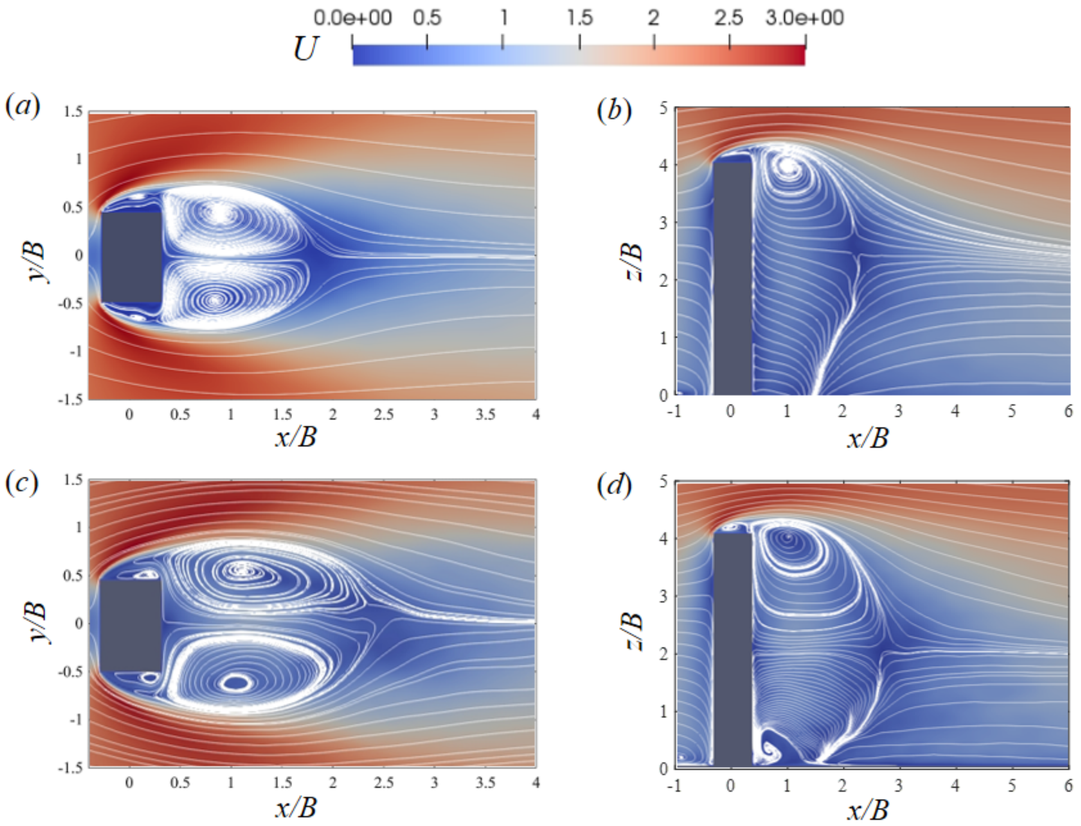

Figure 4.5: Time-averaged streamwise velocity field and projected streamlines for an oncoming wind angle of $\alpha = 0°$. The unforced case: (a) Top view in the horizontal plane $z = 0.5H$, (b) side view in the symmetry plane $y = 0$. The controlled case of $St_f = 1.5$: (c) Top view in the horizontal plane $z = 0.5H$, (d) side view in the symmetry plane $y = 0$.

jet. The size of the flow reversal zone in the near wake enlarges, which corresponds to the increase in the recirculation region in the xy plane. Moreover, the saddle point is located at $z = 2.1B$, much lower than the unforced case, illustrating the enhancement of the downwash flow. Figure 4.6 shows the time-averaged vertical velocity field on the xz plane at $y = 0$ for the unforced and controlled cases. The region with the negative w value is noticeably expanded towards the ground in the vertical direction, consistent with the movement of the saddle point in figure 4.5 and indicating the downwash flow is strengthened under the impact of the synthetic jet. The enhanced downwash flow also causes downward (rather than upward) flow near the lower part of the back face of the

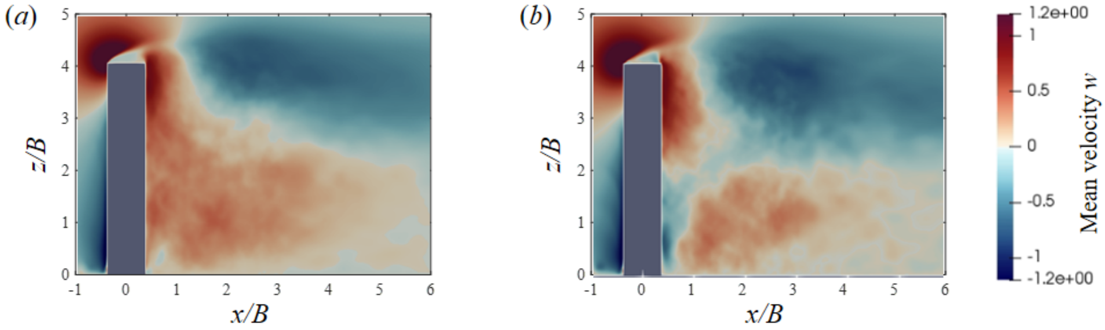

Figure 4.6: Time-averaged vertical velocity distribution on the xz plane at $y = 0$ for an oncoming wind angle of $\alpha = 0°$. (a) The unforced case, (b) the controlled case of $St_f = 1.5$.

building, which is associated with the formation of the small weak vortex structure near the junction of the building with the ground shown in figure 4.5(b).

Figure 4.7 shows the distribution of turbulent kinetic energy (TKE) of the free-end shear flow on the xz plane, offering insights into the strength of momentum transport in the flow near the top surface (Wang *et al.*, 2018). For the unforced case, the relatively high-value region of TKE associated with the shear layer flow is mainly located above the top surface, and the peak value occurs at $z = 1.08H$ near the trailing edge of the top surface. For the controlled case, the TKE exhibits a triple-peak distribution, where two peaks are located near the slot exit of the synthetic jet, and the other, associated with the separated flow, occurs further upstream and closer to the top surface compared with the unforced case. The maximum TKE occurring near the slot exit is significantly higher than for the unforced case, and the region with a relatively high TKE value shows a wider vertical spread above the top surface of the building. The synthetic jet strengthens the turbulent fluctuation near the top surface of the building, and Wang *et al.* (2018) and Wang *et al.* (2022) suggested that this strong turbulent fluctuation can enhance the momentum transport between the high-momentum main flow and the wake, thus further inducing the stronger downwash flow.

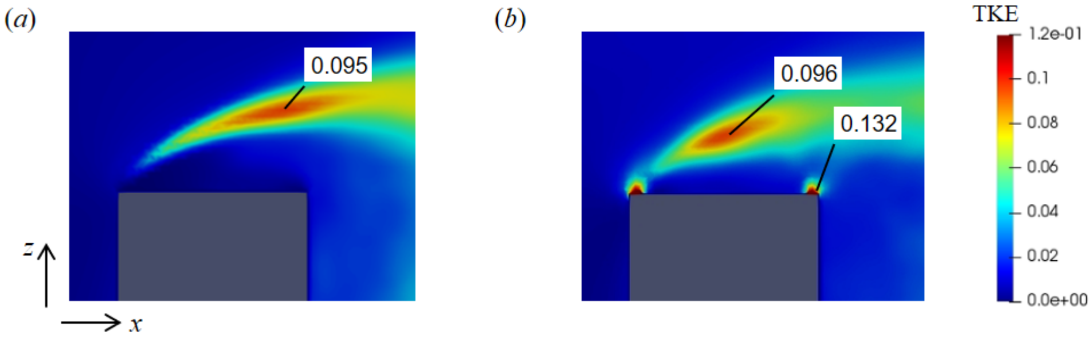

Figure 4.7: TKE distribution near the top surface at $y = 0$ for an oncoming wind angle of $\alpha = 0°$. (a) The unforced case, (b) the controlled case of $St_f = 1.5$. Local maxima in the TKE are marked as values in the plots.

The time-averaged Reynolds stresses on the horizontal slice at $z = 0.5H$ for the unforced case and the controlled case of $St_f = 1.5$ are compared in figure 4.8. For the unforced case, the time-averaged streamwise Reynolds normal stress $u'u'/U_\infty^2$ presents a double-peak pattern, which is symmetric about the centerline. The peaks are located in the separated shear layers around the building with a maximum of 0.33. A similar distribution pattern is observed for open-loop forcing at $St_f = 1.5$, but with the maximum of $u'u'/U_\infty^2$ being significantly reduced to 0.24. The $u'u'/U_\infty^2$ values in the separated shear layer region are also reduced compared to the unforced case.

The distribution of $v'v'/U_\infty^2$ for the unforced case is shown in figure 4.8(b). Since the antisymmetric vortices from two side edge shear layers oscillate periodically in the y-direction, a single-peak distribution of $v'v'/U_\infty^2$ is observed with a maximum of 0.23 occurring along the centreline, with streamwise location $x/B = 1.59$. In the presence of the synthetic jet at $St_f = 1.5$, the peak of $v'v'/U_\infty^2$, corresponding to the spanwise vortex, is pushed much further downstream to near $x/B = 2.09$, with its value reduced by 15.3%. This indicates that the synthetic jet successfully pushes the spanwise vortex shedding further downstream and weakens it in the process, which is ascribed to the enhancement of the downwash flow.

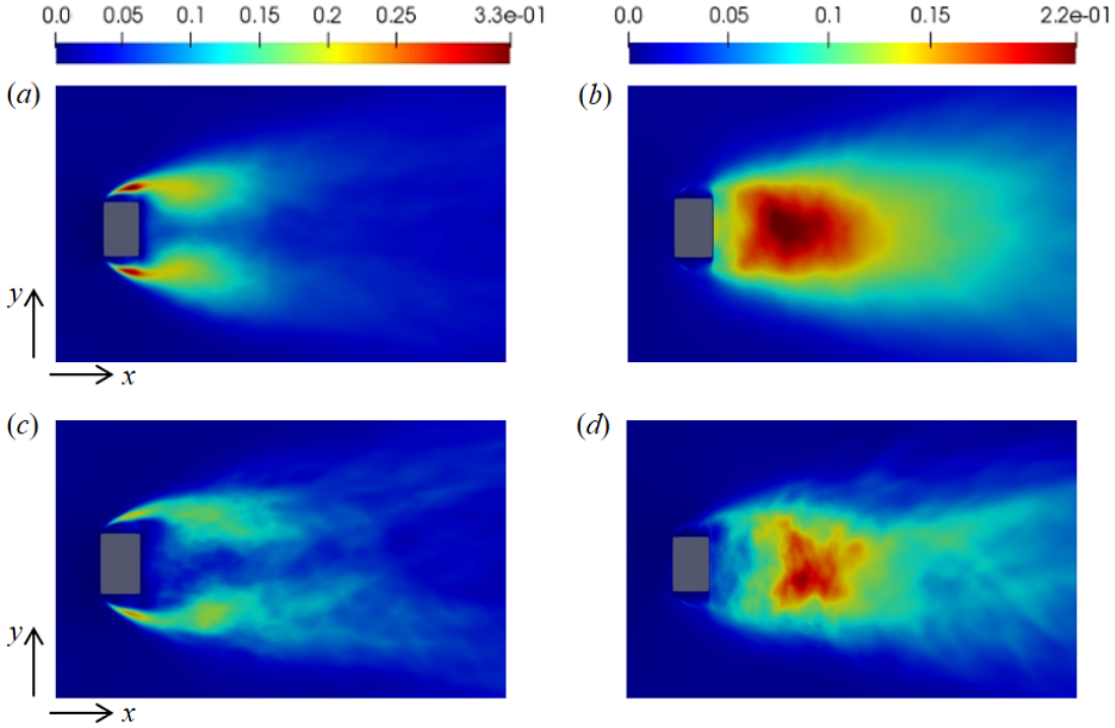

Figure 4.8: Time-averaged Reynolds stress distributions in the horizontal slice at $z = 0.5H$ for an oncoming wind angle of $\alpha = 0°$: $u'u'/U_\infty^2$ and $v'v'/U_\infty^2$ for (a, b) the unforced case;(c, d) the controlled case of $St_f = 1.5$.

Figure 4.9 shows the effect of open-loop control on the time-averaged streamlines and velocity field in the horizontal slice for an oncoming wind angle of $\alpha = 10°$. For the unforced case, the main flow also separates at the leading edges, and no reattachment occurs on the side faces. However, the mean wake structures behind the building are not symmetric about the centerline; the vortex structure near the lower side is larger than that close to the upper side. The controlled flow also shows asymmetry in the mean wake topology, but with the recirculation region extending further downstream similar to the effect at $\alpha = 0°$.

The effect of control at an oncoming wind angle of $\alpha = 20°$ is shown in figure 4.10. The reattachment of the separated shear layer can be observed on the lower side faces of the building for the unforced case, different to the flows at $\alpha = 0°$ and 10°. A second flow

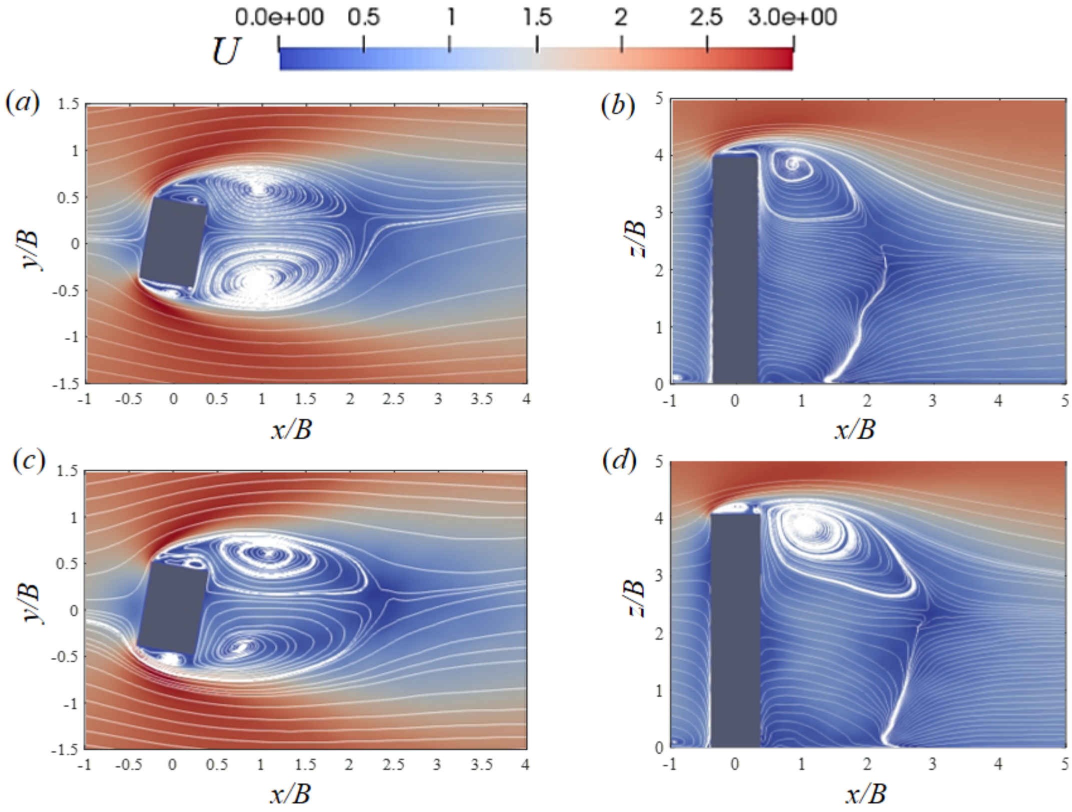

Figure 4.9: Time-averaged streamwise velocity field and projected streamlines for an oncoming wind angle of $\alpha = 10°$. The unforced case: (a) Top view in the horizontal plane $z = 0.5H$, (b) side view in the symmetry plane $y = 0$. The controlled case of $St_f = 1.5$: (c) Top view in the horizontal plane $z = 0.5H$, (d) side view in the symmetry plane $y = 0$.

separation occurs at the trailing edge of the lower side, forming the recirculation region behind the building. The open-loop control has little impact on the reattachment but still extends the size recirculation region in the streamwise direction.

The time-averaged velocity fields on the xz plane at $\alpha = 10°$ and $20°$ are also shown in figures 4.9 and 4.10 respectively. The flow patterns of the unforced flow at these two angles do not change much compared with the case at $\alpha = 0°$. At $\alpha = 10°$ and $20°$, the control extends the flow reversal zone and enhances the downwash flow, similar to its effect at $\alpha = 0°$.

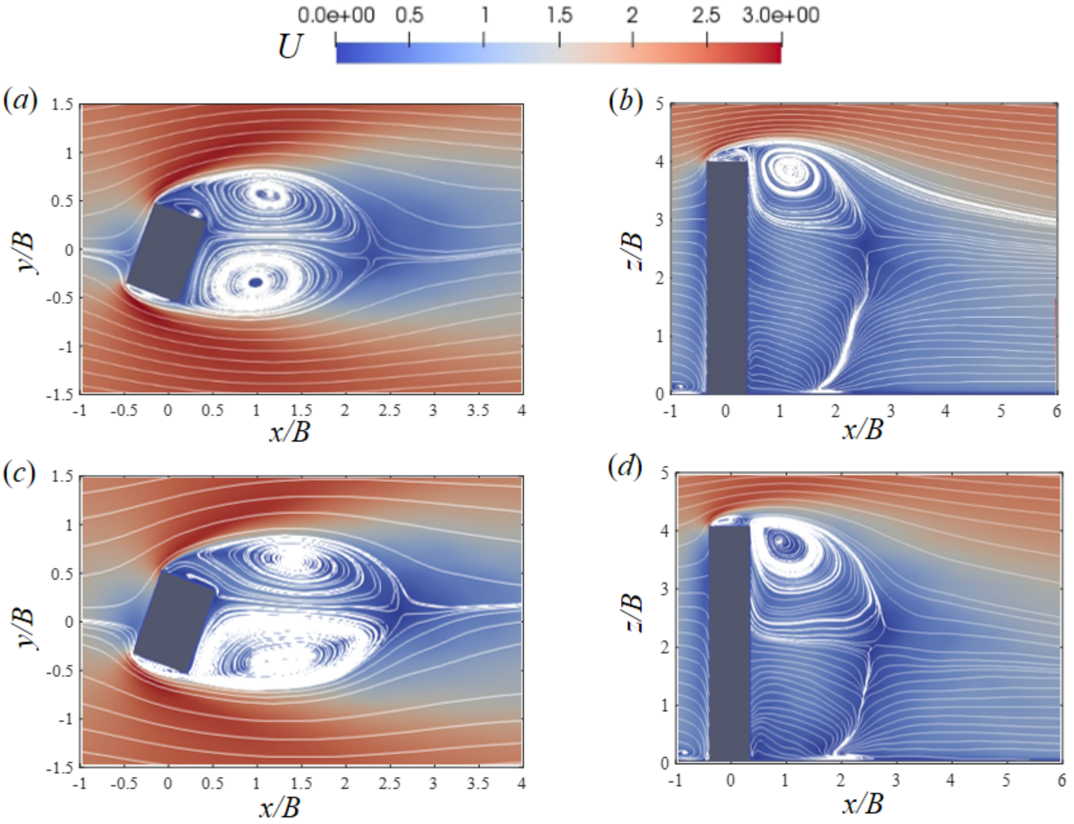

Figure 4.10: Time-averaged streamwise velocity field and projected streamlines for an oncoming wind angle of $\alpha = 20°$. The unforced case: (a) Top view in the horizontal plane $z = 0.5H$, (b) side view in the symmetry plane $y = 0$. The controlled case of $St_f = 1.5$: (c) Top view in the horizontal plane $z = 0.5H$, (d) side view in the symmetry plane $y = 0$.

4.3.3 Unsteady flow characteristics

In order to better understand the mechanism by which the actuation attenuates the unsteady loading, the unsteadiness in the flow around the building under the effect of the open-loop control is further investigated. The frequency spectra of the fluctuating side force for the unforced and controlled cases are examined first, after which the flow structures caused by the synthetic jet are investigated.

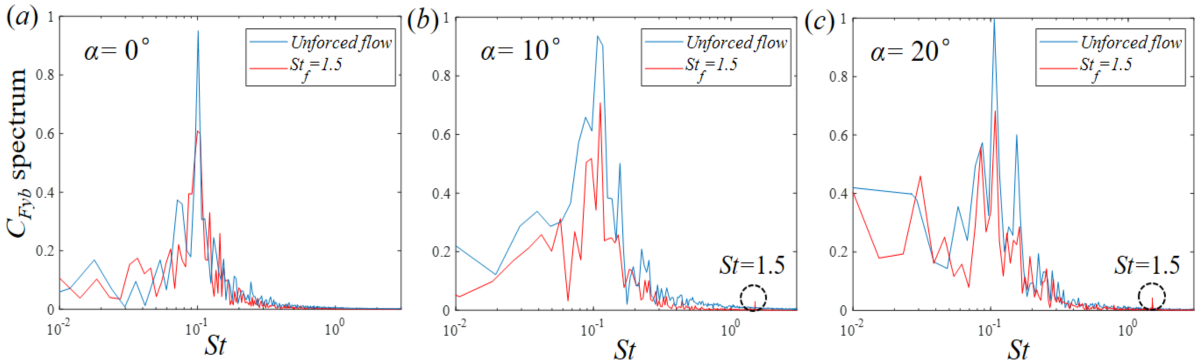

Figure 4.11: Normalized spectra of the building's side-force fluctuation, C_{Fyb} at (a) $\alpha = 0°$; (b) $\alpha = 10°$; (c) $\alpha = 20°$.

Frequency analysis

The spectra of the side-force fluctuation are compared for the unforced and controlled cases for three oncoming wind angles in figure 4.11. For the unforced case, the main spectrum peak in the side-force fluctuation, corresponding to antisymmetric vortex shedding (Hu & Morgans, 2022), occurs at the same frequency $St = 0.1$ for cases of $\alpha = 0°$, $10°$ and $20°$. Defining St' as the Strouhal number taking the width of the building model normal to the flow as the reference length, these peak frequencies are respectively $St' = 0.1$, 0.11 and 0.118, showing good agreement with the dominant frequencies reported in the experimental study of Obasaju (1992). In the presence of control at $St_f = 1.5$, the fluctuation of C_{Fyb} still exhibits a narrow peak associated with the spanwise vortex shedding at around $St = 0.1$ for all three wind angles, but these dominant peak values are significantly reduced compared with the unforced case. Thus the synthetic jet is effective in attenuating the side-force fluctuations.

The power spectral densities of C_{Fxb} are compared in figure 4.12. The spectra in the presence of control exhibit a peak at the forcing frequency, $St = 1.5$, indicating the direct influence of the synthetic jet on the separated shear layer flow near the top surface. Interestingly, for the spectra of the side-force fluctuations, C_{Fyb}, the peak corresponding

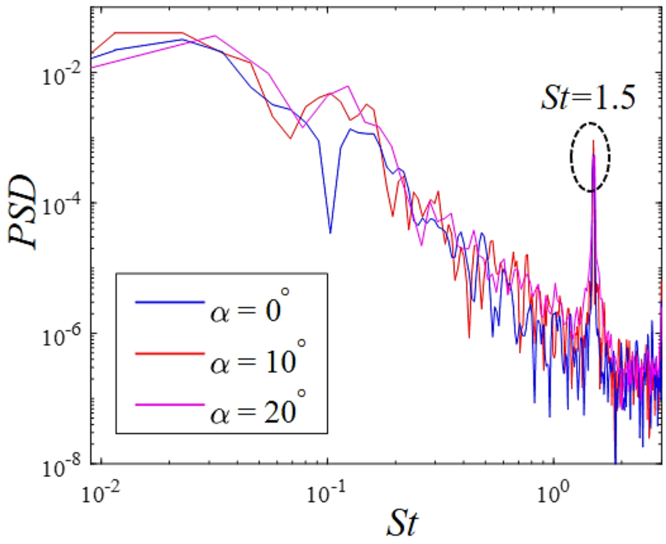

Figure 4.12: Power spectral density of C_{Fxb} of the building in the controlled cases across different oncoming wind angles, where filtering is applied using the pwelch function for clarity.

to the forcing frequency can be also observed at $\alpha = 10°$, $20°$, but not at $\alpha = 0°$, where C_{Fyb} does not include any component in the along-wind direction. This suggests that the synthetic jet does not directly affect the fluctuation of the force in the crosswind direction, which might lead to the absence of the peak at the forcing frequency for the controlled case at $\alpha = 0°$.

Jet behaviour

The synthetic jet on the top surface successfully attenuates the side-force fluctuation of a high-rise building, and thus it is of interest to analyse the unsteady flow structures generated by the synthetic jet. In this section, the immediate flow field in the vicinity of the synthetic jet is characterized for the control case of $St_f = 1.5$ at $\alpha = 0°$.

The velocity forcing direction of the synthetic jet positioned on the top surface is coincident with the z-axis, as shown in figure 4.1. The flow around the building under the effect of the synthetic jet is complex, highly turbulent, and comprises both large-scale structures and fine-scale turbulent fluctuations. Since our main interest is the former, modal decomposition was applied to the unsteady flow field. Spectral Proper Orthogonal Decomposition(SPOD) proposed by Towne *et al.* (2018), an empirical method to identify spatial-temporal coherent structures, was performed based on the time-resolved flow data. Compared with the space-only POD, SPOD is able to extract coherent structures oscillating at a certain frequency (Towne *et al.*, 2018; Schmidt *et al.*, 2018), which enables analysis of the dominant structures associated with the synthetic jet at its forcing frequency.

SPOD was performed based on the streamwise and vertical velocity fluctuations on the xz plane for the region close to the top surface, as shown in figures 4.13(b)-(d). 650 snapshots with a sampling time step of 0.01s were collected, and 9 blocks with 50% overlap were generated for the DFT analysis in the decomposition. The Hamming window function was applied to each block in order to avoid spectral leakage. The SPOD modal energy spectrum for the fluctuating kinetic energy of the plane at $y = 0$ is shown in figure 4.13(a), with a peak at the forcing frequency $St = 1.5$ present in Mode 1 which contains the most energy and thus plays a dominant role.

Figures 4.13(b) and 4.13(c) show respectively the streamwise and vertical velocity components of the first SPOD mode at $St = 1.5$. The strong oscillation in these two velocity components is observed above the top surface of the building, suggesting that coherent structures occur here. The first SPOD mode of the corresponding vorticity, ω_y, at the forcing frequency is further visualized in figure 4.13(d). Small vortex structures near the slot exits on the leading and trailing edges are observed. The height of these coherent structures increases gradually from the leading edge to the trailing edge, which can be ascribed to the separated shear flow near the top surface. The coherent vortex structures caused by the synthetic jet significantly enhance the turbulent fluctuations above

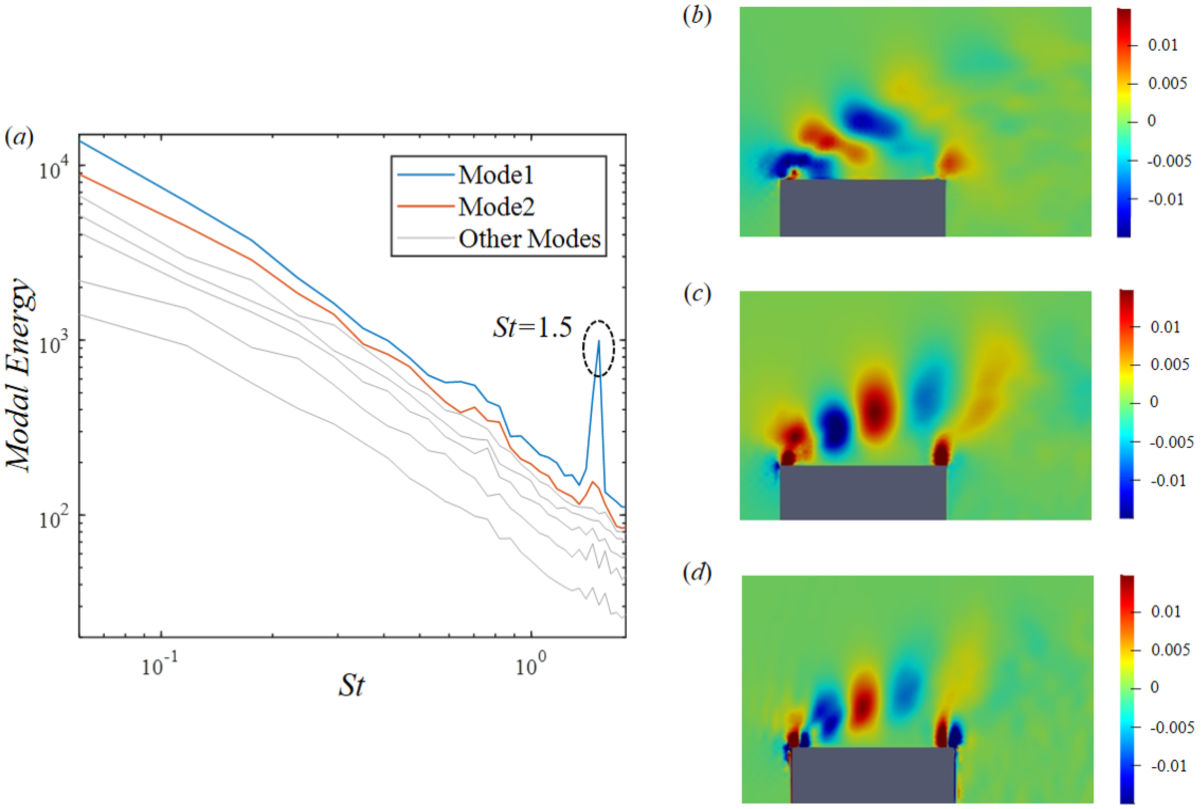

Figure 4.13: SPOD spectra and first SPOD mode on the xz plane at $y = 0$ for the controlled case at $\alpha = 0°$. (a) SPOD energy spectra; (b) streamwise velocity component of the first SPOD mode at $St = 1.5$; (c) vertical velocity component of the first SPOD mode at $St = 1.5$; (d) first SPOD mode of ω_y at $St = 1.5$.

the top surface as well as the momentum transport, consistent with the TKE results observed in figure 4.7. Wang *et al.* (2018) and Wang *et al.* (2022) suggested that this enhanced momentum transport can further induce a stronger downwash flow.

To understand further the effect of the synthetic jet, the fluctuation of the side-face pressure force was investigated for the controlled case. The normalized spectra of the side-force coefficient, C_{Fyb}, at different heights for the controlled case of $St_f = 1.5$ are shown in figure 4.14, where the peaks at the forcing frequency are not observed. However, since the slot of the synthetic jet is positioned around the top surface as shown in figure 4.1, the flow from the slot exits near the two side edges inevitably affect the pressure of the building's side faces. Figure 4.14 shows the spectra of the pressure

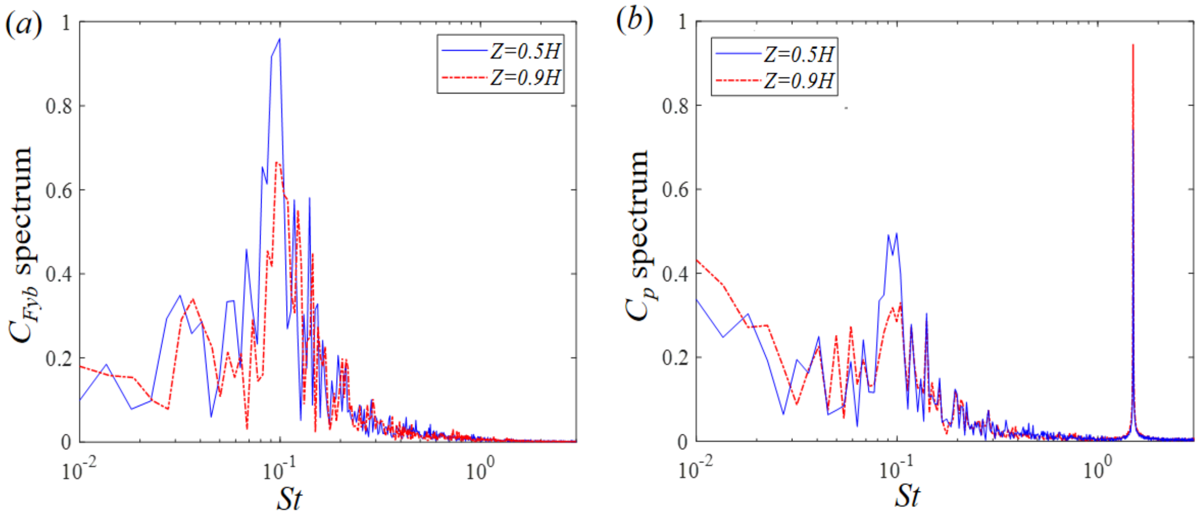

Figure 4.14: (a) Normalized spectra of C_{Fyb} at different heights of the CAARC building. (b) Normalized spectra of C_p at different heights.

coefficient only on one side face, C_p, for the controlled flow. It is observed that a narrow peak in C_p occurs near the forcing frequency, $St_f = 1.5$, indicating flow structures directly caused by the actuation exist near the two side faces. These flow structures are likely to be symmetric about the wake centerline, accounting for the observation that no spectral peak in C_{Fyb} occurs at the forcing frequency.

The streamwise and vertical velocity components of the first SPOD mode at the forcing frequency in the xy plane at $z = 0.9H$ are shown in figure 4.15, and are seen to exhibit symmetric coherent structures. Figure 4.15(c) shows the streamlines denoting the real-part mode shape of the vector composed of these two velocity components. The vortex structures formed near two sides of the building are completely symmetric about the wake centerline, illustrating the synthetic jet on the top surface has no direct impact on the net side-force fluctuation. The symmetric coherent structures are ascribed to the flow from the jet exit close to two side edges.

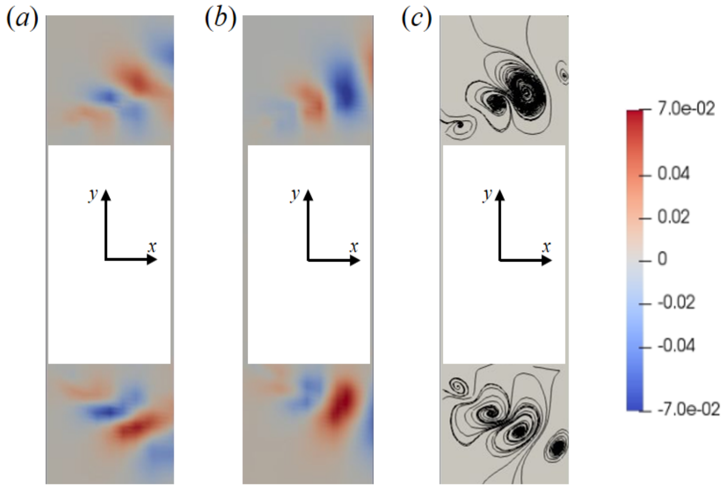

Figure 4.15: First SPOD mode around the building on the horizontal slice at $z = 0.9H$ for the controlled case at $\alpha = 0°$. (a) Streamwise velocity component of the first SPOD mode at $St = 1.5$; (b) vertical velocity component of the first SPOD mode at $St = 1.5$; (c) generated streamlines.

Near wake structures

The unsteady wake flow around the building determines the building's unsteady loading. As already discussed, the action of the open-loop forcing, the synthetic jet on the top surface, is to enhance the downwash flow, subsequently affecting the wake. The corresponding effect of this forcing on the near wake structures around the building is now analysed.

Snapshots of the instantaneous flow fields around the high-rise building for the unforced case and the controlled case are illustrated in figure 4.16, where the vortical structures are identified by the iso-surfaces of the Q-criterion. The horseshoe vortex wrapping around the front bottom of the building can be observed in both cases, while the shear layer flow separated from the top-surface leading edge is much closer to the building top surface in the presence of control, consistent with the time-averaged results obtained in Sec 4.3.2. Moreover, the vortices in the wake behind the building are shifted to the

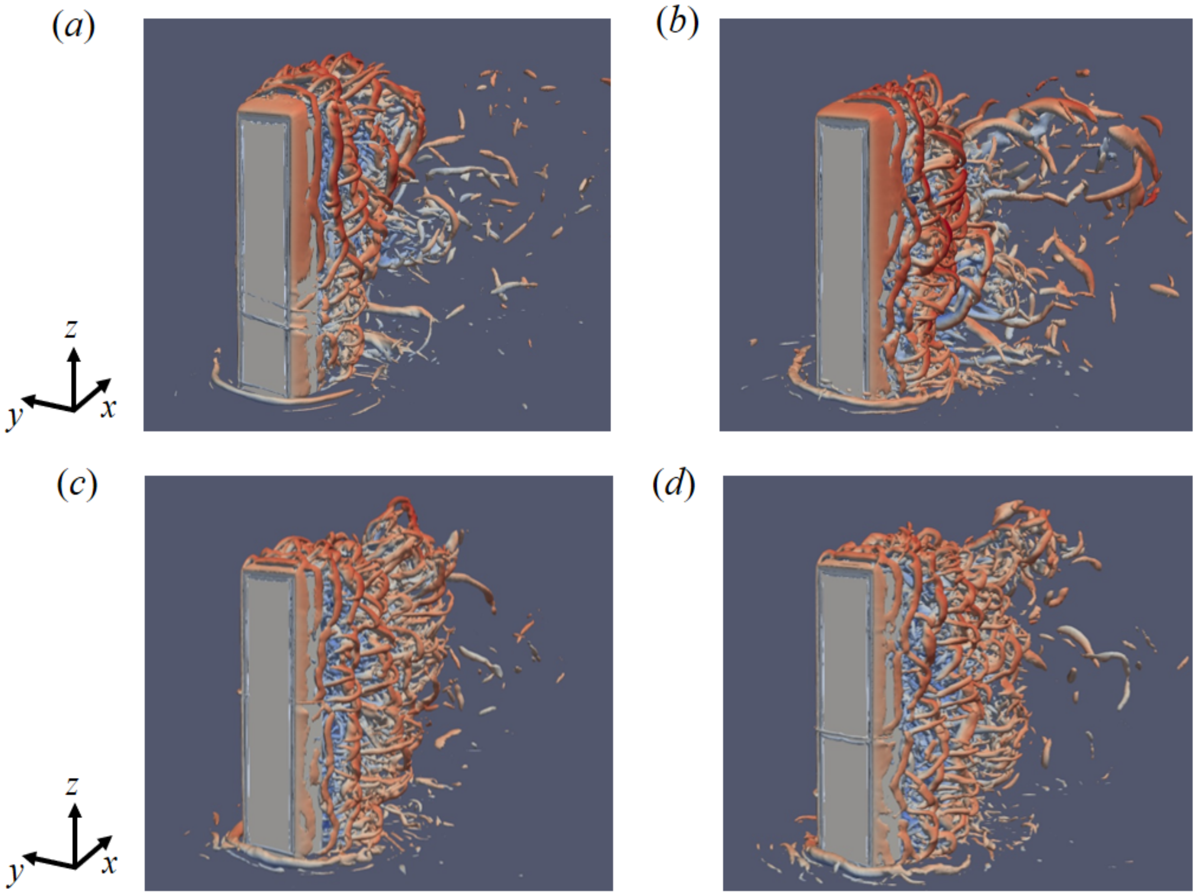

Figure 4.16: Instantaneous snapshots for iso-surfaces of Q-criterion colored by velocity at $\alpha = 0°$ in (a, b) the unforced case; (c, d) the controlled case of $St_f = 1.5$.

lower positions under the effect of the synthetic jet, consistent with the enhancement of the downwash flow.

For the unforced case, two types of spanwise vortex shedding behaviour, antisymmetric and symmetric vortex shedding, have been identified in the flow around the building immersed in the atmospheric boundary layer. As discussed in Chapter 3, the antisymmetric vortex shedding mode is prevalent in the near wake and dominates the unsteady loading on the building (Hu & Morgans, 2022). The effect of the synthetic jet on the spanwise vortex shedding is now investigated in more detail. Figure 4.17 shows the fluctuations of the pressure coefficient on the right and left side faces of the building,

C'_{pr} and C'_{pl}, for the unforced flow and in presence of control at three different heights of the building. The instantaneous results of 40000 samples are shown in these scatter plots. These plots are able to shed light on the side-to-side symmetry of the fluctuations (Bourgeois *et al.*, 2013). If the fluctuations are in phase, corresponding to symmetric flow structures, a positive gradient will be observed, while if the fluctuations are out of phase, corresponding to antisymmetric fluctuations, a negative gradient will dominate.

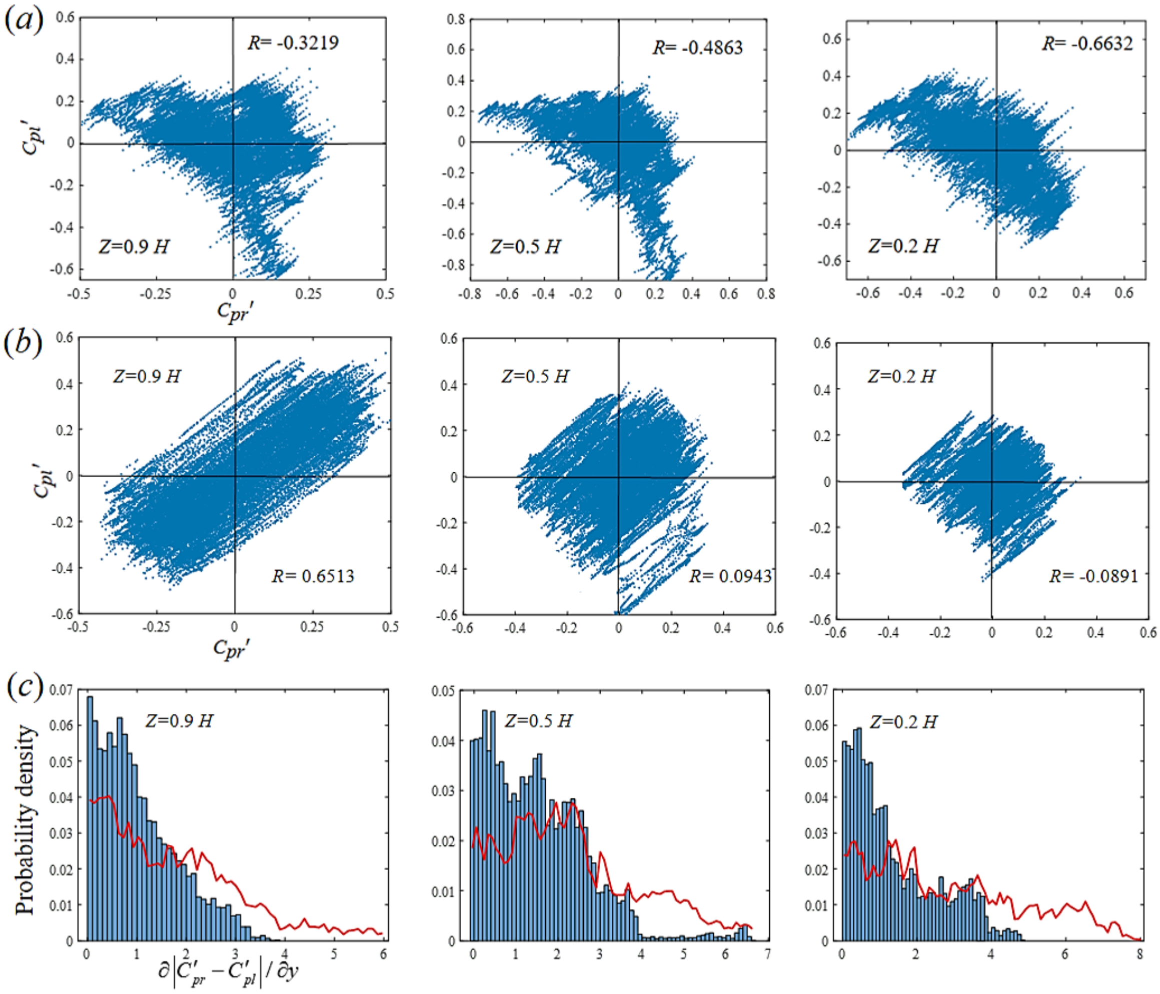

Figure 4.17: Scatter plot for the fluctuation of the pressure coefficient on the right and left building side faces for an oncoming wind angle of $\alpha = 0°$ for (a) the unforced case and (b) the controlled case of $St_f = 1.5$. (c) The corresponding probability distribution of the side pressure gradients for the uncontrolled case (red lines) and the controlled case (blue bars). Three different heights are considered, $z = 0.9H$ near the building top, $z = 0.5H$ at the half-height position and $z = 0.2H$ near the base.

For the unforced case at $z = 0.9H$, the pressure fluctuations on the two opposing faces are negatively correlated, with a correlation coefficient of -0.3219. However, at the same height but in the presence of control at $St_f = 1.5$, most scatter points are located in the first and third quadrants, with the correlation coefficient between C'_{pl} and C'_{pr} being 0.6513. The pressure fluctuations on opposing side faces are in phase most of the time, indicating that the antisymmetric vortex shedding becomes significantly suppressed. At $z = 0.5H$, the correlation coefficients between C'_{pl} and C'_{pr} are -0.4863 for the unforced flow and 0.0943 with control, while at $z = 0.2H$ they are -0.6632 and -0.0891, respectively. Moreover, the effect of the synthetic jet on the side pressure gradient probability density is also shown in figure 4.17. In the presence of control, the side pressure gradient exhibits a distribution much more concentrated around 0 at all three different heights of the building, which also indicates the weakened antisymmetric vortex shedding.

Figure 4.18 shows the pressure fluctuations on the right and left side faces of the building, C'_{pr} and C'_{pl}, at the half-height position $z = 0.5H$ for oncoming wind angles of $\alpha = 10°$ and 20°. For the controlled cases of $St_f = 1.5$ at $\alpha = 10°$ and 20°, the synthetic jet significantly weakens the antisymmetric vortex shedding, similar to its effect at $\alpha = 0°$.

All of these indicate that the synthetic jet weakens the antisymmetric vortex shedding behaviour and enhances the symmetric vortex shedding behaviour along the entire height of the building by enhancing the downwash flow. Since the effect of enhanced downwash flow gradually retreats close to the ground, spanwise antisymmetric vortex shedding is most significantly weakened near the building top. These observations are consistent with the findings reported by Wang & Zhou (2009), Behera & Saha (2019) and da Silva *et al.* (2020) that the free-end downwash flow postpones the antisymmetric vortex shedding.

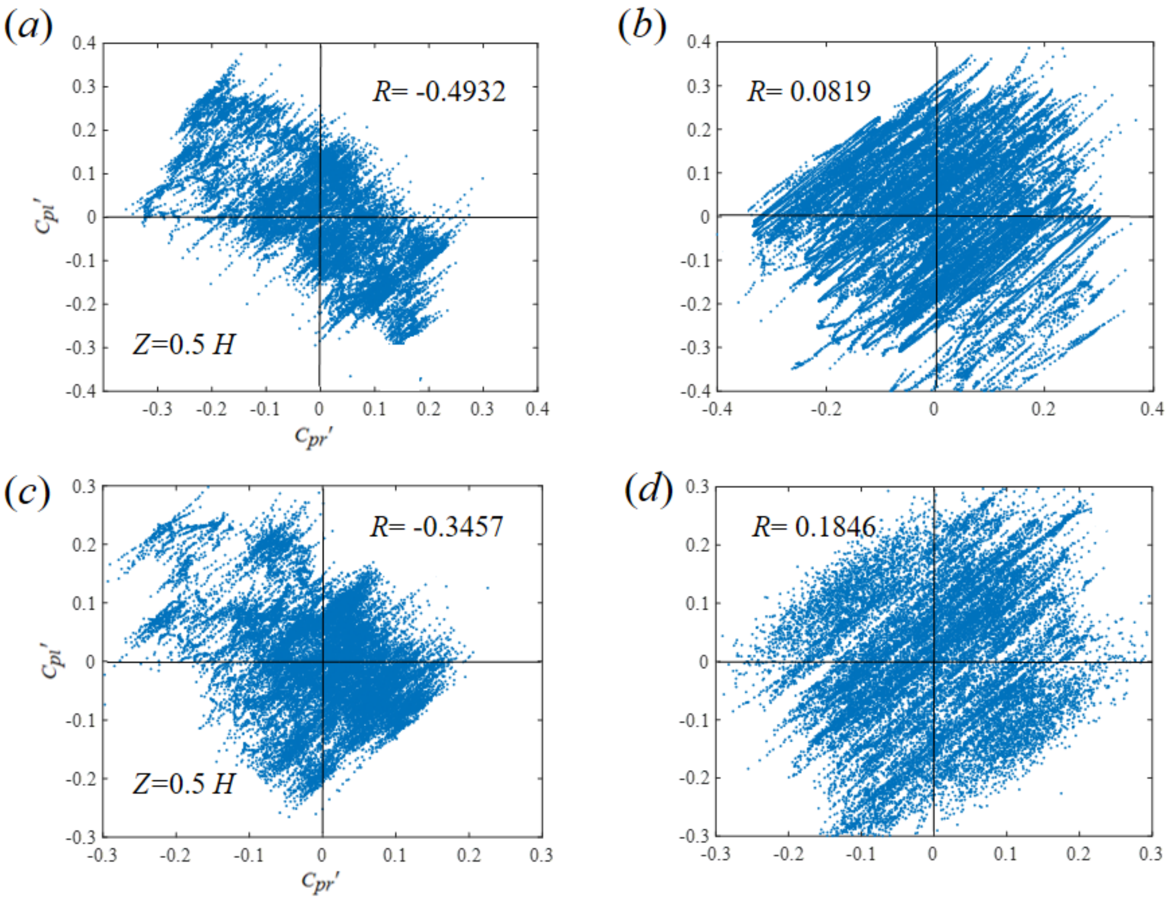

Figure 4.18: Scatter plot for the fluctuation of the pressure coefficient on the right and left building side faces at the half-height position $z = 0.5H$ for (a) the unforced case at $\alpha = 10°$; (b) the controlled case of $St_f = 1.5$ at $\alpha = 10°$; (c) the unforced case at $\alpha = 20°$; (d) the controlled case of $St_f = 1.5$ at $\alpha = 20°$.

In order to further investigate the effect of the synthetic jet on spanwise vortex structures, modal decomposition was also applied to the wake, with SPOD used for wake structure visualization. Figure 4.19(a) shows the energy spectra of the first mode from SPOD of the crosswise velocity component on the xz plane at $y = 0.44B$ for the unforced and controlled cases. For both cases, the spanwise vortex shedding frequency, $St = 0.1$, contains the most energy, as indicated by the main peaks. For the controlled case, the second peak occurs at $St = 1.5$ corresponding to the forcing frequency. Figure 4.19(b) and 4.19(c) show the first SPOD mode of the crosswise velocity component at the spanwise vortex shedding frequency, $St = 0.1$, for the unforced case and the controlled case respectively. The first mode for these two cases exhibits similar behaviours: coherent structures corresponding to antisymmetric vortex shedding are observed, with the structures shed uniformly along the entire building height. However, in the presence of the synthetic jet, the dominant coherent structures are weakened and appear further downstream. This is consistent with the attenuation of the pressure force fluctuations occurring in the presence of control.

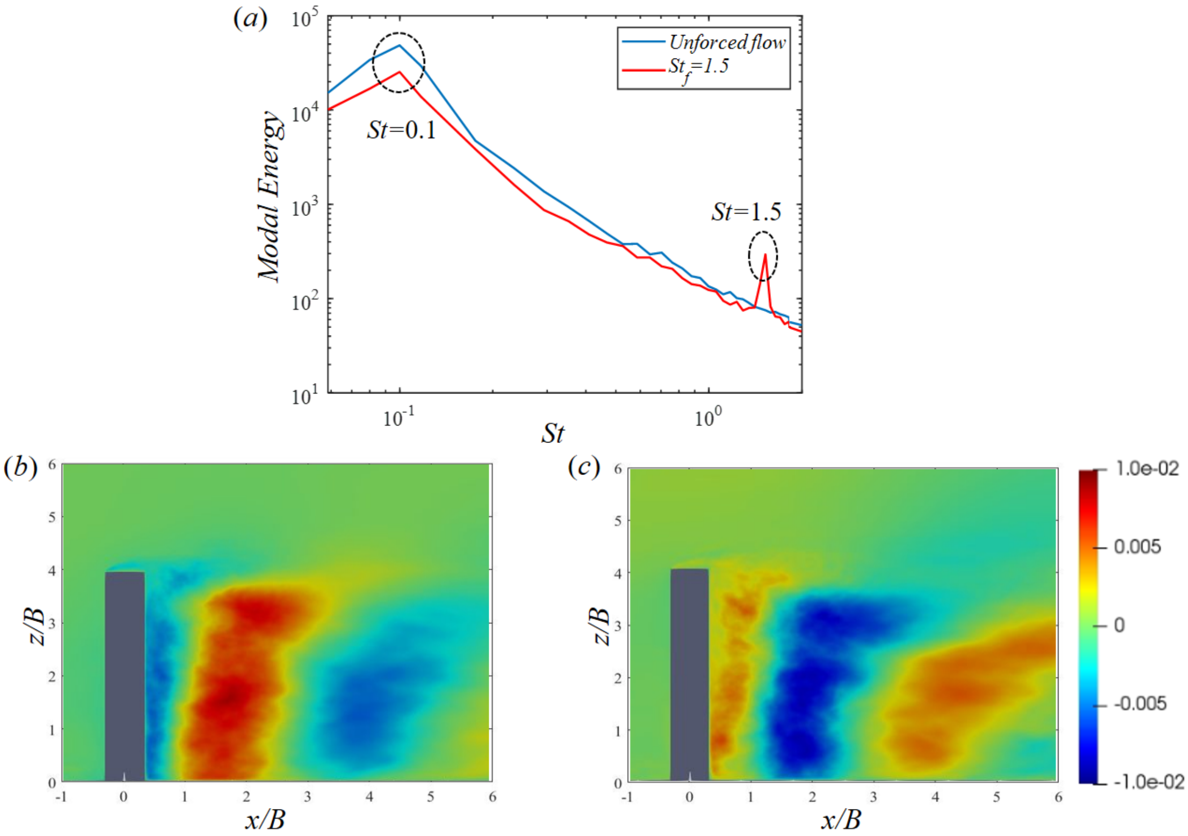

Figure 4.19: SPOD spectra and first SPOD mode on the xz plane at $y = 0.44B$ for an oncoming wind angle of $\alpha = 0°$. (a) Energy spectra of the first SPOD mode for the unforced case and the controlled case. (b) First SPOD mode of crosswise velocity component at $St = 0.1$ for the unforced case. (c) First SPOD mode of crosswise velocity component at $St = 0.1$ for the controlled case.

In order to further investigate the effect of the synthetic jet on spanwise vortex structures at $\alpha = 10°$ and $20°$, modal decomposition was also applied to the wake, with SPOD used for wake structure visualization. The first SPOD modes of the crosswise velocity component on the xz plane at the spanwise vortex shedding frequency for the cases of $\alpha = 10°$ and $20°$ are shown in figures 4.20 and 4.21 respectively. The first modes of the unforced flow at these two wind angles do not change much compared to the case at $\alpha = 0°$, exhibiting coherent structures along the entire building height corresponding to antisymmetric vortex shedding. For the controlled cases of $St_f = 1.5$ at $\alpha = 10°$ and $20°$, the vortex shedding is still weakened and the actuation results in the coherent structures being located further downstream, this being especially pronounced closer to the ground.

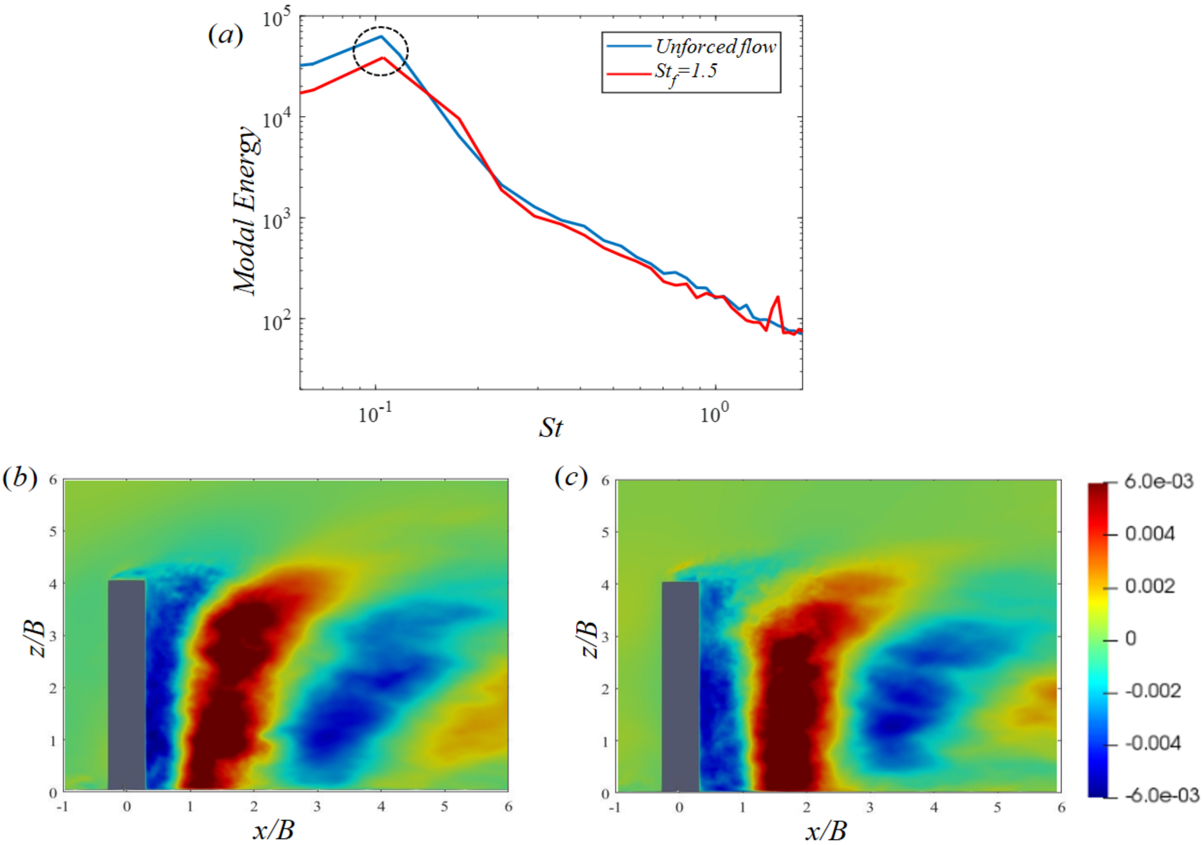

Figure 4.20: SPOD spectra and first SPOD mode on the xz plane at $y = 0.44B$ for an oncoming wind angle of $\alpha = 10°$. (a) Energy spectra of the first SPOD mode for the unforced case and the controlled case. (b) First SPOD mode of crosswise velocity component at $St = 0.1$ for the unforced case. (c) First SPOD mode of crosswise velocity component at $St = 0.1$ for the controlled case.

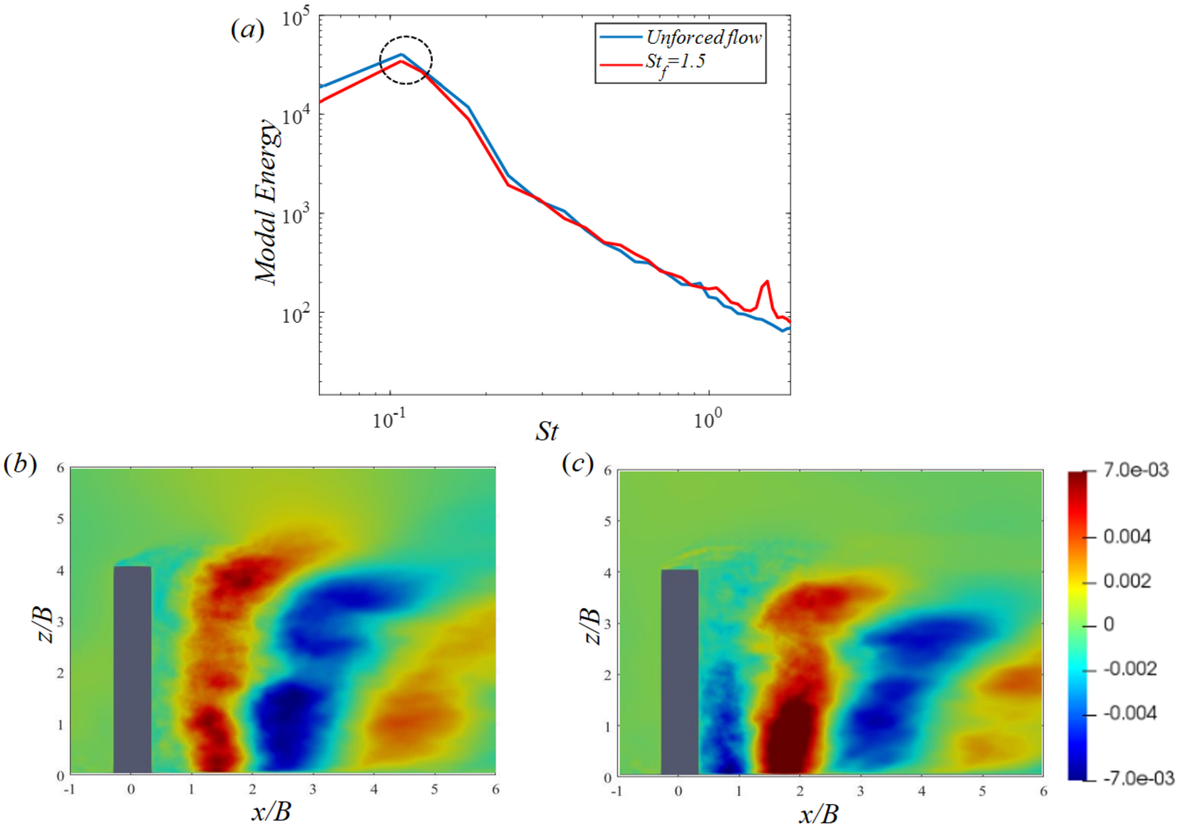

Figure 4.21: SPOD spectra and first SPOD mode on the xz plane at $y = 0.44B$ for an oncoming wind angle of $\alpha = 20°$. (a) Energy spectra of the first SPOD mode for the unforced case and the controlled case. (b) First SPOD mode of crosswise velocity component at $St = 0.1$ for the unforced case. (c) First SPOD mode of crosswise velocity component at $St = 0.1$ for the controlled case.

4.4 Summary

In this work, an open-loop active control method employing a synthetic jet on the top surface was proposed to mitigate the unsteady loading of a high-rise building exposed to differing oncoming wind directions. A canonical high-rise building, known as the CAARC model, was studied, and four different oncoming wind angles were considered. The behaviour of the synthetic jet and its effect on the flow structures around the building was studied numerically using wall-resolved large eddy simulations.

Synthetic jet open-loop forcing at three different frequencies, all at least half an order of magnitude larger than the main vortex shedding frequency, were considered. Across all conditions, the synthetic jet attenuated the side-force fluctuations of the building. Actuation at the high frequency, $St_f = 1.5$, was identified as exhibiting good performance for all oncoming wind angles. The influence of the synthetic jet on the time-averaged flow structures was analysed, with it being found that the downwash flow is enhanced significantly and the recirculation region is extended in the streamwise direction under its effect.

The effect of control on the frequency spectra of the fluctuating aerodynamic force was investigated, with control seen to weaken the peak at the vortex shedding frequency. A SPOD analysis for the controlled case of $St_f = 1.5$ at an oncoming wind angle of $\alpha = 0^\circ$ confirmed that the synthetic jet enhances the turbulent fluctuation above the top surface, but has no direct impact on the side-force fluctuation. The enhanced turbulent fluctuation induces a stronger downwash flow, which could further influence the spanwise vortex shedding. The unsteady near wake structures in the unforced and controlled cases were also investigated, with the synthetic jet found to suppress antisymmetric spanwise vortex shedding and promote symmetric vortex shedding, which is ascribed to the enhanced downwash flow. The formation of dominant vortices is also delayed by the synthetic jet, which can further reduce the pressure fluctuations on the building caused by these vortices.

Chapter 5

Attenuation of unsteady loading using H_∞ loop-shaping feedback control

5.1 Introduction

This present chapter considers whether the design of a single SISO (single-input single-output) feedback controller can mitigate the unsteady wind loading of a high-rise building across different oncoming wind angles. In order to choose the sensor and actuation that are effective across different oncoming wind angles, the unforced flow structures across different wind angles are investigated in more detail than in Chapter 4, by combining LES with modal analysis of the dominant flow structures and analysis of harmonic open-loop forcing results across different wind angles. Linear system identification is then employed to identify low-order linear models for how the chosen sensor signal responds to actuation for each wind angle. A SISO feedback control strategy aiming to attenuate the side-force fluctuation across differing wind directions is then developed. To account for the difference in open-loop transfer functions for different wind angles, the feedback control strategy employs the H_∞ loop-shaping method (McFarlane & Glover, 1992), which provides for tradeoffs between good performance and robust stability and has been successfully applied to other flow control problems with differing open-loop transfer functions (Flinois & Morgans, 2016; Li & Morgans, 2016). The present study performs what we believe is the first attempt to employ an H_∞ loop-shaping control strategy with the aim of reducing the unsteady loading of a high-rise building exposed to differing oncoming wind directions.

This chapter presents the chosen actuator and sensor signals in section 5.2 followed by the presentation of the system identification for different oncoming wind angles in section 5.3. The designed feedback control strategy and its effect on the unsteady wind loading are studied in section 5.4.

5.2 Choice of sensor signals and actuator

The wind angle range from 0° to 45° can capture most of the unsteady loading variation (Obasaju, 1992), and three characteristic oncoming wind angles, $\alpha = 0°$, $20°$ and $45°$, are studied in this chapter.

The unforced flow field around the building determines its unsteady loading and informs the choice of actuator and sensor signals. The numerical setup and validation for the unforced flows at $\alpha = 0°$, $20°$ and $45°$ are described in Chapter 4. The flow structures at three different wind angles are investigated using POD analysis. The streamwise velocity components of the first POD mode in the horizontal slice at three oncoming wind angles are shown in figure 5.1. All of them exhibit the antisymmetric coherent

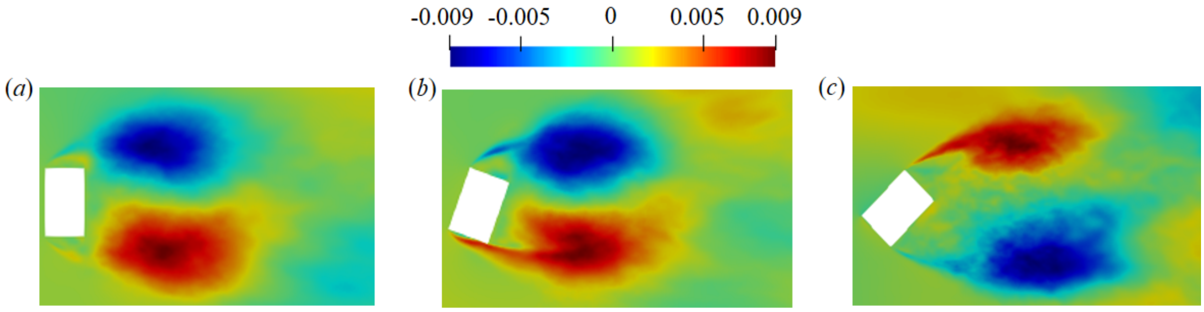

Figure 5.1: Streamwise velocity components of the first POD mode at $z = 0.5H$ for the unforced flow at (a) $\alpha = 0°$; (b) $\alpha = 20°$; (c) $\alpha = 45°$.

vortex structures behind the building, confirming the dominance of the large-scale von Kármán antisymmetric vortex shedding mode in the near wake. For an oncoming wind angle of $\alpha = 0°$, the antisymmetric spanwise vortex shedding with the separation near both leading edges is observed. For an oncoming wind angle of $\alpha = 20°$, the flow still separates at the leading edges of two side faces, with reattachment of the separated shear layer observed on the lower side face. A second flow separation occurs at the trailing edge of the lower side. At $\alpha = 45°$, the main flow separation occurs at the leading edge of the upper side face and the trailing edge of the lower side, which is significantly different from the case at $\alpha = 0°$.

In terms of sensor signals, the antisymmetric component of the base pressure force used in Chapter 3 performs well for an oncoming wind angle of $\alpha = 0°$. Figure 5.2 shows the spectrum of the antisymmetric base pressure force for an oncoming wind angle of $\alpha = 45°$. At $\alpha = 45°$, the main vortex shedding frequency of the unsteady loading cannot be captured clearly, and thus this signal is not feasible to the feedback controller design across different wind angles.

Given that the fluctuating C_{Fxb} is more dependent on the inflow turbulence rather than the near wake dynamics, a possible choice is the side-force fluctuation of the high-rise building. The spectra of the side-force fluctuation for the unforced cases at three

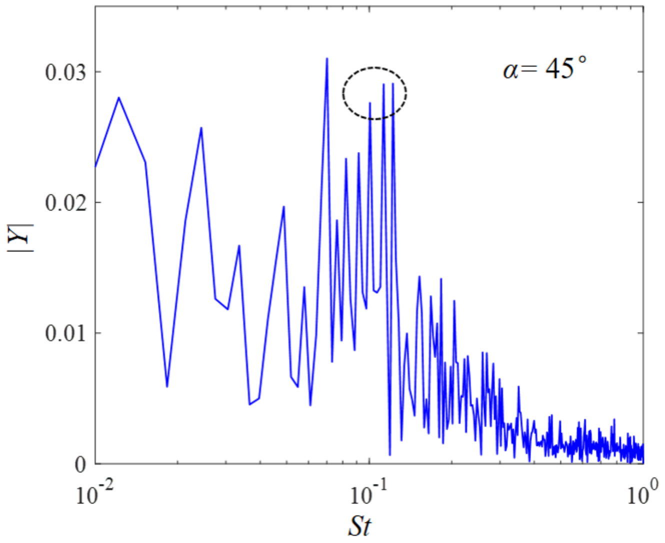

Figure 5.2: FFT spectra of the antisymmetric base pressure force signal for an oncoming wind angle of $\alpha = 45°$.

oncoming wind angles are shown in figure 5.3. The proposed sensor signals exhibit a narrow peak at the antisymmetric vortex shedding frequency, around $St = 0.1$, across these three different wind angles. For future practical applicability, this unsteady side-force fluctuation signal is measured directly using pressure sensors on the two side faces of the building, which can capture the unsteadiness in spanwise antisymmetric vortex shedding.

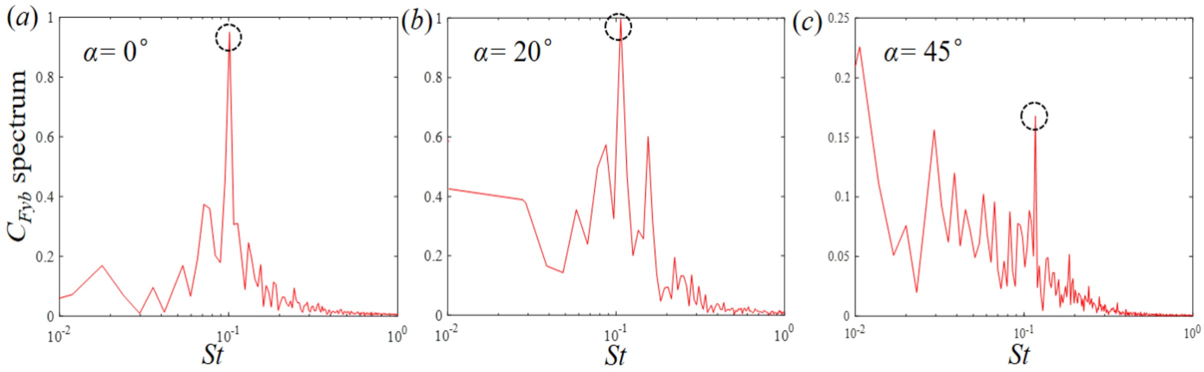

Figure 5.3: Spectra of the building's side-force fluctuation, C_{Fyb}, for oncoming wind angles of (a) $\alpha = 0°$; (b) $\alpha = 20°$; (c) $\alpha = 45°$.

Synthetic slot jets are chosen as the actuation to attenuate the unsteady loading. They should act on the large-scale flow separation from the leading edges of the building, which can ensure that the actuation strategy has good control authority across different oncoming wind directions. Linear system identification is employed to identify the open-loop transfer function describing how the sensor signals respond to the actuation. The design of a robust controller will be based upon the assumption of dynamic linearity, thus the degree to which this assumption holds will be checked. The assumption implies that a sinusoidal actuation signal will produce a sensor signal with the same dominant frequency and with the gain and phase shift independent of forcing level.

Based on the unforced flow features at three wind angles, three actuation configurations shown in figure 5.4 are investigated. The first slot jet actuation is located on the top surface of the high-rise building and injects along the vertical (z) direction. This aligns with the manner in which the open-loop controller setup, as described in Chapter 4. However, this actuation acts on the downwash flow to attenuate the unsteady loading instead of acting on the wake directly. According to the frequency analysis for this open-loop controller shown in figure 4.11, there is no corresponding frequency peak for the sensor signal in response to the open-loop forcing, and thus this actuation strategy is not feasible to the feedback controller design.

The other two actuation configurations directly act on the spanwise vortex shedding. As shown in figure 5.1, flow separation occurs at the leading edge on the upper side face for cases of $\alpha = 0°$, $20°$ and $45°$. Thus the synthetic slot jets are implemented near the upper side face leading edge in both actuation configuration 2 and 3. In actuation configuration 2, two synthetic jet slots located near the leading edges of the building side faces extend along the entire cylinder span and the injection angle relative to the building's side face is 45 degrees, the same as the actuation strategy applied in Chapter 3. The two synthetic slot jets are out of phase and operate simultaneously. In terms of

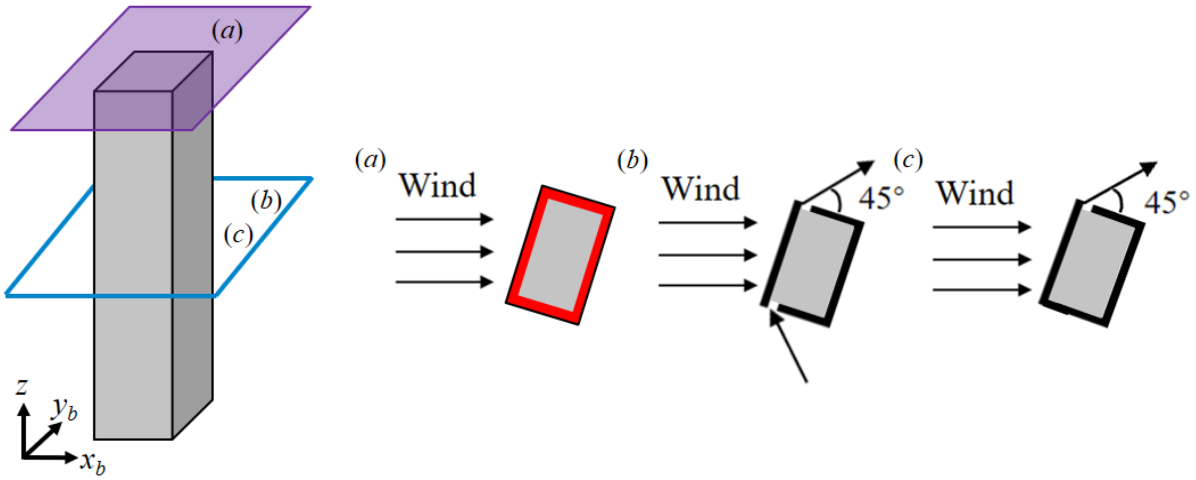

Figure 5.4: (a) Actuation configuration 1: a synthetic jet on the top surface, which injects in the upward ($+z$) direction. (b) Actuation configuration 2: synthetic jets near the leading edges of two side faces, which extend along the entire building height. (c) Actuation configuration 3: a synthetic jet near the leading edge of the upper side face, which extends along the entire building height.

Actuation	Dynamic linearity at $\alpha = 0°$	Dynamic linearity at $\alpha = 20°$	Dynamic linearity at $\alpha = 45°$
Actuation configuration 1	✗	✗	✗
Actuation configuration 2	✓	✓	✓
Actuation configuration 3	✗	✗	✓

Table 5.1: Summary of the open-loop forcing study for three actuation configurations for three oncoming wind angles.

actuation configuration 3, only the jet near the upper side face leading edge is employed.

Harmonic forcing simulations based on these two actuation configurations at three different oncoming wind angles are applied to test whether the assumption of dynamic linearity holds. The results, summarized in table 5.1, show actuation configuration 2 is effective at all three wind angles, and the response of the sensor signal to the forcing can be considered dynamically linear. Thus the second actuation configuration is employed in the H_∞ loop-shaping feedback controller design.

5.3 System Identification

The feedback control system is summarised in the schematic in figure 5.5. It is clear that a low-order linear model for $G(s)$ must be identified in order to design the feedback controller. Open-loop transfer functions at three different oncoming wind angles describing how the sensor signals respond to actuation signals need to be identified.

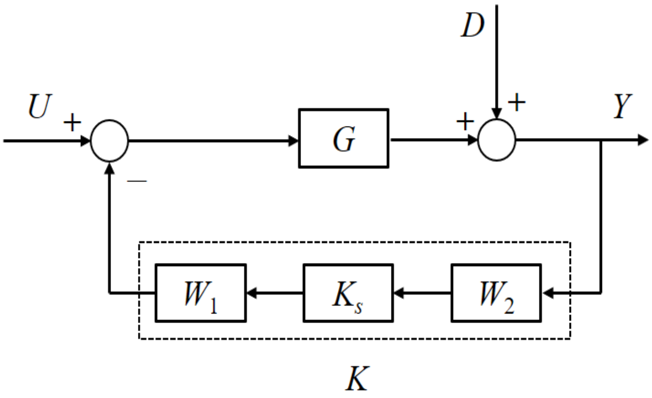

Figure 5.5: Schematic for the H_∞ loop-shaping feedback control system.

Given the assumption that the sensor response induced by open-loop forcing is approximately dynamically linear, open-loop transfer functions for three oncoming wind angles can be identified through linear system identification. Different actuation forcing signals can be applied in order to perform system identification. Based on the spectra of figure 5.3, the open-loop forcing frequency range was chosen to be $0.05 \leq St \leq 1$, with different amplitudes considered.

Once transients in the sensor signals had decayed to low levels, the sensor signals were recorded and the gain and phase shift of the open-loop response were extracted using spectral analysis. The results for all three oncoming wind angles, shown in figure 5.6, first confirm that their frequency responses vary little with forcing amplitude A_j for frequencies across the considered range. Hence the responses of the sensor signal to the

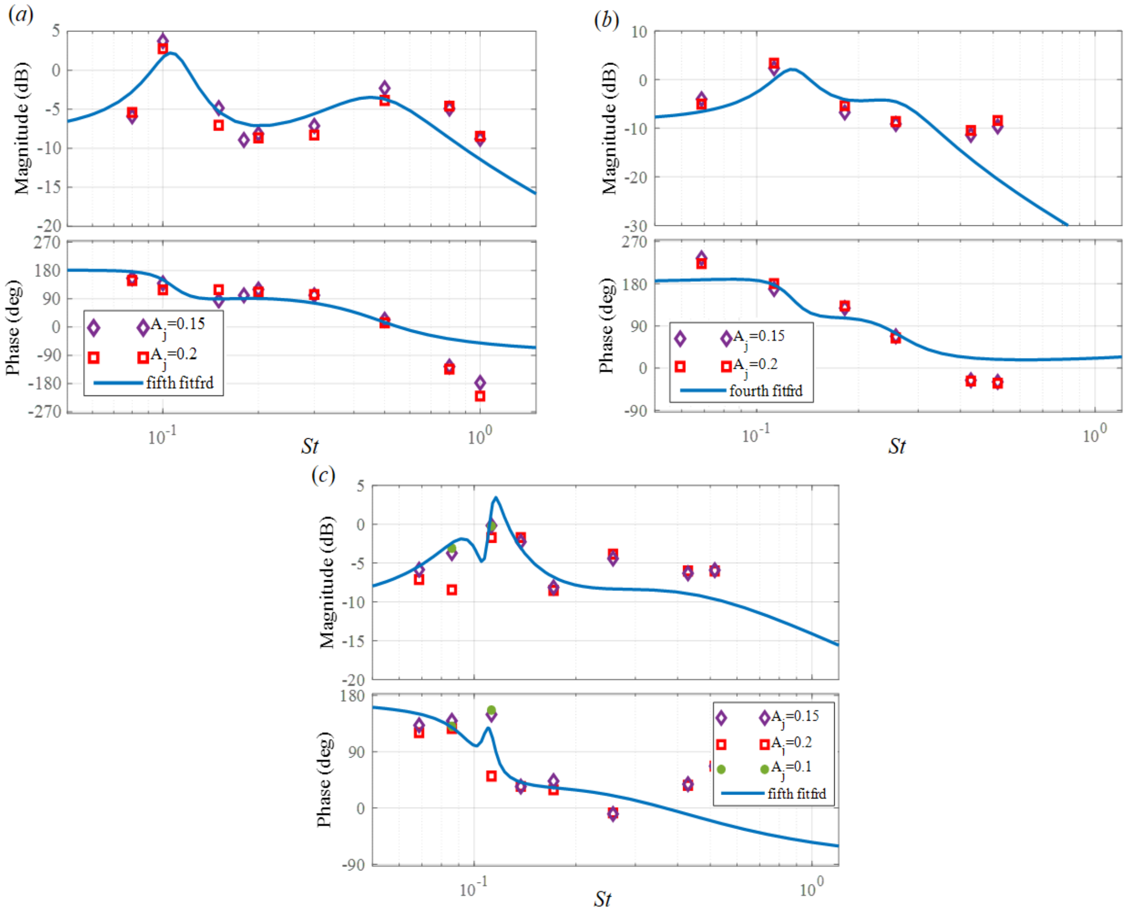

Figure 5.6: System identification data resulting from open-loop harmonic forcing at (a) $\alpha = 0°$; (b) $\alpha = 20°$; (c) $\alpha = 45°$.

forcing can be considered dynamically linear. The average gains and phase shifts across the different forcing amplitudes are calculated, and the Matlab `fitfrd` command is used to fit the frequency-domain response data with linear state-space models, as shown in figure 5.6.

5.4 H_∞ loop-shaping feedback control

5.4.1 The ν-gap metric and H_∞ loop-shaping

A fundamental factor in describing robustness is to determine whether two open-loop systems are similar in a feedback loop. Two systems may not be close from the point of view of feedback even if their open-loop performances are quite similar (Åström & Murray, 2021). The ν-gap metric introduced by Vinnicombe (2000) can be used to compare two SISO open-loop systems in a way that reflects their closed-loop performance. The ν-gap can be calculated based on the chordal metric applied to two different open-loop systems, $G_1(s)$ and $G_2(s)$, written as follows,

$$d_{G_1G_2}(\omega) = \frac{\left|G_1(i\omega) - G_2(i\omega)\right|}{\sqrt{1+\left|G_1(i\omega)\right|^2}\sqrt{1+\left|G_2(i\omega)\right|^2}}, \tag{5.1}$$

where ω is the angular frequency. The ν-gap metric is then defined as

$$\delta_v(G_1, G_2) = \sup_{\omega} d_{G_1G_2}(\omega), \tag{5.2}$$

if the following conditions are satisfied

$$\begin{cases} 1 + G_1(i\omega) G_2(-i\omega) \neq 0 \quad \forall\omega \quad \text{and} \\ \text{wno}\left(1 + G_1(i\omega) G_2(-i\omega)\right) + \eta(G_1) - \eta(G_2) = 0 \end{cases} \tag{5.3}$$

where wno(F) is the winding number for the transfer function $F(s)$ around the Nyquist contour, and n represents the number of poles at the right-hand plane. $d_{G_1G_2}(\omega) = 1$ when two open-loop systems cannot satisfy the above conditions.

Classical linear loop shaping is always used to design a feedback controller based on a known open-loop transfer function. The performance of the designed controller is not guaranteed when applied to different open-loop transfer functions e.g. those at different wind angles. Since we aim to design a single feedback controller that suppresses unsteady leading across a variety of wind angles, we therefore move to modern linear robust control strategies that can guarantee both good performance and robustness of the closed-loop system. Here the H_∞ loop-shaping procedure proposed by McFarlane & Glover (1992), which combines classical loop-shaping and robust stabilization, is used to obtain a robust feedback controller. This method applies to multi-input multi-output (MIMO) systems, with some simplification possible for SISO systems such as the one being considered here.

The feedback control system using H_∞ loop-shaping is summarised in the schematic in figure 5.5. A pre-compensator W_1 and a post-compensator W_2 are selected to modify the shape of open-loop transfer functions. In terms of SISO systems, the shaping can be simplified to designing a single compensator which moves the open-loop system towards the desired shape in the frequency domain. An H_∞ controller, K_s, is then synthesized to robustly stabilize the system. The H_∞ norm of the closed-loop system can be written as

$$\gamma = \left\| \begin{bmatrix} I \\ G_s \end{bmatrix} (I - K_s G_s)^{-1} [I, K_s] \right\|_\infty \tag{5.4}$$

where $G_s = W_1 G W_2$ is the shaped plant. The generalized stability margin of the closed-loop system, b, is the inverse of γ. The H_∞ controller, K_s, is synthesized to achieve the minimal γ which maximizes the stability margin while not substantially affecting the gain of the shaped transfer function. The `ncfsyn` command in MATLAB is used to identify the optimal controller K, with the final feedback controller being $K = W_1 K_s W_2$, and the resulting stability margin for the feedback loop can be also returned.

This stability margin provides a robust stability guarantee for the closed-loop system and can fit the ν-gap metric naturally into H_∞ loop-shaping control design. For two SISO open-loop transfer functions $G_1(s)$ and $G_2(s)$, if the stability margin of the H_∞ loop-shaping controller designed based on $G_1(s)$ exceeds the ν-gap metric between two open-loop transfer functions, this controller is also guaranteed to stabilize $G_2(s)$.

5.4.2 Controller design and implementation

H_∞ loop-shaping feedback controller design requires a reference linear model $G_{ref}(s)$. The ν-gap metric can then be used to characterise the differences between the reference model and the open-loop transfer functions at the different oncoming wind angles. The open-loop forcing results across all oncoming wind angles can be used to identify the reference model used in the H_∞ loop-shaping controller design. For each frequency, the average gains and phase shifts across the different forcing amplitudes at each wind angle are collected, and the reference system identified through a frequency-domain fitting procedure using the MATLAB command `fitfrd`. Since the designed controller typically has an order comparable to that of the shaped plant, a fifth-order fit is chosen to avoid a high order of the designed controller, as shown in figure 5.7(a).

Figure 5.7(b) compares the frequency response of the reference system to the open-loop transfer functions at three oncoming wind angles. The ν-gaps between this reference system and open-loop transfer functions at three oncoming wind angles can be identified from the frequency variations of $d_{G_1 G_2}(\omega)$ at frequencies ranging from 0.05 to 1, shown in figure 5.8. The relatively large values can be observed in the low-frequency region, and the maximum value of the ν-gap across all different wind angles is 0.35 occurring at $\alpha = 0^\circ$.

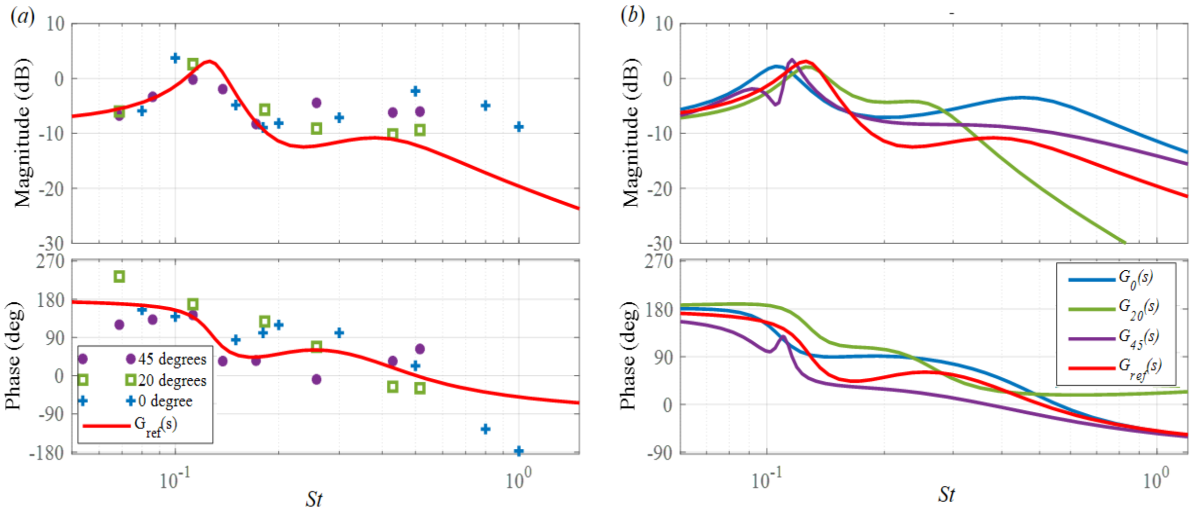

Figure 5.7: Frequency response: gains and phase shifts for (a) system identification data for the reference linear model; (b) all open-loop transfer functions.

In terms of the H_∞ loop-shaping controller, since we are employing SISO control for the open-loop transfer function $G_{ref}(s)$, we only use the pre-compensator W_1 and set $W_2 = 1$. To suppress the fluctuations in the sensor signal, the feedback controller $W_1(s)$ is designed such that the magnitude of the sensitivity transfer function is less than unity over the frequency range where the wake exhibits significant dynamics, consistent with that in Chapter 3. The conventional loop-shaping method is used to design the feedback controller $W_1(s)$ to achieve this. The MATLAB command `ncfsyn` is then used to perform a H_∞ loop-shaping synthesis. This is an iterative process, where, depending on the returned value of b, small iterations to the exact form of W_1 are performed. The stability margin achieved by the designed controller for this reference system needs to be larger than the maximum value of ν-gap across all oncoming wind directions. The final designed feedback controller has an order of 8, and the stability margin is $b = 0.531$, noticeably larger than the maximum ν-gap value, suggesting the controller should guarantee the closed-loop stability of all open-loop models.

For the designed controller, we assess its performance by calculating the sensitivity

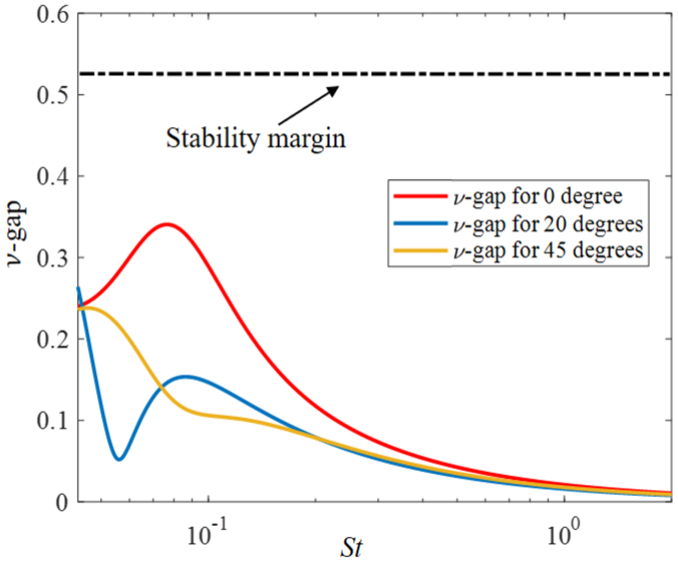

Figure 5.8: Frequency variation of ν-gaps value between the reference system and open-loop transfer functions at three oncoming wind angles.

functions at different oncoming wind directions. Figure 5.9 shows resulting sensitivity functions for three different wind angles in the presence of the feedback controller $K(s)$, where it can be seen that $|S(i\omega)| < 1$ is achieved at the frequency range of $0.09 \leq St \leq 0.18$. For the wind angle of $\alpha = 45°$, it can be noticed that the controller works well in the targeted frequency range, although the gain of the sensitivity transfer function at $St = 0.26$ becomes relatively high, suggesting the disturbances around $St = 0.26$ might be amplified.

The controller was implemented in a discrete-time format in the LES in order to test its performance at three oncoming wind angles. When implementing the feedback flow control into the flow simulations, the actuators, whose signal at each time step is generated following the variation of the sensor signal, require a time-varying boundary condition. As in Chapter 3, the plugin SWAK4FOAM library allowing user-defined equations for boundaries was used.

The effects of the H_∞ loop shaping controller on the side-force fluctuation of the high-rise

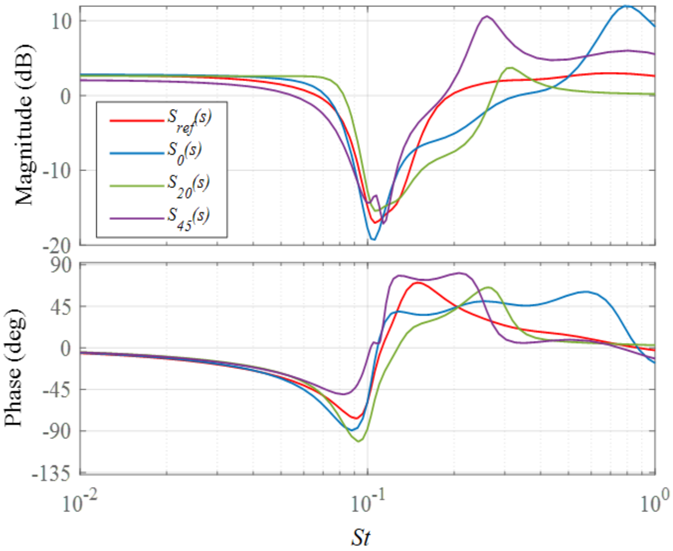

Figure 5.9: Frequency responses of sensitivity functions for three oncoming wind angles.

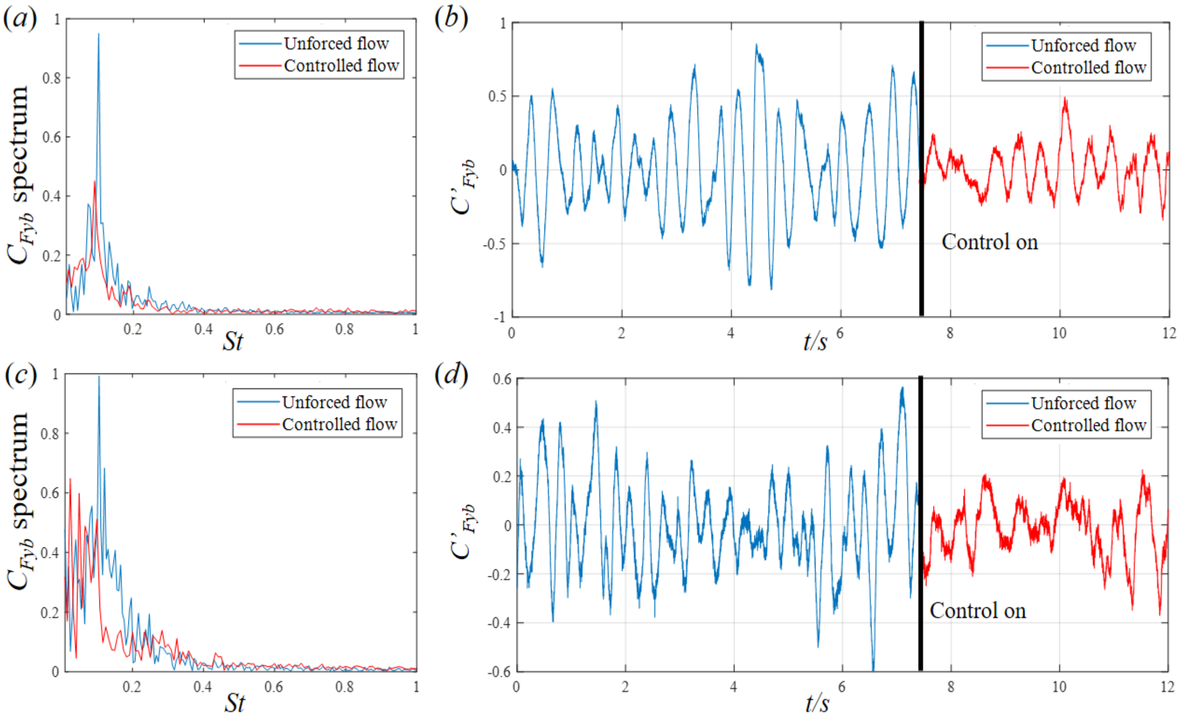

Figure 5.10: Effect of the controller: comparison between cases with and without feedback control in (a) spectrum for the side-force fluctuations for a wind angle of $\alpha = 0°$; (b) time history for the side-force fluctuations for a wind angle of $\alpha = 0°$; (c) spectrum for the side-force fluctuations for a wind angle of $\alpha = 20°$; (d) time history for the side-force fluctuations for a wind angle of $\alpha = 20°$.

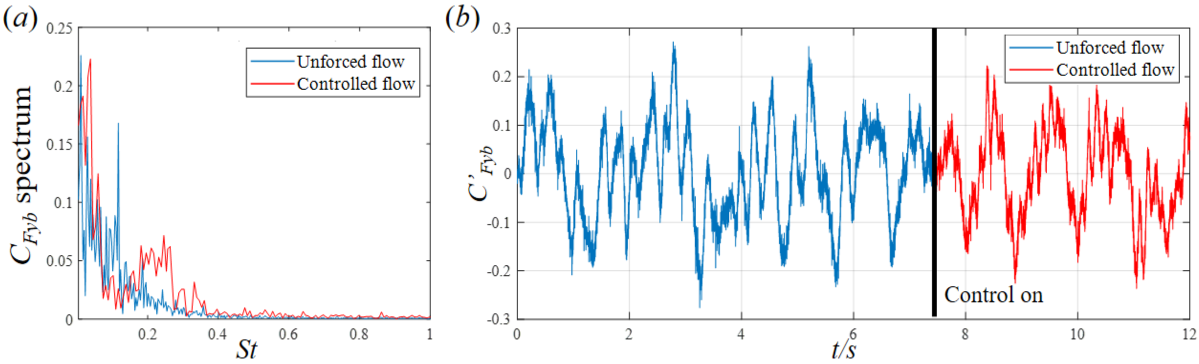

Figure 5.11: Effect of the controller: comparison between cases with and without feedback control in (a) spectrum for the side-force fluctuations for a wind angle of $\alpha = 45°$; (b) time history for the side-force fluctuations for a wind angle of $\alpha = 45°$.

building across differing wind angles are shown in figure 5.10 and 5.11. The feedback control strategy is effective in reducing successfully the fluctuation of C_{Fyb} over the targeted frequency range for all oncoming wind directions. The r.m.s. values of C_{Fyb} were reduced by approximately 48 % and 33 % via the H_∞ loop-shaping controller for oncoming wind angles of $\alpha = 0°$ and $20°$ respectively. The attenuation remains present but smaller for $\alpha = 45°$, although the side-force fluctuations are so much smaller in absence of control at this wind angle. At $\alpha = 45°$, the H_∞ loop-shaping feedback controller attenuates the amplitude response around the vortex shedding frequency, while a peak occurs at $St = 0.25$. Considering the sensitivity function at $\alpha = 45°$ shown in figure 5.9, this frequency feature of the controlled flow might result from the designed controller.

The changes to the time-averaged flow field for an oncoming wind angle of $\alpha = 0°$ after implementing the H_∞ loop shaping controller are shown in figure 5.12. The recirculation region has been extended in the streamwise direction, in a manner similar to the linear feedback controller used in Chapter 3.

The controller aims to be effective in mitigating the side-force fluctuations across differing oncoming wind angles. Therefore, in addition to the three oncoming wind angles used in

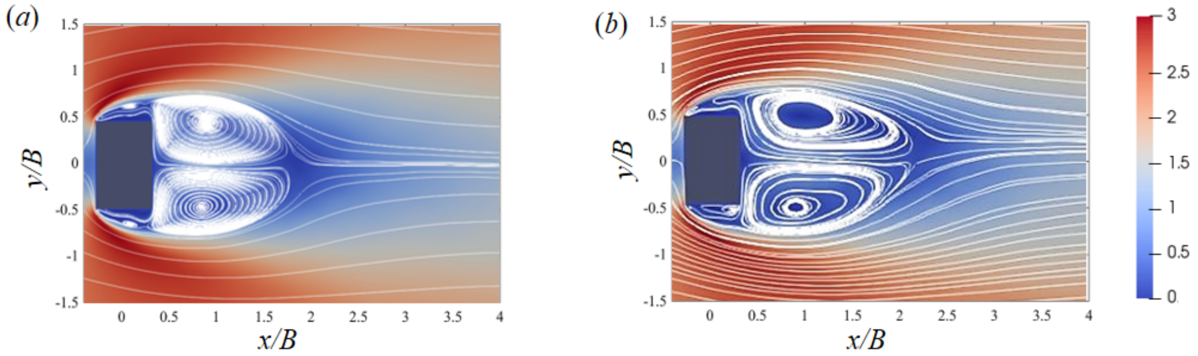

Figure 5.12: Colour contours of the time-averaged streamwise velocity and streamlines for an oncoming wind angle of $\alpha = 0°$: (a) unforced flow; (b) controlled flow.

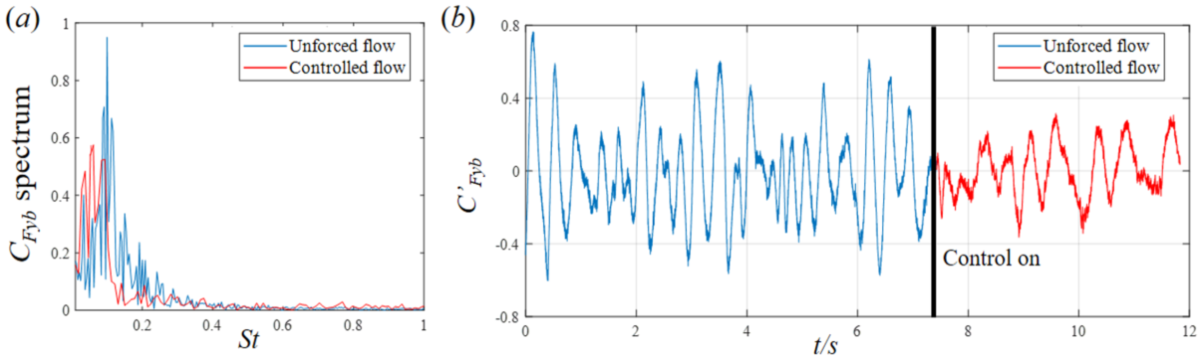

Figure 5.13: Effect of the controller: comparison between cases with and without feedback control in (a) spectrum for the side-force fluctuations for a wind angle of $\alpha = 10°$; (b) time history for the side-force fluctuations for a wind angle of $\alpha = 10°$.

the controller design, the controller was also implemented in the numerical simulation at $\alpha = 10°$ to evaluate its control performance. The open-loop transfer function for $\alpha = 10°$ has not been identified and was not used as part of the controller design process. The effects of the H_∞ loop shaping controller on the side-force fluctuation of the high-rise building for the oncoming wind angle of $\alpha = 10°$ are shown in figure 5.13. The feedback control strategy is effective in reducing successfully the side-force fluctuation around the vortex shedding frequency, attenuating the fluctuations of C_{Fyb} by approximately 39 %, demonstrating the success of the feedback control at $\alpha = 10°$.

5.5 Summary

In this chapter, an H_∞ loop-shaping feedback control method employing a synthetic jet along the leading edges of the building's side faces was proposed to mitigate the unsteady loading of a high-rise building exposed to differing oncoming wind directions. Three different oncoming wind angles, $\alpha = 0°$, $20°$ and $45°$, were investigated and their open-loop transfer functions were identified via linear system identification. A reference linear open-loop transfer function was defined as the target plant used in the H_∞ loop-shaping feedback controller design. The ν-gap metric was employed to quantify the differences between the reference open-loop system and open-loop transfer functions for different oncoming wind angles. The H_∞ loop-shaping controller was then designed to mitigate the side-force fluctuations associated with the antisymmetric vortex shedding, ensuring the controller stability margin exceeded the maximum ν-gap across the important frequency range for all wind angles. The designed controller was further implemented in large eddy simulations and attenuated successfully the building's side-force fluctuations for the three oncoming wind angles. For an oncoming wind angle of $\alpha = 10°$, which had not been part of the controller design process, the controller reduced the side-force fluctuation effectively, demonstrating its success at an off-design wind angle.

Chapter 6

Conclusion

6.1 Summary

The present work has presented high-fidelity wall-resolved large eddy simulations of the flow around a high-rise building in an atmospheric boundary layer, focusing on capturing accurately the unsteady wake dynamics and developing active control techniques for the reduction of the unsteady loading. A canonical high-rise building, known as the CAARC model, was studied, which has a constant rectangular cross-section. The active control strategies studied in this project include feedback control and open-loop control.

In a first part, the flow around a high-rise building with an oncoming wind normal to its wider side was investigated. The switching between antisymmetric to symmetric vortex shedding modes was explored, and the influence of the atmospheric boundary layer on suppressing symmetric vortex shedding was identified. Proper orthogonal decomposition confirmed that the von Kármán antisymmetric vortex shedding mode is prevalent in the near wake, rather than the symmetric mode. The influence of the atmospheric boundary layer was also analysed via the comparison with the uniform inflow case, with it being found that the symmetric vortex shedding mode is suppressed significantly by immersion the atmospheric boundary layer. Two feedback control strategies were then developed, which aimed to attenuate the building's unsteady loading. Both the designed linear controller and the least mean square adaptive controller attenuate successfully the side-force fluctuations by 38 % and 17 %, respectively when implemented in simulations. Feedback control that requires a smaller sensing area is then explored, with a comparable control effect achieved in the attenuation of the unsteady loading.

In a second part, an open-loop active control method employing a synthetic jet on the top surface was proposed to mitigate the unsteady loading of a high-rise building exposed to differing oncoming wind directions. Four different oncoming wind angles were considered, and the behaviour of the synthetic jet and its effect on the flow structures around the building was studied numerically. Across all conditions, the synthetic jet attenuated the side-force fluctuations of the building. Actuation at the high frequency, 15 times the vortex shedding frequency, was identified as exhibiting good performance for all oncoming wind angles. The influence of the synthetic jet on the time-averaged flow structures was analysed, with it being found that the downwash flow is enhanced significantly and the recirculation region is extended in the streamwise direction under its effect. A spectral proper orthogonal decomposition analysis for the controlled case confirmed that the synthetic jet enhances the turbulent fluctuation above the top surface, but has no direct impact on the side-force fluctuation. The enhanced turbulent fluctuation induces a stronger downwash flow, which could further influence the spanwise vortex shedding. The unsteady near wake structures in the unforced and controlled cases were also investigated, with the synthetic jet found to suppress antisymmetric spanwise vortex shedding and promote symmetric vortex shedding, which is ascribed to the enhanced downwash flow.

In a third part, an H_∞ loop-shaping feedback control method employing a synthetic jet along the leading edges of the building's side faces was proposed to mitigate the unsteady loading of a high-rise building exposed to differing oncoming wind directions. Three different oncoming wind angles were investigated. The sensor signal and actuator were chosen based on the spectral information in the sensor signal, the control authority of the actuator signal and a dynamically linear response of sensing to actuation. The open-loop transfer functions for three oncoming wind angles were then identified respectively. A reference linear open-loop transfer function was defined as the target plant used in the H_∞ loop-shaping feedback controller design. The differences between the reference open-loop system and open-loop transfer functions for differing oncoming wind angles were quantified by the ν-gap metric. An H_∞ loop-shaping controller was then designed to mitigate the side-force fluctuations associated with the antisymmetric vortex shedding and guarantee robustness. The designed controller was implemented in large eddy simulations and attenuated successfully the building's side-force fluctuations for different oncoming wind angles, including a wind angle which had not been used in the controller design process.

The open-loop and feedback control results demonstrate the potential of active control techniques for the attenuation of unsteady wind loading of a high-rise building. This work can provide a theoretical basis for the practical application of the novel active control approaches to high-rise buildings and may offer a conceptual starting point for the application of active control techniques to real high-rise buildings.

6.2 Future Work

The current numerical study proved to be successful in capturing the intermittent nature of vortex shedding in the flow around a high-rise building. It can be found the downwash flow near the top surface tends to postpone the antisymmetric vortex shedding. It would be interesting to establish a full understanding of how the downwash flow interacts with the spanwise vortex shedding behaviour. Investigation into the low-Reynolds number flow around a square finite cylinder can promote a deeper understanding of the three-dimensional flow structures interaction.

More modern advanced controllers can also yield interesting results. The feedback control strategies in this work were designed based on the linear system identification and loop-shaping methods. The combination of data-driven system models and the optimal control theory has the potential to result in a better controller to achieve the reduction of unsteady loading.

In terms of the passive control techniques for minimising unsteady wind loading, another element of future work could be to develop systematic shape optimisation methods applied at the upstream corners based on numerical simulations and neural networks.

The high-rise building in this study is isolated. Interesting to extend to the simple case with interacting building flows - one high-rise building located very close to another. The different flow structures need to be further explored. Again, active control and passive control techniques for attenuating unsteady loading could also be investigated.

Moreover, given that a rigid high-rise building model was considered in this work, an elastic building model could be used in future work to investigate the flow-induced vibrations as well as the unsteady flow features of the high-rise building. Flow control techniques, especially active flow control, aiming to suppress the negative effects of flow-induced vibrations would be further explored.

Bibliography

Åström, Karl Johan & Murray, Richard M 2021 *Feedback systems: an introduction for scientists and engineers*. Princeton university press.

Bai, H.L. & Alam, M.M. 2018 Dependence of square cylinder wake on reynolds number. *Phys. Fluids* **30** (1), 015102.

Behera, S. & Saha, A.K. 2019 Characteristics of the flow past a wall-mounted finite-length square cylinder at low reynolds number with varying boundary layer thickness. *J. Fluid Eng.* **141** (6).

Billoud, G., Galland, M.A., Huynh, H.C. & Candel, E.S. 1992 Adaptive active control of combustion instabilities. *Combust. Sci. Technol.* **81** (4-6), 257–283.

Bisset, D.K, Antonia, R.A. & Browne, L. 1990 Spatial organization of large structures in the turbulent far wake of a cylinder. *J. Fluid Mech.* **218**, 439–461.

Blocken, B. 2014 50 years of computational wind engineering: past, present and future. *J. Wind Eng. Ind. Aerod.* **129**, 69–102.

Bourgeois, J.A., Sattari, P. & Martinuzzi, R.J. 2011 Alternating half-loop shedding in the turbulent wake of a finite surface-mounted square cylinder with a thin boundary layer. *Phys. Fluids* **23** (9), 095101.

Bourgeois, J. A., Noack, B. R. & Martinuzzi, R. J. 2013 Generalized phase average with applications to sensor-based flow estimation of the wall-mounted square cylinder wake. *Journal of Fluid Mechanics* **736**, 316–350.

Brun, C., Aubrun, S., Goossens, T. & Ravier, P. 2008 Coherent structures and their frequency signature in the separated shear layer on the sides of a square cylinder. *Flow Turbul. Combust.* **81** (1-2), 97–114.

Brunton, S.L. & Noack, B.R. 2015 Closed-loop turbulence control: Progress and challenges. *Appl. Mech. Rev.* **67** (5).

Carassale, Luigi, Freda, Andrea & Marre-Brunenghi, Michela 2014 Experimental investigation on the aerodynamic behavior of square cylinders with rounded corners. *J. Fluids Struct.* **44**, 195–204.

Cattafesta III, Louis N & Sheplak, Mark 2011 Actuators for active flow control. *Annu. Rev. Fluid Mech.* **43**, 247–272.

Choi, H., Jeon, W.P. & Kim, J. 2008 Control of flow over a bluff body. *Annu. Rev. Fluid Mech.* **40**, 113–139.

Dahan, J.A., Morgans, A.S. & Lardeau, S. 2012 Feedback control for form-drag reduction on a bluff body with a blunt trailing edge. *J. Fluid Mech.* **704**, 360–387.

Dalla Longa, L., Evstafyeva, O. & Morgans, A.S. 2019 Simulations of the bi-modal wake past three-dimensional blunt bluff bodies. *J. Fluid Mech.* **866**, 791–809.

Dalla Longa, L., Morgans, A.S. & Dahan, J.A. 2017 Reducing the pressure drag of a d-shaped bluff body using linear feedback control. *Theor. Comput. Fluid Dyn.* **31** (5-6), 567–577.

Elshaer, A., Bitsuamlak, G. & Damatty, A. 2016 Aerodynamic shape optimization of tall buildings using twisting and corner modifications. In *8th International Colloquium on Bluff Body Aerodynamics and Applications*.

Elshaer, A., Bitsuamlak, G. & El Damatty, A. 2017 Enhancing wind performance of tall buildings using corner aerodynamic optimization. *Eng. Struct.* **136**, 133–148.

Erfan, I., Abbaspour, M. & Martinuzzi, R. J 2021 Investigation of the influence of low-frequency forcing on the 3-d turbulent wake of a cantilevered triangular prism. *J. Fluid Mech.* **913**.

Evesque, S & Dowling, A.P. 2001 Lms algorithm for adaptive control of combustion oscillations. *Combust. Sci. Technol.* **164** (1), 65–93.

Evstafyeva, O., Morgans, A.S. & Dalla Longa, L. 2017 Simulation and feedback control of the ahmed body flow exhibiting symmetry breaking behaviour. *J. Fluid Mech.* **817**.

Fabbiane, N., Bagheri, S. & Henningson, D.S. 2017 Energy efficiency and performance limitations of linear adaptive control for transition delay. *J. Fluid Mech.* **810**, 60–81.

Ferziger, J., Perić, M. & Street, R. L 2002 *Computational methods for fluid dynamics*, , vol. 3. Springer.

Flinois, T.L.B. & Morgans, A.S. 2016 Feedback control of unstable flows: a direct modelling approach using the eigensystem realisation algorithm. *J. Fluid Mech.* **793**, 41–78.

Franke, J., Hellsten, A., Schlunzen, K.H. & Carissimo, B. 2011 The cost 732 best practice guideline for cfd simulation of flows in the urban environment: a summary. *Int. J. Environ. Pollut.* **44** (1-4), 419–427.

Giangaspero, G., Amerio, L., Downie, S., Zasso, A. & Vincent, P. 2022 High-order scale-resolving simulations of extreme wind loads on a model high-rise building. *J. Wind Eng. Ind. Aerod.* **230**, 105169.

Golnaraghi, F. & Kuo, B.C. 2017 *Automatic control systems*. McGraw-Hill Education.

Gu, M. & Quan, Y. 2004 Across-wind loads of typical tall buildings. *J. Wind Eng. Ind. Aerod.* **92** (13), 1147–1165.

Gad-el Hak, M. 2000 *Flow Control: Passive, Active, and Reactive Flow Management*. Cambridge University Press.

Henning, L. & King, R. 2005 Drag reduction by closed-loop control of a separated flow over a bluff body with a blunt trailing edge. In *Proceedings of the 44th IEEE Conference on Decision and Control*, pp. 494–499. IEEE.

Hertwig, D., Efthimiou, G., Bartzis, J. & Leitl, B. 2012 Cfd-rans model validation of turbulent flow in a semi-idealized urban canopy. *J. Wind Eng. Ind. Aerod.* **111**, 61–72.

Hesse, F. & Morgans, A.S. 2021 Simulation of wake bimodality behind squareback bluff-bodies using les. *Comput. Fluids* **223**, 104901.

Hesse, F. & Morgans, A.S. 2023 Characterization of the unsteady wake aerodynamics for an industry relevant road vehicle geometry using les. *Flow. Turbul. Combust.* pp. 1–33.

Hosseini, Z., Bourgeois, J.A. & Martinuzzi, R.J. 2013 Large-scale structures in dipole and quadrupole wakes of a wall-mounted finite rectangular cylinder. *Exp. Fluids* **54**, 1–16.

Hu, X. & Morgans, A. S. 2022 Attenuation of the unsteady loading on a high-rise building using feedback control. *J. Fluid Mech.* **944**, A10.

Huang, P., Luo, P. & Gu, M. 2005 Pressure and forces measurements on CAARC standard tall building in wind tunnel of tong ji university. In *Proceedings of the 12th national wind engineering conference of China, Xi'an, China*, pp. 240–244.

Huang, S.H., Li, Q.S. & Wu, J.R. 2010 A general inflow turbulence generator for large eddy simulation. *J. Wind Eng. Ind. Aerod.* **98** (10-11), 600–617.

Irwin, Peter A. 2009 Wind engineering challenges of the new generation of super-tall buildings. *J. Wind Eng. Ind. Aerod.* **97** (7-8), 328–334.

Jarrin, N., Benhamadouche, S., Laurence, D. & Prosser, R. 2006 A synthetic-eddy-method for generating inflow conditions for large-eddy simulations. *Int. J. Heat Fluid Flow* **27** (4), 585–593.

Kareem, A., Kijewski, T. & Tamura, Y. 1999 Mitigation of motions of tall buildings with specific examples of recent applications. *Wind Struct.* **2** (3), 201–251.

Kawai, H 1998 Effect of corner modifications on aeroelastic instabilities of tall buildings. *J. Wind Eng. Ind. Aerod.* **74**, 719–729.

Kawamura, T., Hiwada, M., Hibino, T., Mabuchi, I. & Kumada, M. 1984 Flow around a finite circular cylinder on a flat plate: Cylinder height greater than turbulent boundary layer thickness. *Bull. JSME* **27** (232), 2142–2151.

KIM, Y. & KANDA, J. 2010 Characteristics of aerodynamic forces and pressures on square plan buildings with height variations. *J. Wind Eng. Ind. Aerod.* **98** (8-9), 449–465.

KRAJNOVIĆ, S. 2009 Large eddy simulation of flows around ground vehicles and other bluff bodies. *P. Roy. Soc. A-Math. Phy.* **367** (1899), 2917–2930.

KURZ, A., GOLDIN, N., KING, R., TROPEA, C. & GRUNDMANN, S. 2013 Hybrid transition control approach for plasma actuators. *Exp. Fluids* **54** (11), 1–4.

KWOK, K. 1982 Cross-wind response of tall buildings. *Eng. Struct.* **4** (4), 256–262.

LI, J. & MORGANS, A.S. 2016 Feedback control of combustion instabilities from within limit cycle oscillations using h loop-shaping and the ν-gap metric. *P. Roy. Soc. A-Math. Phy.* **472** (2191), 20150821.

LI, R.Y., BARROS, D., BORÉE, J., CADOT, O., NOACK, B.R. & CORDIER, L. 2016 Feedback control of bimodal wake dynamics. *Exp. Fluids* **57** (10), 1–6.

LIANG, S., LIU, S.C., LI, Q.S., ZHANG, L.L. & GU, M. 2002 Mathematical model of acrosswind dynamic loads on rectangular tall buildings. *J. Wind Eng. Ind. Aerod.* **90** (12-15), 1757–1770.

LUMLEY, J. L. 1967 The structure of inhomogeneous turbulent flows. *Atmos. Turb. Radio Wave Prop.* pp. 166–178.

MADISETTI, V. 1997 *The digital signal processing handbook*. CRC press.

MCFARLANE, D. & GLOVER, K. 1992 A loop-shaping design procedure using h/sub infinity/synthesis. *IEEE Trans. Autom. Control* **37** (6), 759–769.

MELBOURNE, W.H. 1980 Comparison of measurements on the CAARC standard tall building model in simulated model wind flows. *J. Wind Eng. Ind. Aerod.* **6** (1-2), 73–88.

MENICOVICH, D., LANDER, D., VOLLEN, J., AMITAY, M., LETCHFORD, C. & DYSON, A. 2014 Improving aerodynamic performance of tall buildings using fluid based aerodynamic modification. *J. Wind Eng. Ind. Aerod.* **133**, 263–273.

NGOOI, T.B. 2018 Hardware development for high-frequency force balance (HFFB) method.

NICOUD, F. & DUCROS, F. 1999 Subgrid-scale stress modelling based on the square of the velocity gradient tensor. *Flow Turbul. Combust.* **62** (3), 183–200.

OBASAJU, E.D. 1992 Measurement of forces and base overturning moments on the CAARC tall building model in a simulated atmospheric boundary layer. *J. Wind Eng. Ind. Aerod.* **40** (2), 103–126.

OGUNREMI, A. & SUMNER, D. 2015 The effect of a splitter plate on the flow around a finite prism. *J. Fluids Struc.* **59**, 1–21.

OXLADE, A., MORRISON, J., QUBAIN, A. & RIGAS, G. 2015 High-frequency forcing of a turbulent axisymmetric wake. *J. Fluid Mech.* **770**, 305–318.

PARK, C. & LEE, S. 2000 Free end effects on the near wake flow structure behind a finite circular cylinder. *J. Wind Eng. Ind. Aerod.* **88** (2-3), 231–246.

PASTOOR, M., HENNING, L., NOACK, B.R., KING, R. & TADMOR, G. 2008 Feedback shear layer control for bluff body drag reduction. *J. Fluid Mech.* **608**, 161.

PORTEOUS, R., MOREAU, D.J. & DOOLAN, C. 2017 The aeroacoustics of finite wall-mounted square cylinders. *J. Fluid Mech.* **832**, 287.

Pörtner, H., Roberts, D., Adams, H., Adler, C., Aldunce, P., Ali, E., Begum, R., Betts, R., Kerr, R. & Biesbroek, R. 2022 *Climate change 2022: Impacts, adaptation and vulnerability*. IPCC Geneva, Switzerland:.

Posa, A., Broglia, R., Felli, M., Falchi, M. & Balaras, E. 2019 Characterization of the wake of a submarine propeller via large-eddy simulation. *Comput. Fluids* **184**, 138–152.

Qu, Y., Wang, J., Feng, L. & He, X. 2019 Effect of excitation frequency on flow characteristics around a square cylinder with a synthetic jet positioned at front surface. *J. Fluid Mech.* **880**, 764–798.

Qu, Yuan, Wang, Jinjun, Sun, Mao, Feng, Lihao, Pan, Chong, Gao, Qi & He, Guosheng 2017 Wake vortex evolution of square cylinder with a slot synthetic jet positioned at the rear surface. *J. Fluid Mech.* **812**, 940–965.

Ricci, M., Patruno, L., Kalkman, I., de Miranda, S. & Blocken, B. 2018 Towards les as a design tool: Wind loads assessment on a high-rise building. *J. Wind Eng. Ind. Aerod.* **180**, 1–18.

Rigas, G., Oxlade, A.R., Morgans, A.S. & Morrison, J.F. 2014 Low-dimensional dynamics of a turbulent axisymmetric wake. *J. Fluid Mech.* **755**, R5.

Rowley, C.W., Williams, D., Colonius, T., Murray, R. & Macmynowski, D. 2006 Linear models for control of cavity flow oscillations. *J. Fluid Mech.* **547**, 317–330.

Saeedi, M. & Wang, B.C. 2016 Large-eddy simulation of turbulent flow around a finite-height wall-mounted square cylinder within a thin boundary layer. *Flow Turbul. Combust.* **97** (2), 513–538.

Sattari, P., Bourgeois, J.A. & Martinuzzi, R.J. 2012 On the vortex dynamics in the wake of a finite surface-mounted square cylinder. *Exp. Fluids* **52** (5), 1149–1167.

Schmidt, Oliver T & Colonius, Tim 2020 Guide to spectral proper orthogonal decomposition. *Aiaa J.* **58** (3), 1023–1033.

Schmidt, O. T., Towne, A., Rigas, G., Colonius, T. & Brès, G. 2018 Spectral analysis of jet turbulence. *J. Fluid Mech.* **855**, 953–982.

da Silva, B. L., Chakravarty, R., Sumner, D. & Bergstrom, D. J. 2020 Aerodynamic forces and three-dimensional flow structures in the mean wake of a surface-mounted finite-height square prism. *Int. J. Heat Fluid Fl.* **83**, 108569.

Sirovich, L. 1987 Turbulence and the dynamics of coherent structures, parts i, ii and iii. *Quart. Appl. Math.* pp. 561–590.

Skyscrapercenter 2021 Tall buildings in 2020: Covid-19 contributes to dip in year-on-year completions. *Tech. Rep.*. `https://www.skyscrapercenter.com/year-in-review/2020`.

Sohankar, A. 2006 Flow over a bluff body from moderate to high reynolds numbers using large eddy simulation. *Comput. Fluids* **35** (10), 1154–1168.

Stalnov, O., Fono, I. & Seifert, A. 2011 Closed-loop bluff-body wake stabilization via fluidic excitation. *Theor. Comput. Fluid Dyn.* **25** (1), 209–219.

Sumner, D. 2013 Flow above the free end of a surface-mounted finite-height circular cylinder: a review. *J. Fluids Struct.* **43**, 41–63.

Sumner, D., Heseltine, J.L. & Dansereau, O. 2004 Wake structure of a finite circular cylinder of small aspect ratio. *Exp. Fluids* **37** (5), 720–730.

Taira, K., Brunton, S.L., Dawson, S.T.M., Rowley, C.W., Colonius, T., McKeon, B.J., Schmidt, O.T., Gordeyev, S., Theofilis, V. & Ukeiley, L. 2017 Modal analysis of fluid flows: An overview. *AIAA J.* **55** (12), 4013–4041.

Tamura, Y., Tanaka, H., Ohtake, K., Nakai, M. & Kim, Y. 2010 Aerodynamic characteristics of tall building models with various unconventional configurations. In *Structures Congress 2010*, pp. 3104–3113.

Thordal, M.S., Bennetsen, J.C. & Koss, H.H. 2019 Review for practical application of cfd for the determination of wind load on high-rise buildings. *J. Wind Eng. Ind. Aerod.* **186**, 155–168.

Tominaga, Y. 2015 Flow around a high-rise building using steady and unsteady rans cfd: Effect of large-scale fluctuations on the velocity statistics. *J. Wind Eng. Ind. Aerod.* **142**, 93–103.

Tominaga, Y., Mochida, A., Yoshie, R., Kataoka, H., Nozu, T., Yoshikawa, M. & Shirasawa, T. 2008 Aij guidelines for practical applications of cfd to pedestrian wind environment around buildings. *J. Wind Eng. Ind. Aerod.* **96** (10-11), 1749–1761.

Towne, A., Schmidt, O. T. & Colonius, T. 2018 Spectral proper orthogonal decomposition and its relationship to dynamic mode decomposition and resolvent analysis. *J. Fluid Mech.* **847**, 821–867.

Tse, K., Hitchcock, P., Kwok, K., Thepmongkorn, S. & Chan, C. 2009 Economic perspectives of aerodynamic treatments of square tall buildings. *J. Wind Eng. Ind. Aerod.* **97** (9-10), 455–467.

Vinnicombe, Gl. 2000 *Uncertainty and Feedback, H Loop-shaping and the V-gap Metric*. World Scientific.

WANG, H., PENG, S., LI, Y. & HE, X. 2018 Control of the aerodynamic forces of a finite-length square cylinder with steady slot suction at its free end. *J. Wind Eng. Ind. Aerod.* **179**, 438–448.

WANG, H., ZHAO, C., ZENG, L., A., MAHBUB & TANG, H. 2022 Control of the flow around a finite square cylinder with a flexible plate attached at the free end. *Phys. Fluids* **34** (2), 027109.

WANG, H.F., ZHAO, X.Y., HE, X.H. & ZHOU, Y. 2017 Effects of oncoming flow conditions on the aerodynamic forces on a cantilevered square cylinder. *J. Fluids Struct.* **75**, 140–157.

WANG, H.F. & ZHOU, Y. 2009 The finite-length square cylinder near wake. *J. Fluid Mech.* **638**, 453.

WANG, H., ZHOU, Y., CHAN, C. & LAM, K. S. 2006 Effect of initial conditions on interaction between a boundary layer and a wall-mounted finite-length-cylinder wake. *Phys. Fluids* **18** (6), 065106.

WELLER, J., CAMARRI, S. & IOLLO, A. 2009 Feedback control by low-order modelling of the laminar flow past a bluff body. *J. Fluid Mech.* **634**, 405–418.

WIDROW, B., MCCOOL, J., LARIMORE, M.G. & JOHNSON, C.R. 1977 Stationary and nonstationary learning characteristics of the lms adaptive filter. In *Aspects of signal processing*, pp. 355–393. Springer.

WILCOX, D.C.S 1998 *Turbulence modeling for CFD*, , vol. 2. DCW industries La Canada, CA.

YAN, B.W. & LI, Q.S. 2015 Inflow turbulence generation methods with large eddy simulation for wind effects on tall buildings. *Comput. Fluids* **116**, 158–175.

YAUWENAS, Y., PORTEOUS, R., MOREAU, D.J. & DOOLAN, C.J. 2019 The effect of aspect ratio on the wake structure of finite wall-mounted square cylinders. *J. Fluid Mech.* **875**, 929–960.

ZHANG, Y. & HABASHI, W.AND KHURRAM, R. 2015 Predicting wind-induced vibrations of high-rise buildings using unsteady cfd and modal analysis. *J. Wind Eng. Ind. Aerod.* **136**, 165–179.

ZHENG, CHAO-RONG & ZHANG, YAO-CHUN 2012 Computational fluid dynamics study on the performance and mechanism of suction control over a high-rise building. *Struct. Des. Tall Special Build.* **21** (7), 475–491.

ZHENG, X., MONTAZERI, H. & BLOCKEN, B. 2021 Cfd analysis of the impact of geometrical characteristics of building balconies on near-façade wind flow and surface pressure. *Build Environ.* **200**, 107904.

ZHOU, Y. & ANTONIA, R.A. 1993 A study of turbulent vortices in the near wake of a cylinder. *J. Fluid Mech.* **253**, 643–661.

ZHU, T. & MORRISON, J. F. 2021 Simulation of the turbulent axisymmetric bluff body wake with pulsed jet forcing. *Phys. Rev. Fluids* **6** (12), 124604.